Continuous Antibody Titer Assessment of the Biomanufacturing Process using Nanofluidic Binding Assays

by

Zhumei Rohskopf

BS, Beijing Institute of Technology (2013)
MS, Shanghai Institute of Optics and Fine Mechanics, Chinese Academy of Sciences (2016)
MS, Massachusetts Institute of Technology (2018)

Submitted to the Department of Mechanical Engineering
in partial fulfillment of the requirements for the Degree of

Doctor of Philosophy in Mechanical Engineering

at the

MASSACHUSETTS INSTITUTE OF TECHNOLOGY

June 2023

Authored by: Zhumei Rohskopf
Department of Mechanical Engineering
March 26, 2023

Certified by: Jongyoon Han
Professor of Electrical Engineering, MIT
Professor of Biological Engineering, MIT
Thesis Supervisor

Certified by: John Hart
Professor of Mechanical Engineering, MIT
Thesis Supervisor

Accepted by: Nicolas Hadjiconstantinou
Professor of Mechanical Engineering
Chair, Department of Mechanical Engineering Committee on Graduate Students

Continuous Antibody Titer Assessment of the Biomanufacturing Process using Nanofluidic Binding Assays

by

Zhumei Rohskopf

Submitted to the Department of Mechanical Engineering

in partial fulfillment of the requirements for the Degree of

Doctor of Philosophy in Mechanical Engineering

Online monitoring of monoclonal antibody (mAb) product titers throughout biologics process development and production enables the implementation of quality-by-design biomanufacturing, rapid bioprocess decision-making, and process optimization. Intermittent sampling and analysis are presently utilized to maintain long-term perfusion culture. However, this increases the risk of introducing external contaminants into the cell culture and the analyzed analytes. Sensors used in in-line probe-based approaches must withstand harsh clean-in-place and sterilization-in-place procedures. Analytical instruments that provide real-time monitoring and continuous feed flow processing and are therefore suitable for direct integration into a perfusion bioreactor are ideal for improving overall process robustness. Online implementation of conventional analytical methods, including high-performance liquid chromatography (HPLC) and turbidimetric analysis, typically

necessitates interfacing with an automated sampling system capable of online sampling and fractionation, which appends to the cost, risk of failure, and mechanical complexity of the system.

The objective of this study is to create a nanofluidic device for online monitoring of monoclonal antibody (mAb) titers based on ligand-binding. This system has a small footprint, straightforward operation procedures, and minimal complex data analytics requirements. During manufacturing and process development, this nanofluidic platform delivers direct titer measurement in the bioreactor as well as functional information on the binding activity, enabling immediate modification of process parameters to improve biomanufacturing yield and preserve the desired product quality.

Thesis Supervisor: Jongyoon Han, Professor of Electrical Engineering and Professor of Biological Engineering

ACKNOWLEDGEMENTS

I express my sincere gratitude to my advisor, Dr. Jongyoon Han. His thoughtful advice propelled me further toward achieving my academic and professional goals. He has provided many golden opportunities for which I am forever grateful, including switching to his group and thoughtfully helping me present my work and establish a professional network. Dr. Jongyoon Han is an amazingly thoughtful advisor, and his actions show that he cares for his students, so I am thankful for the past few years under his mentorship. I am also sincerely thankful to my committee for their time, patience, and suggestions on my thesis.

I thank my parents and grandparents for their perpetual support. I thank them for teaching me, through example, the value of working hard to achieve goals. I would like to thank my husband, Drew, for his unwavering emotional support throughout my time at MIT, and our shared experience as Course 2 students. I would also like to thank my parents-in-law for their support.

My appreciation also goes to fellow group members and students. I must thank Taehong Kown, Sung Hee Ko, Dragana Bozinovski, Mingyang Cui, Hyungkook Jeon, and Naresh Mohan for their fruitful collaborations and discussions.

This work was carried out in part through the use of MIT.nano's facilities. I would like to thank all the support from the staff, including Dennis Ward, Kristofor Payer, Eric Lim, Scott Poesse, Paul Tierney, Bob Bicchieri, Jorg Scholvin, Donal Jamieson, and Kurt Broderick, for their help with developing the fabrication process.

This work was performed in part at the Harvard University Center for Nanoscale Systems (CNS); a member of the National Nanotechnology Coordinated Infrastructure Network (NNCI), which is

supported by the National Science Foundation under NSF award No. ECCS-2025158. I would like to thank Dr. Ling Xie for her help with developing the DRIE etching recipe.

I would like to thank Mark Belanger at the Edgerton Student Shop for guiding me through CNC machining.

This work was performed in part at the MRL Materials Analysis and X-Ray Facility, and the MIT Biophysical Instrumentation Facility.

This work was supported under Grant No. 5U01FD006751-03 awarded by the Food and Drug Administration.

TABLE OF CONTENTS

LIST OF FIGURES

CHAPTER 1. INTRODUCTION

The biopharmaceuticals market was valued at USD 345.84 billion in 2021 and is predicted to reach USD 974.48 billion by 2030, with a compound annual growth rate of 11.7% from 2022-2030 [1]. Monoclonal antibodies (mAbs), currently the most significant product group of the pharmaceutical industry, are used to enhance and suppress the immune response in various medical conditions and to treat various diseases, such as cancer, cardiovascular, and cerebrovascular diseases. The dominance of approved mAbs in the global biopharmaceuticals market has increased steadily in the past ten years, and its product approval number and the relative importance of mAbs in terms of the percentage of overall biopharmaceutical product sales also continue to grow [2], [3]. Around the world, at least 570 therapeutic mAbs have been studied in clinical trials, and 79 therapeutic mAbs have been approved by the United States Food and Drug Administration (US FDA) and are currently on the market [4], including 30 mAbs for treating cancer. Between 2008 and 2017, 48 new mAbs were approved, contributing to a total global market of 61 mAbs in clinical trials. Strikingly, a total of 18 new antibodies were granted approval by the US FDA from 2018 to 2019 [4]. The global mAbs market size is expected to grow from $168.70 billion in 2021 to $188.18 billion in 2022, at a compound annual growth rate (CAGR) of 11.5% [5]. As the biopharmaceutical industry matures, older patents on approved biologics expire. Thus, non-brand companies can begin to manufacture generic versions of the biotherapeutic (biosimilars), analogous to generic drugs in the pharmaceutical industry. This biosimilar market is also expected to grow at very high compounded annual growth rates (24–34%) by 2025 [5]. The COVID-19 pandemic has

acted as a catalyst for biopharmaceutical industry growth, given that numerous biological compounds have been produced to tackle the virus and reduce its strain on healthcare systems.

Biopharmaceutical production needs large manufacturing capacities, which must be designed with cost and time in mind. With exponential growth of biotherapeutics, production capabilities and efficiency are more important than before. The increasing complexity of biomanufacturing requires flexible pipeline infrastructures that can accommodate different modalities with varying demands [6]. Mammalian cells, which are employed in the manufacturing of antibodies, have historically been considered difficult to work with due to factors such as low yield, medium complexity, serum requirement, and shear sensitivity [7]. Recent advances in process optimization and cell line engineering have allowed antibody production to generate high yields above 10 g/L in fed-batch Chinese hamster overall (CHO) lines, even in a small-scale bioreactor, while maintaining a high viable cell density over a 14-day production time [8]. In addition to optimizing traditional batch-based processes, alternative manufacturing approaches are under development. One strategy for process intensification is to implement continuous biomanufacturing. Proposed in 2011, continuous biomanufacturing features perfusion bioreactors that simultaneously charge and discharge the media and products, which has several advantages over traditional fed-batch processes. Compared with the traditional method in which products are harvested at the end of the process, continuous biomanufacturing significantly reduces the equipment and facility size and the associated capital costs, increases volumetric productivity, and improves product quality through enhanced control and uniformity of the microenvironment [9]–[11]. With all these

attributes, continuous biomanufacturing is identified as a key enabler for modernizing pharmaceutical manufacturing in 2015 [12].

Process and product understanding are the basis for producing safe and effective medicines. The consistency of the critical quality attributes (CQAs) of the product is ensured by implementing a control strategy that maintains the process within the bounds of the design space. Lot-to-lot variation indicated that the current established processes were not as robust as imagined, resulting in fewer products to be commercialized and an increased cost of drug manufacturing. To guide the biomanufacturing sector towards better production efficiencies while still ensuring maximum process safety in a timely manner, the Quality by Design (QbD) and Process Analytical Technologies (PATs) initiatives were established [13], [14]. Central to the implementation of QbD is defining and identifying the CQAs of a product, as well as defining an appropriate design space rather than relying on post-quality control batch testing (also known as “Quality by Testing”). QbD is a systematic and rigorous approach to the development of products and processes, which results in a detailed understanding of the factors that influence the clinical efficacy and safety of the products, and the establishment of robust control strategies to ensure consistent process performance [15]. However, currently, the implementation of QbD faces some practical difficulties that arise from the complexity and heterogeneity of biopharmaceutical products [16]. Biological systems are very sensitive to many process conditions, and the fundamental understanding of the intricate relationships between a very significant number of process parameters and the ultimate desired process outcome is often not complete. Numerous experiments to understand the quality limitations of a process are called for and can result in long delays in process development timelines. Even previous work with

similar compounds does not accelerate these timelines substantially, as biomolecule properties vary considerably from one another, even with seemingly minor changes [17]. Effective process optimization requires real-time monitoring of key performance indicators (KPIs). Capabilities to monitor IgG titers are central to optimizing process conditions and achieving high yields as well as consistent product quality. The IgG titer is thus naturally an important KPI in the production of mAbs. The knowledge gained about product and process understanding facilitates the identification of the sources of variability that impact product quality, which provides an opportunity to shift controls upstream and monitor the CQAs of the output materials in real-time. In-process testing reduces the reliance on end-product release testing and provides an increased level of quality assurance. Without adequate PATs and CQAs in place, one cannot understand the process properly.

The extended culturing duration of continuous biomanufacturing intensifies the need for online and fast PAT and CQA that usually involve sensors that are associated with, or close to, the process equipment. In addition, it is preferred that the measurements are relatively continuous and often allow for closed-loop process control capable of identifying deviations in product CQAs. As all parts of the process are closely integrated, and the product flows continuously through different unit operations, the current local control of individual unit operations implemented in batch manufacturing makes it difficult to identify the cause of specific deviations during production. It is safe to say that online monitoring of CQAs is a prerequisite for ensuring product quality and consistency.

In this chapter, an overview of biotherapeutic processing modes is first reviewed. The need for CQAs to be routinely monitored is discussed. The main technological tools used for bioprocess monitoring, with a focus on online upstream monitoring, are then presented.

1.1 Continuous biopharmaceutical processing

Biopharmaceutical processing is typically divided into two parts: upstream and downstream. The upstream process includes two steps: inoculation and cultivation (seed expansion) in seed bioreactors and cell culture production in large-scale bioreactors. When producing antibodies using CHO cells, the product is released into the supernatant, and the induction of flock formation enables easier cell removal without compromising product yield. Reliable and efficient separation, coupled with introducing fresh cell culture medium, enables high cell densities and viability. The cell retention step, which also refers to the clarification step, is the start of the downstream or purification processing. At this step, cells and cellular debris are separated from the culture fluid to produce a clarified CHO cell culture supernatant (CCCCS) suitable for further purification. A standard purification process for a therapeutic antibody consists of several steps to reach the statutory high-purity requirements. First, capture is conducted to concentrate the antibodies from the cell culture, followed by virus inactivation (VIN) at low pH conditions to inactivate viruses. Then the polishing steps specifically target the removal of process- and product-related impurities (*e.g.,* aggregates). Both batch and continuous operations have been developed for mAb production in mammalian cells, which are summarized in Figure 1 [18], [19].

For batch processing, the antibody is usually captured by Protein A chromatography columns. The polishing steps are typically performed in bind-and-elute or flow-through modes, typically using anion exchange chromatography (AEC) and cation exchange chromatography (CEC) to remove host cell proteins (HCPs), DNA, leached Protein A, and

aggregates. At last, a viral clearance step is performed by nanofiltration followed by ultra-/diafiltration (UF/DF).

Continuous bioprocessing generally refers to perfusion technologies. A typical perfusion bioreactor runs at a fixed volume and fixed cell concentration for 30-90 days or longer, depending on the cell line. During this time, the feed media is constantly refreshed. The cells are retained in the bioreactor using a cell retention device while the recombinant products are harvested, and the growth-inhibiting metabolites are removed concurrently. The evolution of continuous perfusion bioreactors and the availability of established single-use upstream technologies offer cost and performance benefits to biologics manufacturers. High cell density cultivations can be maintained for a prolonged time in a continuous upstream process, which calls for continuous purification rather than the classical batch processing of large supernatant volumes. A recent cost of goods evaluation reported 30% savings could be achieved in an integrated continuous process using disposable technologies over a stainless-steel batch process [20]. With regard to continuous downstream processing, continuous chromatography can be applied, which utilizes multiple smaller columns to maximize the use of the resin's binding capacity. Using smaller columns provides an economic advantage by reducing the purification footprint, buffer, and resin usage [21]. The continuous precipitation process and aqueous two-phase extraction (ATPS) are also available [22]. Viral contamination of biologics can occur due to the source of the cell line or due to the introduction of adventitious agents during the manufacturing process, and demonstrating virus safety is an important regulatory requirement for biologics expressed in human or animal cell lines [23]. mAbs are prone to aggregation when held at low pH for extended periods, which poses some challenges for

low pH continuous VIN. The eluate is continuously collected from the capture processing and fed into the VIN tank, where it is held for the required inactivation time. Usually, a surge tank is used between capture and VIN. Solvent/detergent treatment and ultraviolet irradiation methods are alternative solutions for developing a continuous VIN [24]. The aforementioned polishing processes can be used in continuous mode by using multiple columns. Other methods like simulated moving bed (SMB) chromatography, multicolumn countercurrent solvent gradient purification (MCSGP), annular chromatography, radial flow chromatography, protein crystallization, and tangential flow filtration can also be used in continuous purification steps [25]. Two viral filters, ran alternately, can be used for continuous viral filtration [11]. The continuous formulation can be achieved by single-pass tangential flow filtration (SP-TFF), cascade diafiltration, countercurrent staged diafiltration, and crystallization [11].

Studies in continuous bioprocessing have demonstrated significant improvements in bioreactor volumetric productivity, resin capacity utilization, buffer consumption, and a reduction in both bioreactor and column size, compared to batch operation [10], [26]. A comparison of integrated continuous antibody production and batch processing revealed that five 2000 L bioreactors could deliver almost the same product mass as the batch scenario using four 12500 L bioreactors [27]. The productivity increase reduces the overall specific cost of goods per gram (COGs) by about 88% [28]. Compared to batch processing, continuous processing has a 15% lower operational cost and a 50% lower capital cost. Another research showed a 50% reduction in specific COGs, and a 66% reduction in facility costs compared to the fed-batch process [29]. The continuous process reduces the use of the primary capture column by two folds, which leads to a 68% reduction in

consumable costs at the same annual production rate. However, perfusion has a higher environmental footprint in the form of water consumption compared to fed-batch because of the relatively low titer [30]. The outcomes of the aforementioned studies are highly dependent on the various assumptions and system configurations. The following sections discuss key enabling technologies of continuous upstream processing, including the perfusion bioreactor and the cell retention device. The remaining challenges in establishing integrated, continuous processes were discussed at the end.

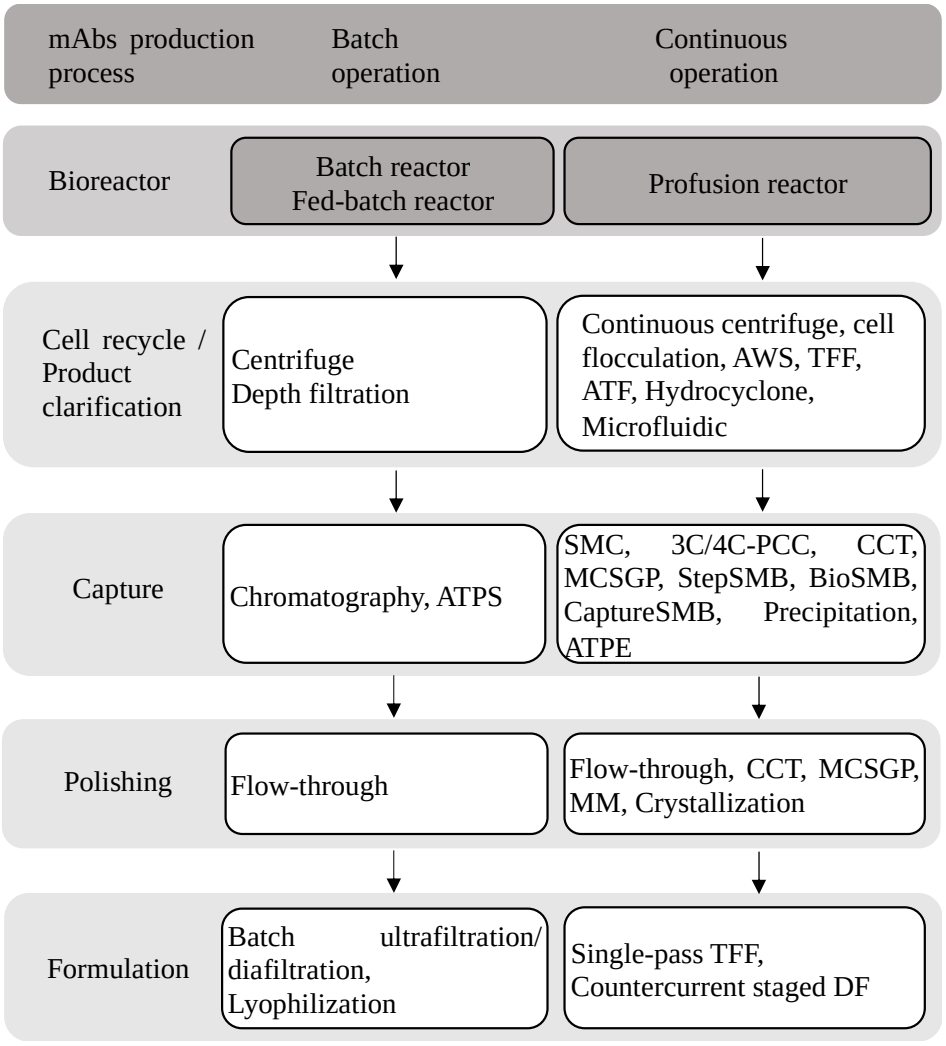

Figure 1 Flowchart of biopharmaceutical manufacturing processes of MAbs production.

1.2 Continuous upstream process

Current mAb production is generally carried out batch-wise due to the higher technical complexity of the perfusion bioreactor and the limitations of the cell retention devices available. Traditional upstream bioreactors such as fed-batch do not have an outlet stream, and all the waste, by-products, and target protein products accumulate inside the unit. The product is harvested at the end of each run. It is technically challenging to sustain high cell viability in those bioreactors because of the accumulation of undesired by-products (*e.g.*, ammonia and lactate), which could lead to undesired chemical and enzymatic modifications of the mAb [12], [31]. One solution to this problem is using perfusion bioreactors that allow cell cultivation with continuous delivery of new media and removal of waste products. A cell retention device is a cell culture media exchange system necessary to maintain a high cell density under constant conditions for an extended period of time. This can increase production while also allowing for a reduced footprint and culture vessel volume. Continuous biomanufacturing runs typically last around a month and require CHO cell-line stability to deliver the most proteins. In addition to the products that are continuously secreted from the cell, cell components such as HCPs and DNA are gradually released into the supernatant through cell lysis accompanied by the apoptosis of CHO cells, which contributes to contaminants that require downstream purification [32]. Preserving the viability of the retained cells is essential for the long-term process, which makes sedimentation technologies non-ideal. For the perfusion culture of suspended mammalian cells, studies have reviewed cell retention devices, including membrane filtration, gravitational settling, centrifugation, acoustic wave separation, and hydrodynamically sorting [33], [34].

1.2.1 Perfusion bioreactor

Figure 2 shows schematic diagrams of fed-batch and perfusion systems. The continuous feed of fresh nutrients and the continuous removal of the product, byproduct, and waste from the bioreactor achieve high cell density. The removal of toxic metabolites results in a healthier and more uniform culture over time, resulting in constant viable cell density (VCD), typically between 20-60 million cells/mL, and up to 200 million cells/mL [35], [36], and the viability can be maintained throughout the production process [6] [37]. A study showed that the average productivity in perfusion culture is 7.5 times greater than in fed-batch culture [38]. A lab-scale continuous-flow stirred-tank bioreactor demonstrated the startup and long-term operation for 83 days with a twofold volumetric productivity increase over the commercially-ready, optimized fed-batch process [39].

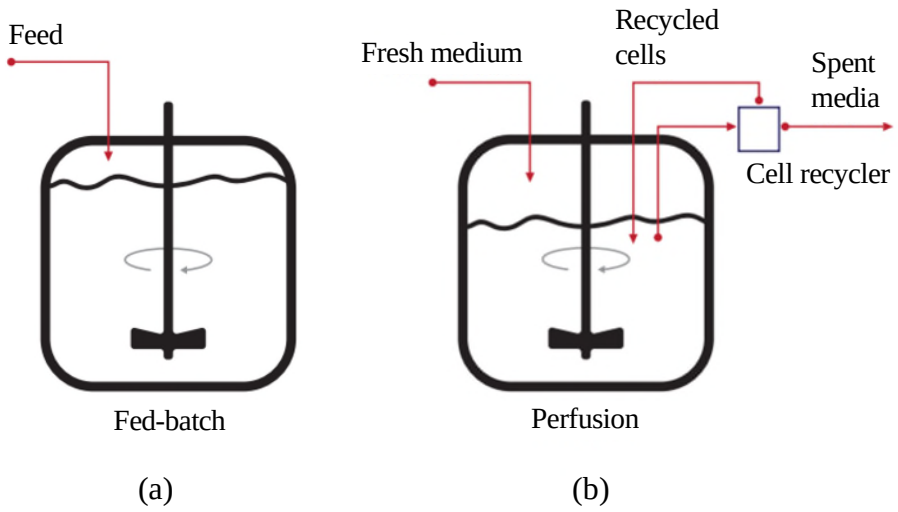

Figure 2 Modes of operation: (a) fed-batch and (b) perfusion. Nutrients are given continuously or intermittently to the system during fed-batch operation to control total substrate concentration. Perfusion systems continuously refill the media into the bioreactor while extracting spent media. Cells are removed from the extraction media and returned to the stirred tank bioreactor. An ultrafiltration retention module is utilized for recycling cells back into the system.

Besides, the product residence time in fed-batch bioreactors varies significantly, anywhere between just being produced and the entire duration of the culture. As a result, the harvest

is a collection of all mAbs produced at various time points throughout the process and under varying culture conditions. This results in significantly more product- and process-related impurities, such as aggregates, fragments, or charge variants. Because of the continuously changing environment, multiple protein isoforms could be expressed, resulting in heterogeneity and batch-to-batch variations. In contrast, the continual removal of products from the perfusion bioreactor ensures a relatively short and narrow residence period with an average value equal to the ratio between the bioreactor volume and the perfusion volumetric flow rate, typically in the order of 1-2 days. A stable environment is maintained during the entire production phase, and the kinetics of all processes in the bioreactor do not change over time, including those related to impurities or post-translational modifications [31]. The consistency of the bioreactor hydrodynamics results in stable perfusion bioreactor operation with precise control of cell density, flow rates, and media composition, resulting in regular cell metabolic behavior [40]. When compared to the fed-batch mode, this results in a more consistent product profile and a noticeable decrease in aggregate formation [38]. Furthermore, the product quality of mAb produced by the perfusion process conforms to the specified operating circumstances at a steady state, and a reliable correlation between the bioreactor operating conditions and the product features can be established. This information can be utilized to detect changes in operational parameters or to regulate certain product quality aspects, such as the glycan pattern [41]. One study investigated the effect of manganese, galactose, and VCD on N-linked glycosylation [42], indicating that perfusion systems have the potential to control quality attributes toward a specific target.

1.1.1 Continuous Clarification

Continuous processing mostly utilizes size-based filtrations, while non-filtration options such as continuous centrifugation, acoustic wave separation (AWS), and continuous flocculation have also been explored [43]–[46]. Another two membrane-less novel cell retention devices are based on hydrocyclone structures and inertial microfluidics [47]–[50]. Small-depth filtration is usually required following non-filtration-based methods.

1.1.1.1 Continuous microfiltration

Alternating tangential flow (ATF) filtration, as well as the most commonly used TFF and spin filters, have been employed in the CHO cell bioprocessing [51]–[53]. In TFF, the feed travels tangentially to the filter surface, while the permeate containing the product flows perpendicularly, reducing the trapping of cell debris and other solids in the filter [54]. Gradual fouling is still an issue, and the continued circulation of the bioreactor contents through the feed pump and TFF module can cause cell lysis [36]. In comparison, ATF uses a low-shear diaphragm pump to alternatingly drive the cell culture into and out through the standard hollow fiber membranes to separate cells and products. The high reverse flow across the membrane can efficiently detach the debris and reduce filter fouling.

The use of ATF in place of an internal spin filter can double cell density and enhance productivity by 50% [55]. A comparison investigation revealed that the TFF system is more resistant to bubbles and can achieve twice as high peak cell densities as ATF methods, while both failed at very high cell densities due to high viscosity [36]. Research showed up to 50% of the product was being partially retained in the bioreactor (product retention) in the TFF system, contrasting with 10% in the ATF [52]. The retention can be mitigated using hollow fiber filtration with a large pore size (>2 μm, compared to the commonly used

0.2 µm). This system showed nearly 100% product transmission and high cell viability (>90%), extending the run to 18 days [51].

1.1.1.2 Membrane-less technologies

Continuous centrifugation does not suffer from filter clogging and allows dead cells to be selectively separated and removed based on the centrifugal force used. The fluidized bed centrifuge retains the cells through the counteracting centrifugal and fluid flow forces, inducing little to no stress-related cell lysis [56]. A typical continuous centrifuge can process feed with solids at or below 10-13% [41], so dilution is required for solid feed levels above this. A higher burden of solids (≥15%) and sub-micron particles typically exceeds the capabilities of a continuous centrifuge to effectively remove the solids without a substantial loss of product [57]. In addition, centrifuges are usually associated with complex devices and moving parts, and have both high capital and operational costs, impacting the cost of goods.

AWS uses low-frequency acoustic standing waves to trap cells, which are then returned to the bioreactor by gravity sedimentation. Single-use Cadence™ acoustic separator was demonstrated to process up to 100 million cells/mL feed over 60 days, with 100% mAb transmission, 99% clarification, and consistent cell removal efficiency, positioning it well for emerging high-cell density perfusion processes [58].

Continuous flocculation accomplished with a tubular bioreactor using cationic polymers in combination with two parallel depth filters showed a 97% yield, regardless of the cell density [59]. While a sufficiently long bioreactor (5.76 m) is required to guarantee complete flocculation, possible cell toxicity is a concern.

Separation through a hydrocyclone (HC) is enabled by its special structure, which sustains the centrifugal field generated by the tangential inflow of the feed suspension at high flow rates [60]. HC can achieve a 70-80% centrifugal efficiency independent of the feed concentration without product retention [61]. The performance of the hydrocyclone is mainly determined by the pressure drop across the device, which sets the lower limit of the processing rate [62], resulting in a large processing capacity and rendering laboratory-scale evaluation under continuous perfusion mode difficult.

1.1.1.3 Microfluidic methods

Hydrodynamically sorting or separating cells with high throughput (on the order of a few mL/min per single microchannel) has recently been developed [48], [63]. Hydrodynamic forces are used to focus and separate particles laterally in a continuous flow within the channel, depending on the particle size and the channel structure. The inertial microfluidic device features passive operation without the need for active force fields, such as acoustic waves in AWS, and requires minimal maintenance compared to membrane filtration, making it a robust and easy-to-use technology. Typical channel structures are fabricated in polydimethylsiloxane (PDMS) using soft-lithographic techniques or in poly (methyl methacrylate) (PMMA) using laser cutters.

Size-dependent cell separation in spiral microchannels under laminar flow is attributed to the interaction of three factors: the shear-gradient-induced force, the wall-induced lift, and the secondary-flow drag forces (Dean drag) related to the curvature of the channel, which accelerates the arrangement of particles at equilibrium. A spiral channel with a trapezoidal

cross-section can generate strong Dean vortex cores to trap smaller particles near the outer wall while concentrating bigger particles towards the inner wall.

A single spiral channel was demonstrated for continuous separation of CHO cell culture with over 95% efficiency at a flow rate of 6 mL/min [47]. A combined flow rate of 500 mL/min was achieved through the massive multiplexing of 84 spiral chips. This inertial filtration technique can process a cell concentration of up to 10^7 cells/mL while maintaining high post-sorting cell viability. Cell recycling was recently performed with a spiral channel in a perfusion process [50]. The cell culture with >20 million cells/mL concentration was continuously separated through the device into the cell-free permeate and the retentate and provided a retention efficiency of 82% on average. High IgG1 recovery (>99%) and cell viability (>97%) were maintained throughout the test. Device multiplexing with four spiral channels can triple the flow rate to 700 mL/day for large-scale perfusion culture. The microfluidic cell retention device can also perform controlled continuous cell bleeding at high cell density without manual intervention.

Removing nonviable cells and debris is critical, as dead cells can affect productivity by decreasing the product-producing biomass and degrading the product via the increased release of proteases into the media. In CHO bioprocesses, dead cells can make up as much as 30% of the total produced biomass [64]. A cell retention device that can simultaneously remove small (<10 μm) nonviable cells was demonstrated using microfluidic devices [49]. Despite the size overlap between viable and nonviable cell populations, the devices demonstrated 3.5-28.0% dead cell removal efficiency with 88.3-83.6% removal purity and 97.8-99.8% live cell retention efficiency at 4 million cells/mL. Cascaded and parallel configurations increased the cell concentration capacity to 10 million cells/mL. Although

the removal efficiency is low, the effect compounds over several weeks of the perfusion process and will remove a significant number of nonviable cells from the bioreactor. Therefore, a healthy culture can be maintained without active bleeding, which is required for microfiltration-based methods.

For most industrial processes, cell separation on a milliliter scale is insufficient. Effective cascading is needed to increase the flow rate. Besides, high cell concentration leads to a severe increase in cell-to-cell interactions and might cause microchannel clogging. The microchannels might need to be scaled up to process higher concentrations [65].

1.1.1.4 Summary

Table 1 outlines the various cell retention devices compared in this chapter. The clarification efficiency is determined by measuring the turbidity difference or the pressure change between the inlet and outlet of the retention device. When ATF and TFF cell retention devices are employed, no additional filtration is required between the bioreactor and the capture chromatography step as the outlet turbidity is lower than 10 NTU (not shown in the table). Other cell retention methods call for additional filtration to avoid chromatography column clogging.

Table 1 Cell retention devices and their application in continuous CHO cell culture processing with the traditional non-continuous disk stack as a comparison

System	Max VCD ($\times 10^6$ cells/mL)	Processing rate (mL/min)	Clarification efficiency (%)	Yield (%)	Advantage	Disadvantage
Retention mechanism: Centrifuge						
Traditional non-continuous disk stack CSA-1 [57]	11.1	200–1000	82–94 (<20 psig*)	96	High separation efficiency	Cell lysis, complex devices, moving parts, high maintenance cost, high initial expense, limit to particle >1 μm
Ksep [24], [66]	5.4	180	88.2–93.4, (<20 psig)	95.7–98.7	Retain cell viability, washing option, single-use inserts	Cell losses during bed formation
Centritech Lab II [67][68]	13	108	45–89		Single-use inserts	Long residence time
Continuous disk stack CFD-130 [69]	9			87.6	Adaptive feedback-control scheme, constant downstream flow	Cleaning and maintenance, further filtration
Retention mechanism: Filtration						
Spin filter [55]	20		82.5	100	No product retention	Fouling, and lower cell density, require active bleeding
TFF ReadyToProcess™, KrosFlo, Pellicon, PuroSep [36]	214	300-1000	<14 psig	99.5	High cell capacity	Shear, product retention, require active bleeding, high run cost

XCell ATF® System [36][55]	132	700-1000	<7 psig	99.5	Self-cleaning, less fouling	Low cell capacity, requires active bleeding, high run cost
Retention mechanism: Acoustic						
Biosep [70]	125	7		98	No moving components	High risk of cell accumulation, retention efficiency adversely influenced by cell concentration
FloDesign Sonics [71]	75	56-194	90-94	>90	Single-use, continuous harvest	
Cadence [58]	100	60	>86	>90		
Retention mechanism: Flocculation [59]						
pDADMAC [59]	96	10	>90	97	Broad cell density range	Bulky bioreactor, residual flocculant
Retention mechanism: Hydrocyclone [61]						
Hydrocyclone [61]	50	500 (40/77 with pump)		95	Natural bleeding, high capacity, no moving components, disposable at a reasonable cost, separation efficiency independent of cell concentration	Limited performance optimization, noncontrollable bleeding, not suitable for lab-scale, hyperosmotic shock
Retention mechanism: Microfluidic [50]						
Microfluidic [50]	23	0.5		82	Controlled bleeding, simple scaling, passive operation, minimal maintenance	Cell debris aggregation, non-rigid device, limited flow rate, clog at high cell density

*psig, pressure unit, pound/square inch [gauge], 1 psig = 1.082198 Bar.

Examples of the operation of CHO perfusion processes are listed in Table 2. The perfusion rate is expressed in specific rates, *i.e.*, the volume of medium per bioreactor working volume per day (vvd; [d^{-1}]), or by cell-specific perfusion rate (CSPR), *i.e.*, the daily medium supply per cell in a continuous process. A lower CSPR indicates that the product is highly concentrated and a lower harvest volume needs to be processed in the downstream. The mAb production rate is compared using cell productivity. In the production phase, cell productivity was comparable for ATF, TFF, and spin filter systems, while the CSPR was lower for TFF and ATF systems, with the CSPR in these two systems being comparable. The relatively low cell productivity in perfusion bioreactors using microfluidic cell retention devices is related to the low flow rate required to maintain certain separation efficiencies, which could be improved by cascading. And less than 1 vvd perfusion rate indicates that the bioreactor is not fully used, as observed in the HC retention device, which was chosen to avoid possible hyperosmotic shock from a spiked feed medium [61].

Table 2 Example of cell retention with perfusion bioreactor for stable operations with CHO cells.

Retention device	Biomass control	Viable cell densities (10^6 cells/mL)	Perfusion rate (vvd, 1/day)	CSPR (pL/cell/day)	Steady-state duration (days)	Cell productivity pg/cell/day
TTF ATF [36], [72]	Daily	20-214	1.2-3.9	55-60	14-17.1	9-13 @25 ×10^6 cells/mL
		20-36	1.2-1.5	55-70	6.5-16	
ATF[73]	Off-line measurement and/or online capacitance probe	50-60	2-3	40-50	45	13-16
TTF ATF [52]	On-line biomass sensor, dielectric spectroscopy	20 / 60 / 40	1.42 / 1.1 / 1.28 1.44 / 1.06 / 1.28	72 / 18 / 32	10	11 / 7.5 / 5.7
Spin filter ATF [55]	Daily	16 40	1 2	63 50	20 35	10-12
ATF [38]	Off-line measurement and/or online capacitance probe	30	2	66	30	33
HC [61]	Daily	50	0.25	10	8	4
Acoustic [58]		100	2	2	60	
Microfluidic [50]	Daily	22.7	2	88	9	4

1.1.2 Challenges in implementing integrated continuous processes

Continuous processing provides much higher productivity by running small chromatography columns in multiple cycles, easing the scale-up challenges associated with large columns (compression of resin media and nonuniform flow distribution) [74]. The proper implementation of continuous manufacturing requires a thorough understanding of the process to achieve and maintain steady-state conditions.

Full-scale optimization for integrated processes is difficult, with the cost increasing rapidly with the number of operation units. Typically, many individual batch operations are optimized separately and are run in succession continuously. However, scheduling constraints on batch operations are frequently encountered, and surge tanks are frequently used. While the inclusion of surge tanks seems to contradict the motivation of continuous processing, as a properly designed continuous process should have all steps perfectly synchronized and controlled [75], the use of surge tanks is essential in integrating unit operations to smooth the intermittent output and to compensate for differences in flow rate in unit operations (*e.g.*, a multicolumn system).

Upstream operations are prone to numerous deviations that originate from the inherent complexities of culture processes [76]. The ability to quickly identify any sign of deviation allows for in-time adjustment of the process parameters. However, the time required for analysis is usually higher than the time for decision-making [15]. Therefore, there is a critical need for monitoring tools that can track multiple quality attributes rapidly to enable real-time decision-making.

1.2 CQAs for mAb production

IgG1 mAbs are glycoproteins with a molecular mass of about 150 kDa and typically consist of two light chains (LCs, about 25 kDa each) and two heavy chains (HCs, about 50 kDa each), which assemble during culturing via the formation of intermolecular disulfide bridges [1] (structure shown in Figure 3). A typical post-translational modification (PTM) of IgG1-type mAbs is the N-glycosylation at the conserved site Asn297. This N-linked glycan consists of a biantennary glycan but varies widely in its exact structure. Commonly, the most abundant N-glycans consist of a biantennary structure built by galactoses, mannoses, and N-acetylglucosamines. Throughout this work, adalimumab (Humira), a recombinant monoclonal IgG antibody drug frequently used in the treatment of auto-immune diseases such as rheumatoid arthritis and Crohn's disease, will be used as the model biologic molecule. Adalimumab binds and neutralizes the inflammatory cytokine TNF-α with high affinity and specificity [78]. Glycans in adalimumab contain principally bi-antennary non-sialylated complex-type N-glycans with little or no high-mannose type or sialylation. Figure 4 depicts the acceptance criteria for glycosylation of the US-licensed adalimumab composition.

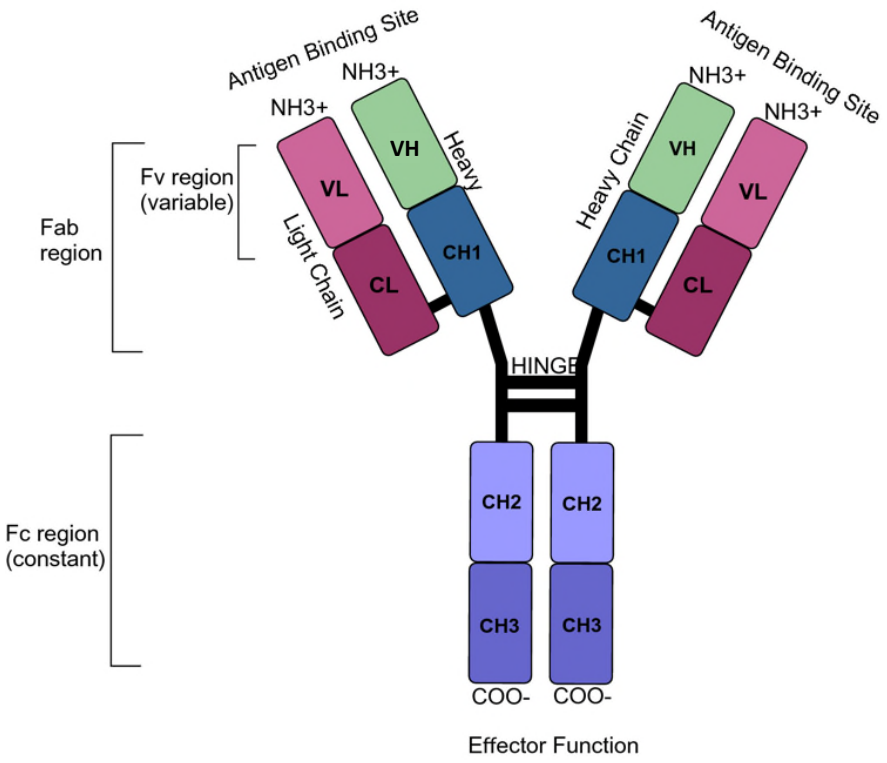

Figure 3 Schematic structure of a human IgG1 antibody [77]**. IgG consists of two heavy and two light chains. The variable domains are variable light (VL) and variable heavy (VH), which form the antigen-binding site. The constant domains are CL (constant light) and CH1–3 (constant heavy). IgG can be furthermore divided into Fab (fragment antigen binding), which consists of Fv (fragment variable) and Fc (fragment crystallizable) that induce effector functions.**

CHO cells do not possess a cell wall that reinforces the cells; thus, they are very sensitive to culturing process parameters such as pH, temperature, and media composition. The prolonged culturing in perfusion culture makes the continuous process more susceptible to varying culture conditions. As a result, the expressed mAb species vary with the change in bioprocess conditions, resulting in mAb of various forms of microheterogeneity, such as mass, size, charge, hydrophobicity, degradation/aggregation, glycovariants, and other attributes, secreted into the cell culture. For example, culture osmolality was shown to promote oligomannose variants [79], [80], and media supplements, such as the addition of galactose and manganese, are known to result in a decrease of oligomannose variants and

a simultaneous increase in levels of galactosylation [81]. It is therefore very important to monitor the mAb product to ensure that no undesirable structural changes are introduced. Variations in molecular charge may influence antibody binding affinity, and thus affect potency, aggregate formation, serum half-life, or stability upon storage of the drug product. The changes in glycosylation affect the structure and function of the protein, which may also affect its mechanism of action, efficacy, stability, half-life, and immunogenicity [82]. Specific glycosylation patterns (*i.e.*, the composition of attached sugar moieties) of antibodies can also be used as an indicator of a consistent manufacturing process or to identify the effect that changes to the manufacturing process have on the molecule. Characterized by the degree of galactose sugar molecules, one of the major glycoforms of mAbs, including adalimumab, is the agalactosyl fucosylated biantennary oligosaccharide (G0F) species that contains fucose but no terminal galactosylation [83]. Evidence that glycosylation patterns affect protein function is accumulating, and differential glycosylation has been shown to influence serum clearance in human studies of therapeutic antibodies with oligomannose sugars [84], antibody-dependent cell-mediated cytotoxicity or complement-dependent cytotoxicity [85], and serum half-life due to differences in binding to the Fc receptors [86]. For example, the presence of fucose, galactose, and sialic acid strongly affects antibody-dependent cellular cytotoxicity, complement-dependent cellular cytotoxicity, and immune modulation of the mAb, respectively [87]. High mannose glycoforms are reported to reduce serum half-life [88]. However, rapid monitoring of the cell culture process as well as accurate quantification of glycoforms and other protein variants remain analytically challenging.

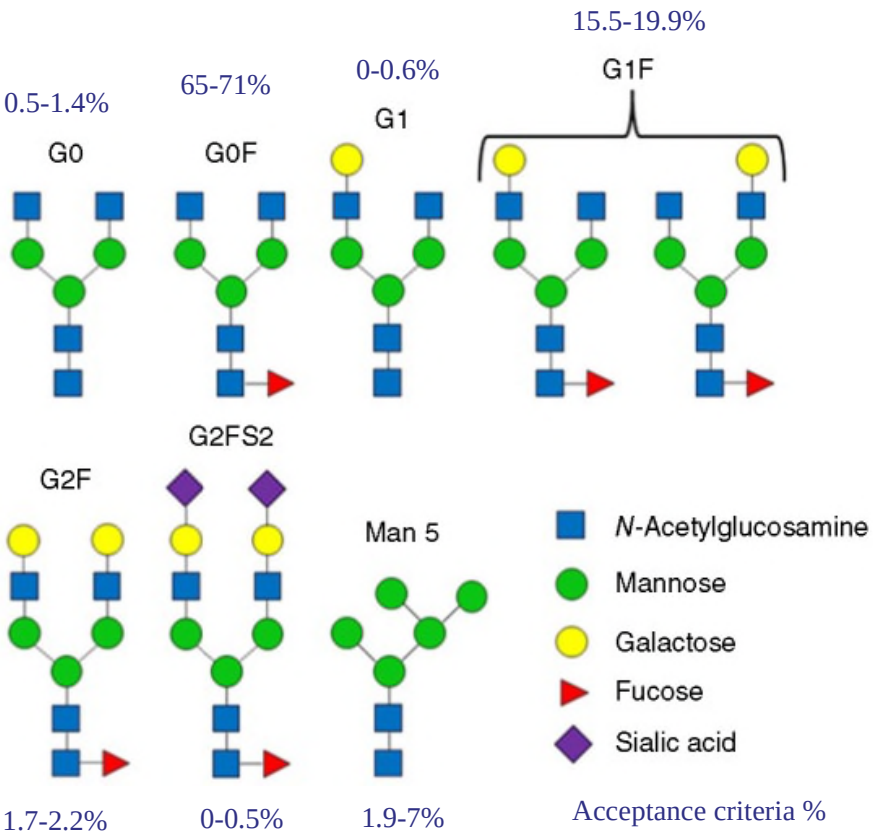

Figure 4 N-linked glycan profiling of US-licensed adalimumab [89]**.**

Therapeutic proteins possess structural features that, if modified even slightly, may affect clinical performance. Consequently, quantification of the breadth of physicochemical and biologically based attributes is needed in order to maintain product quality. To accomplish this in large-scale manufacturing processes, it is important to understand which molecular characteristics are most sensitive to various production process factors. A complete mAb glycosylation analysis must include the identification of sugar chains attached to glycosylation sites (macro-heterogeneity) and of the sugar moieties within the glycan chain (micro-heterogeneity). Specific glycosylation patterns (*i.e.*, the composition of attached sugar moieties) of antibodies can also be utilized to identify the influence of the changes in the manufacturing process have on the molecule [90]. Besides constant monitoring of

bioprocess parameters such as viable cell count, metabolite and nutrient concentrations, and IgG titers, a complementary analytical assessment of product molecular attributes (*i.e.*, subunit assembly or glycosylation profile) is not well established routinely. In biotechnological facilities, glycosylation is typically assessed at the end of the process unit operations due to the complexity of such analyses, which usually involve purification from cultivation media and analysis downstream of the culture process by a plethora of analytical methods such as released glycan profiling upon enzymatic release, peptide mapping, or subunit analysis employing different analytical techniques such as HPLC or capillary electrophoresis (CE) with UV or mass spectrometric detection. These approaches involve time-consuming sample preparation steps and bear the risk of introducing artificial modifications. Furthermore, these multistep procedures are incompatible with in-line process control and screening.

1.3 Online/In-line Monitoring of the upstream process

The development of cell culture processes drives a large portion of cost-savings, as optimizing the upstream process can yield significant increases in protein production. The optimization of these processes can prove to be complex, as there are an innumerable number of parameters that can be adjusted. Equally complex is the number of indicators that can be measured to monitor the cell's health, titer, and product quality attributes. Many of these indicators require manual sampling and handling of the bioreactors, which can become tedious as the number of desired measurements increases. PAT features the incorporation of analytical techniques into development or manufacturing processes in an in-line, online, or at-line fashion. In-line sensors are generally directly connected to the bioreactor and do not require any form of sample extraction from the process stream.

Online tools are integrated into the bioreactor system, *i.e.*, lying outside the bioreactor, requiring an automatic sampling interface to the bioreactor that enables a sample to be drawn and delivered to the analyzer and can continuously analyze the data. In contrast to conventional offline testing, which requires a sample to be taken off the system and analyzed remotely in the laboratory after proper pre-treatments (*e.g.*, dilution, filtration, or digestion), at-line technologies typically involve manual sampling and analysis with the sensor module lying in close proximity to the production process. Online measurements of the product parameters in the cell culture medium are not widely implemented and limit our ability to have a live snapshot of the culture process.

Compared to the conventional batch process, which typically lasts only about 14 days, cell cultivation in continuous processing can proceed for up to 100 days [91], requiring sampling throughout the process. The cell culture is a rather complicated sample matrix containing not only the fully formed mAb but also intermediates and degradation products, host cell proteins, metabolites, and cell medium components. Biotherapeutic manufacturers are keen to generate higher titers with high mAb concentrations at the upstream stage as a part of process intensification. However, highly concentrated formulations are more susceptible to biomolecular aggregation, leading to highly turbid and viscous solutions, which pose more challenges for concentration measurements.

Real-time biomass sensor technologies have been developed using the dielectric properties of living cells. Parameters that can be measured in real-time include viable cell density (VCD), oxygen uptake rates, and concentrations of the key metabolites, including glucose, lactate, glutamine, other amino acids, and ammonia. Many online spectroscopy tools investigated recently can noninvasively and nondestructively measure multiple parameters

simultaneously. Raman spectroscopy provides in-line process-state estimation, including mAb titer measurement. Spectroscopic methods (*e.g.*, NIR, FTIR, mid-IR, Raman [92], fluorescence) and mass spectrometry, including matrix-assisted laser desorption/ionization mass spectrometry (MALDI-MS) [93], can measure a broad range of analytes, including the nutrients, metabolites, and cell concentrations in cell culture broth [94]. The accumulation of the scattering compounds in bioreactors, such as cells, cellular debris, or mAb aggregates, may induce modifications of the scattered light reaching the detector, resulting in nonlinear spectra slope changes. Perturbations due to the dynamics of the cell culture are also a concern. Real-time online monitoring of an ongoing CHO cell culture process is not readily feasible, and elaborate sample preparation is often required. The challenge moving forward will be incorporating spectroscopic methods into perfusion bioreactor monitoring.

To compare different spectroscopic methods based on their detection sensitivity of IgG in water, the molecular cross sections, extinction coefficients, and water absorption coefficients are listed in Table 3. Further calculation information can be found in this paper [95]. This table compares the scattering cross-sections to understand the sensitivity of the various spectroscopic approaches. However, the solvent water in the vicinity must also be considered. It is advantageous to achieve a high ratio of protein scattering cross-section to water absorption. Table 3 provides information on the measurability of a certain protein concentration in water with the selected spectroscopic method. Generally, it is important to examine the protein and water absorption ratios in the wavelength range used by a certain spectroscopic method to draw the right conclusions.

1.3.1 Mid-infrared (MIR) spectroscopy

MIR spectroscopy is gaining popularity in monitoring product quality and impurities due to instrumentation improvements and especially automated water background corrections. Water is an integral component of all bioprocessing systems. A strong mid-IR spectral absorbance of water at 1600 cm^{-1} tends to overlap with major spectral signatures of proteins corresponding to the Amide I (1700^{-1}, 600 cm^{-1}) and Amide II (1600 and 1500 cm^{-1}) regions [96], interfering with conventional analytical calculations based on infrared measurements, sometimes to the extent that the determination of quantitative information from such measurements is not possible. However, modern mid-IR spectrometers are capable of automatically subtracting water absorbance as part of the background correction performed during spectral acquisition (Bruker Matrix MF®, Mettler Toledo ReactIR®). In-line monitoring of protein concentration, aggregation, charge variants, and HCPS in a perfusion bioreactor at high cell density was accomplished by the incorporation of mid-IR probes using flow cells for real-time acquisition (10-20 s per measurement) followed by multivariate data analysis [97]. In addition, this system can analyze a series of different analytes, for example, product and intermediate components, waste products, residual reagents, and buffer components. However, these measurements were carried out with Fourier transform infrared spectroscopy (FTIR), which is not entirely suitable for bioprocess monitoring due to moving parts and vibrational sensitivity [98].

Despite the fact that the background from water absorption can be subtracted, water absorption in this region can be 100-fold greater for dilute protein concentrations (Table 3). Consequently, MIR is not well suited for protein quantifications below 1 mg/mL [99]. Additionally, the temperature sensitivity of the OH bands is a severe drawback for measuring in an aqueous solution with MIR, which makes tempered sample holders

necessary [100]. Due to the overlapping absorptions, highly convoluted and similar spectra are observed for proteins, and advanced data analysis is required to extract the useful information.

Table 3 Molecular cross sections and extinction coefficients (if applicable) of IgG measured with different spectroscopic techniques [95]**.**

Spectroscopic method	Cross section σ as $-\log(\sigma/(\mathrm{cm}^2\ \mathrm{molecule}))$	Absorption/emission coefficient L/(g·cm)	Extinction coefficient of water cm^{-1}
UV (280 nm)	16	1.2 to 1.5 [101]	$2.6 \cdot 10^{-3}$
Fluorescence	17	0.16 to 0.2 [102]	$1.3 \cdot 10^{-3}$
NIR	16	1.2 [103]	25.6
MIR	15	12	1400
Raman (532 nm)	27	–	$4.2 \cdot 10^{-4}$
Resonance Raman (229 nm)	25 [104]	–	$6 \cdot 10^{-3}$
Rayleigh (633 nm)	18-19	–	$3 \cdot 10^{-3}$

1.3.2 Near-infrared (NIR) spectroscopy

NIR spectroscopy has been proven useful for monitoring animal cell cultures under the PAT approach. Due to the complexity of the NIR spectra in scattering systems and the need for chemometric approaches tailored to such systems, the key to implementing this method is to develop an acceptable regression method that can extract the information from the spectra and overcome the nonlinearity issue during the calibration process. Near-infrared spectroscopy has been used to measure the concentration of mAb in the harvested broth in real-time (every 3 s) with ± 0.05 mg/mL accuracy [105]. The use of *in situ* NIR spectroscopy with the locally weighted regression (LWR) method to monitor mAb

glycosylation has been reported for the real-time calculation of the concentrations of main culture medium components (viable cells, glucose, lactate, glutamine, and mAb) as well as of the NG-mAb in batch and feed-harvest modes [106]. The same group later employed LWR and support vector regression (SVR) for in-line real-time monitoring of glycosylation, in terms of high mannose isoforms, fucosylated, sialylated, and galactosylated isoforms, as well as non-glycosylated mAb at concentrations down to 30 mg/L [107]. These results represent a further step toward developing active control feedback for animal cell processes, particularly for ensuring the properties of biologics. Overall, the results demonstrated that in situ NIR spectroscopy has the potential to be a PAT tool when culture dynamics and nonlinearity are adequately considered via spectroscopic calibration models.

The water absorption spectrum is dominant over protein absorption in the NIR region, similar to the MIR region, and the tempered sample holders are also necessary. While NIR spectroscopy has the advantage of having no moving parts, however, the selectivity is generally low due to the superposition of different overtones and combination bands in the NIR region. The NIR band intensities are much weaker than their corresponding MIR peaks by a factor of 10 to 100, depending on the order of the overtone [108].

1.3.3 Raman spectroscopy (RS)

Raman spectroscopy is a ubiquitous multipurpose analytical technique in biopharmaceutical manufacturing for real-time measurements of critical process parameters in cell culture. RS measures the energy of the inelastic scattering of photons by analytes. The shifts in wavelength from the excitation wavelength of a monochromatic

light source correlate to the vibrational energies of chemical bonds. A molecule can have multiple vibrational modes, each causing characteristic scattering and resulting in multiple Raman peaks that provide rich spectral information. RS has garnered significant interest and has become an excellent candidate for quantitative real-time monitoring of bioreactor systems due to its accuracy, especially in aqueous systems, such as cell culture media. Raman spectra have sharper and better-resolved peaks than NIR. They do not show strong interactions with water, but due to very small protein scattering cross-sections (Table 3), the water bands are dominant for dilute protein solutions. Therefore, the resonance enhancement effect in the UV range is often utilized for protein structure studies [109]. The resonant effect of the Raman scattering in the UV region, referred to as UV resonance Raman (UVRR), is caused by the absorption of aromatic amino acids or the polypeptide backbone of proteins. The Raman cross-section of the modes coupled to these resonant electronic transitions can increase by a magnitude of five [104]. The high sensitivity of the Raman spectra allows multiple analytes to be analyzed in cell media at the same time, allowing accurate monitoring of a wide range of key components present in cell culture. However, the complicated fingerprint of all spectral contributions from the protein and formulation components presented in the spectrum makes identifying a single peak connected with a specific CQA extremely difficult. Furthermore, it is crucial to protect the bioreactor from daylight and, even more so, artificial light during spectra acquisition, as both contribute to intense and acute emissions in the Raman spectra with a variance greater than that of the antibody titer.

Prediction of IgG concentration was demonstrated using an in-line RS probe directly in the cell-free permeate stream of a perfusion system [110]. Combined with PLS, this system

was capable of accurately predicting the concentration trend and values of different mAb isotypes with average prediction errors of 0.2 g/L throughout cell culture every 15 minutes without sampling. In situ Raman spectroscopy combined with appropriate chemometric methods was demonstrated to distinguish glycosylated from non-glycosylated molecules in real time [111].

The accuracy of RS relies on chemometric models, which need careful calibration, and its implementation is nontrivial as it necessitates executing multiple designed experiments to generate relevant calibration sets [92]. The calibration models are reliable only under the operating conditions in which they were calibrated, posing a unique challenge in clinical manufacturing if the products have a limited production history. When UVRR is used, there are some drawbacks, like photodamage due to exposure to UV light or a loss of linearity between the signal intensity and the concentration of protein due to the reabsorption of photons [99].

1.3.4 Surface plasmon resonance (SPR) spectroscopy

SPR spectroscopy is a label-free technique for real-time measurements based on refractive index changes at the sensor surface, where one binding partner is immobilized and interacts with the analyte in solution. SPR spectroscopy was utilized to detect total as well as bioactive mAb concentrations using amine coupling [112]. The specific nature of the binding used allowed for direct measurement of untreated samples. SPR measurements have been shown to determine 100 samples in 16 hours, with hands-on time of approximately 1 hour and automated analysis overnight. SPR technique also has the

advantage of bioactive surface regeneration, and it is possible to use a functionalized sensor surface over one month, and over 1000 binding cycles can be conducted.

A novel fiber-optic nanoplasmonic sensor technology was explored for rapid IgG titer measurements in samples from filtered, unpurified CHO cell cultures [113]. LSPR is the result of collective electron oscillations in noble metal nanoparticles, such as gold nanoparticles (AuNPs). Irradiation with visible light produces a pronounced extinction band, the position of which is highly dependent on the refractive index in the vicinity of the nanoparticle surface. Binding of mAbs to ligands (e.g., Protein A) immobilized on the nanoparticle surface results in a concentration-dependent shift of the LSPR band that can be measured spectroscopically. Compared to benchtop surface plasmon resonance (SPR) sensor systems, LSPR sensors require significantly less complex optical setups and are less sensitive to temperature fluctuations and changes in the sample matrix composition. The sensor requires small sample volumes (1-150 µL) and shows a reproducibility and sensitivity comparable to Protein G HPLC-UV. The dynamic range of the sensor system can be tuned by varying the sample volume, which enables the quantification of IgG samples ranging from 0.0015 to 10 mg/mL, without the need for sample dilution. A real-time online operation can be achieved when combined with an auto-sampler that diverts or collects and directs cell-free samples from bioreactors into the flow cell. However, nanoparticle mediated ligand-receptor binding displays a particularly complex behavior that arises from the confinement of the molecular species on a small surface. The chemical equilibrium between ligands and receptors can be locally disturbed by the inhomogeneous species concentration, resulting in an effective affinity that is highly dependent on the local environment and the nature of the confinement. Predicting the outcome of LSPR in nano-

structures is therefore a difficult task requiring extensive experimental data. Furthermore, protein immobilization affects conformational and rotational entropy, therefore, the effective affinity in AcNPs is often determined by the orientation and density of antibodies on the surface, as these molecules are large voluminous ligands.

1.3.5 Fluorescence spectrometry

Fluorescence spectroscopy exhibits little interference from water, with absorption and emission coefficients comparable to those observed in the NIR and MIR regions. Therefore, it is possible to quantify proteins in the mg/L range using fluorescence spectroscopy [114]. Rarely, deviations from the Beer-Lambert equation, such as adsorption to the cell walls, can alter the quantification limits [115]. Light absorption in the sample leads to the inner filtering effect, which distorts emission intensities and spectra, leading to a nonlinear connection between fluorescence intensity and protein concentration [116]. Due to the inner filtering effect, intrinsic fluorescence spectroscopy only behaves linearly at low concentrations (absorbance less than 0.05) when measuring proteins. Continuous, uninterrupted, fast, and specific detection of antibodies was demonstrated using simple fluorescence-based monitoring instrumentation, which allows process control using fluorescence intensity to reduce IgG loss in purification [117]. Adjustable sensitivity down to 1 μg/mL (~6 nM) of IgG was achieved with soluble fluorescein-labeled Fc-binding ligands that produced an immediately-detectable shift in fluorescence polarization and intensity. To extend the upper limit of the inlet flow rate required in continuous manufacturing, flow-splitters were utilized with an inlet flow of 15 mL/min, producing a sampling stream at 1 mL/min while still enabling continuous detection. However, if applied

in continuous processing, the 90 minutes delay caused by fluorescent dye labeling needs to be taken into account.

1.3.6 Ultraviolet and visible (UV/Vis) spectroscopy

UV spectroscopy observes the electronic state transition. The peptide backbone, aromatic amino acids (tryptophan, tyrosine, and phenylalanine), and disulfide bridges formed by the oxidation of two cysteine residues are the most prevalent chromophores in proteins [116]. In addition, UV spectra provide information on protein folding (through wavelength shifts of the relevant chromophores) and aggregation (by light scattering), despite the fact that these diverse energy states overlap with the broad electronic absorption spectra typically found in solution [116]. The spectrum information can be utilized in conjunction with multivariate data analysis tools, such as partial least squares (PLS) models, to deconvolute several species. Similar to fluorescence spectroscopy, UV spectroscopy can be used to quantify proteins in the mg/L range. UV spectroscopy often has a larger, but still limited, linear range compared to fluorescence spectroscopy [118]. The introduction of variable pathlength (VP) UV spectroscopy enables an increase in the dynamic range of the concentration measurements (as seen in these two commercial instruments, FlowVPE and SoloVPE) [119]. FlowVPE, using an automated version of a flow cell, can be employed in-line for the majority of flow rates. By varying the vertical position of a fibrette inside the sample, the slope of the absorbance/pathlength curve can be measured and thus the product concentration inferred [120]. Absorbance is measured through a fiber optic cable connecting the VPE unit to a separate Cary 60 spectrophotometer from Agilent Technologies. SoloVPE is currently used to measure purified product concentration. Real-time monitoring and control of the loading phase of a Protein A capture step was

successfully realized using UV/Vis spectroscopy to quantify mAb in the effluent despite the background of many protein- and non-protein-based impurities [121]. Another drawback of UV/Vis spectroscopy is the limited selectivity for different protein features [99]. To improve the prediction of UV-based approaches and compensate for their lower selectivity, researchers have developed dynamic background subtraction techniques to eliminate the influence of process-related impurities on the UV spectra [121].

1.3.7 Nanofluidic system

Developed in our group previously, nanofluidic devices consisting of a periodically patterned and slanted nanofilter array demonstrated continuous multivariate quality analysis of multiple therapeutic proteins with high detection sensitivity and simple operation [122]. Integrated with a membrane-less microfluidic cell retention device, a nanofluidic system was applied for continuous and automatic monitoring of protein product size and quantity directly from the culture supernatant during a high-cell-concentration CHO cell perfusion culture [123]. This system offered many unique advantages, including an automatic microfluidic liquid handling system, reduced design complexity, lower cost, much less manual operation, and high data throughput, ultimately enabling the monitoring and optimization of even many concurrently running bioreactors in process development. The chemical and mechanical robustness of the nanofluidic device enabled continuous monitoring for several days to a week. The separation resolution of the protein can be improved by adjusting the gap size of the nanofilter array. Silicon dioxide was used to insulate the nanofluidic device (500 nm thick), which might be damaged by long-term exposure to chemical reagents, electric field, and repeated mounting and unmounting of the device on the solid device holder. Alternatively, whole-glass nanofluidic devices [124]

could eliminate the breakdown issue of the insulating layer, which significantly improves device durability and operation time for long-term monitoring. The unoptimized online sample preparation caused about a 5-hour time delay, which could be reduced by using microfluidic devices for sample preparation to minimize hold-up volume. Further reduction in the sample preparation complexity and time can be expected by using label-free protein detection methods.

1.4 At-line monitoring of the upstream process

1.4.1 Flow-induced dispersion analysis (FIDA)

FIDA is based on Taylor dispersion analysis (TDA) in narrow fused silica capillaries and provides the hydrodynamic radius of the binding ligand and complex in addition to the detailed binding characterization. FIDA methods are implemented in fused silica capillaries with an internal diameter of 25-100 μm which requires accurate pressure control in the millibar range, as well as optical detection based on UV-vis or fluorescence. The FIDA assay utilizes a small fluorescently labeled anti-IgG affibody as the selective mAb binder in-solution and requires only nano/microliter sample volumes. Quantification of mAb directly (no sample pre-treatment) in mammalian cell culture is rapid (4 minutes of analysis time) with nanomolar sensitivity (the author claimed that the limit of quantification is 0.9 nM, defined as 10 times the relative standard deviation of the blank sample, while in this paper, the tested samples have concentrations of 1.22 mg/mL and 1.41 mg/mL) [125]. Nonetheless, this method requires considerable liquid manipulation at precise time and pressure, including cleaning and equilibrating with buffer, analyte, and indicator injection. The demonstration of continuous operation has not yet been achieved.

With a suitable in-solution sampler, automated device preparation, and sampling loading mechanism, it may be possible to apply FIDA for the online determination of the antibody titer in CHO cell cultures.

1.4.2 Mass spectrometry (MS)

Bottom-up (BU) is by far the most widespread method in MS-based protein analysis [126]. In this technique, protein samples are digested by one or more proteases, the resultant peptides are separated by liquid chromatography (typically reversed-phase high performance LC), and the masses of the peptides are recorded. Highly abundant precursor ions are then selected for fragmentation, and the masses of their fragment ions are recorded. Additionally, both denatured and native antibodies can be fragmented to produce sequence information; this technique is known as top-down (TD) mass spectrometry. These intact-protein fragmentation spectra are more complex and difficult to interpret than peptide spectra due to the significantly bigger size and greater charge of the studied species [127]. Utilizing specialized proteases to split proteins into smaller subunits helps reduce this issue. This technique is referred to as middle-down (MD) MS, and in the context of antibodies, it is often accomplished by cleaving the hinge region of the heavy chain prior to MS analysis [128].

Matrix-assisted laser desorption/ionization (MALDI)-MS was used to determine the IgG1 concentration semi-quantitatively in the media supernatant without prior purification steps every working day [93]. This platform relies on capillary electrophoresis-electrospray ionization (CE-ESI) to separate biomolecules and microfluidic technology to eliminate sources of extra-column band broadening [129]. The recorded mass spectra also provide

information about the antibody integrity and presence of host cell protein contaminants. Aside from the entire IgG1 at 150 kDa (at the concentration of 0.2 mg/mL), fragments of 23 and 47 kDa were detected. Typical mass spectrometric detection focuses on released glycan profiling upon enzymatic glycan release, peptide mapping, or subunit analysis [130]. Intact mAb glycan analysis requires less sample processing, but centrifugation followed by high selectivity separation such as electrophoresis or chromatography is still required in order to assess the presence of mAb variants (heavy chain, light chain, glycosylation variants) due to the complexity of the bioreactor sample. For example, at-line quantitative profiling of intact mAb products during bioprocessing using HPLC-MS has been demonstrated, which employed ion-pair reversed-phase (IP-RP)-HPLC separation of mAb, light chain, and its dimer in the cell culture [131]. The complex raw data generated by HPLC-MS analysis of intact proteins require extensive data evaluation and processing, and the system itself is costly and requires multi-step manual sample preparation [131].

The repertoire of antibodies consists of many proteins that typically differ in only a small region of their protein sequence. Analyzing antibodies with MS-based technologies poses preanalytical (*e.g.*, sample preparation), analytical (detection limit and sequence coverage), and computational difficulties. Knowledge about how the separation of mAb fragments affects the ultimate experimental outcome remains somewhat limited [132].

1.5 Summary

Efforts have been made to shorten the turnaround time of current analytical methods in response to the rising demand for PAT instruments in bioprocessing. Various analytical

instruments have been utilized to allow the deployment of online/in-line monitoring of cell culture media, bioprocesses, and macromolecule properties, as summarized in Table 4. As noted above, a number of existing analytical techniques have been investigated as prospective PAT systems for continuous biomanufacturing. These techniques provide extremely valuable structural and molecular-level information about the solute and the drug molecules (summarized in Table 5).

The spectroscopic approaches are noninvasive and capable of measuring more analytes at a frequent rate, which holds additional promise over these automatically sampled systems that require the withdrawal of culture from the bioreactor [91]. Infrared spectroscopic measurements generally provide information regarding the vibrational properties of analytes such as reaction products and by-products in process fluids within biomanufacturing systems. Although other measurement techniques, such as Raman spectroscopy, can also produce essential information about these analytes, infrared measurements can offer distinct advantages in some situations. Typically, measurements of infrared spectroscopic information can be completed faster (*e.g.*, in 30 seconds or less) than matching Raman measurements, which can take between 10 and 15 minutes. Consequently, infrared measurements are more suitable for real-time or near-real-time process monitoring and control applications. In addition, infrared spectroscopic measurements can be more sensitive than Raman measurements to changes in analytes and the characteristics of process fluids. Taking into account the rate at which such measurements can be done, infrared spectroscopic measurements may be more suited for higher throughput applications during active monitoring of biomanufacturing processes. In addition, infrared spectroscopic measurements are typically less susceptible to changes in

ambient circumstances that occur throughout the measurement process. Infrared spectroscopic measurements, for instance, are often less sensitive to fluctuations in temperature, humidity, and ambient light than Raman measurements. Consequently, once calibrated, chemometric models based on such measurements can be utilized in a wider range of settings and may be easier to transfer from a laboratory to a high-throughput production operation. However, there are obstacles to the general implementation of these strategies. Due to the dynamic nature of the cell culture, in-line implementation remains a difficulty, as analyses are susceptible to disturbances. Indeed, scattering substances, such as cells, cellular debris, and mAb aggregates, are produced during growth. Their accumulation in the bioreactor may alter the scattered light reaching the detector, resulting in variations in apparent absorbance and, therefore, nonlinear spectral slope modifications. Due to the significant water absorption in the same range as the amide vibrational bands, accurate measurements of the peptide bond using FT-IR spectroscopy, specifically NIR, are hindered by water, a large component of the process flow (>90 percent). These effects, which produce or exacerbate nonlinear connections between spectra and chemicals, may restrict the applicability of conventional linear regression techniques, especially PLSR. Detecting and quantifying components in the mixture of a protein, protein aggregates, host-cell protein, *etc*., necessitates a considerable amount of effort, as well as specialized equipment and data analysis. Since the water signal does not interfere with the Raman spectra of the protein backbone, it is frequently regarded as the default PAT technique for continuous biomanufacturing [111]. Several drawbacks limit the scope of Raman spectroscopy for inline monitoring of the process flow. For instance, the low signal-to-noise ratio resulting from backscattering reduces the amount of Raman photons, the

distorting effects of fluorescence under laser irradiation, and the damaging heating of a material by the laser beam. Raman spectra of multicomponent biomanufacturing product flow are quite complicated, and their qualitative and quantitative analysis is not simple due to overlap. Optical sensors (NIR, Raman, etc.) must be incorporated into the process flow for accurate results; however, frequent cleaning and recalibration of these sensors disrupt continuous product monitoring. Protein concentration measurement using UV/Vis spectroscopy is currently only applied to purified products [120].

Other than the methods listed in the tables, low-field water proton nuclear magnetic resonance (NMR) under flow conditions (flow-wNMR) has been explored as a contact-free in-line PAT for continuous biomanufacturing [133]. The water proton transverse relaxation rate R2($1H_2O$) is sensitive to low levels of mAb aggregates, with larger aggregates causing a faster relaxation of the surrounding water molecules via proton exchange. The setup can detect variations in protein concentration (±1 mg/mL) and reasonably low levels of protein aggregates (±1%). The R2($1H_2O$) is sensitive to changes in protein concentration as well as aggregate content, but it does not distinguish between the two. Further experiments need to be conducted to show if this instrument can handle real-life supernatant samples. One could hypothesize that HCP and other components in the supernatant could interfere with the relaxation measurements. The interferometric reflectance imaging sensor (IRIS) system (similar to biolayer interferometry) has been used as a real-time and label-free method to detect IgG in aqueous solutions [134]. By performing kinetic characterization experiments, the sensor can measure IgG concentration in the range of 1–50 μg/mL with a high correlation coefficient value (> 0.94) and a low detection limit (0.25 μg/mL or 1.67 nM). Since protein A is used as the ligand, this method

should be able to detect IgG in the supernatant as well. Still, proper rinsing is required to remove the unbound residuals on the sensor surface, which can complicate the operation and potentially introduce uncertainties in the measurements.

Despite considerable efforts to improve the speed of IgG quantification methods, there is still a lack of robust, cost-effective sensor systems that allow for online, real-time titer measurements. The multistep nature of many of these technologies discussed in the above session makes the development and validation of new assays cumbersome. Surface-based technologies in general suffer from artifacts related to nonspecific surface adsorption, which complicate measurements in complex sample matrices such as supernatant. In continuous biomanufacturing operations, timely feedback is critical for operational control. Preferably, the feedback would be obtained in a contactless manner, which would greatly reduce the maintenance burden and thereby enhance the robustness of operation. Further, although the majority of the technologies can provide detailed information on protein isoforms, they do not provide functional information on the binding activity.

A nanofluidic device as an alternative monitoring system enables a comprehensive biologics quality assessment, including size, folding, and activity in the continuous manufacturing process. Simple operation, together with better performance in terms of detection sensitivity and resolution, make it a promising candidate for quality assessment well beyond that possible with conventional techniques. Stable operation over a long period of time can be achieved as the device is resistant to mechanical or chemical degradation. The short operational time (less than one hour) and minimal sample volume make the device ideal for on-site (point-of-care) biologics monitoring.

Online monitoring provides significant potential for process optimization and control. Measuring product quality and safety in real time can significantly alleviate the strain of process development. When implemented, online monitoring enables the fast acquisition of important information required for corrective action. Monitoring each step of the whole production chain in real time enables the identification of crucial process conditions and operating parameters for the succeeding unit. Additionally, essential process knowledge can be included to refine the entire procedure. For the selection of monitoring instruments, the correct identification of critical quality attributes and critical process parameters (CPPs) is of the utmost importance. By providing a continuous record of product quality throughout the production process, firms can adjust parameters through a single continuous experiment to assure consistent CQA without needing a full experimental design (DoE). Despite the high initial investment costs in analytical equipment, the implementation of online monitoring is worthwhile due to the possibility of increasing productivity and product quality, shortening processing time, and enhancing compliance with regulatory requirements for the production of drugs, food, and biopharmaceuticals.

Table 4 List of analytical methods for upstream (pre-Protein A) monitoring of cell and product attributes of mAbs production in the fed-batch process.

Attribute	Analytical methods	Mode	VCD ($\times 10^6$ cells/mL)	Phase	Data analysis	Specs, RMSEP @ range	Advantage	Disadvantage
TCD, VCD, DCD, viability	Capacitance sensor [135], [136]	Online	45/18	Exponential growth; multi-frequency: + steady and death [136]	PLSR, OPLS [136]	VCD > 5×10^5 cells/mL, 0.99 @ 18 $\times 10^6$ cells/mL	Scale-independent, probe-to-probe consistency, accurate, reduced cross-sensitivity to cell diameter changes	Limited permittivity signal in the steady growth and death phase, process-specific calibration, and scalability unknown [136]
	UV/VIS spectroscopy [137]	In-line	4–6	Exponential growth, steady and death	PLSR, MCR	VCD: 7.59 @ 50×10^5 cells/ mL, DCD: 3.65 @ 65×10^5 cells/ mL	Inverse cultivation protocol, accelerated experiment time, reduced sterility issues	Spectroscopic features not attributed to either viable or starved cell density, high order MCR model to handle nonlinearity, particle scattering, and band shifts

	2D-fluorescence spectroscopy [138]	In-line	0.3-32	Lag, exponential growth, and death	PLSR	TCD: 1.82 @ 38 $\times 10^6$ cells/mL, VCD: 2.15 @ 32×10^6 cells/mL, viability: 3.82 @ 100%	In-situ sterilizable probe distinguishes between viable cells, dead cells, and lysed cells, simpler data preprocessing, highly sensitive	Cannot distinguish between different forms of cell death such as apoptosis and necrosis
	Raman Spectroscopy [139]	In-line		Exponential growth	RT-JITL generic model	VCD: 1.17% RMSE, viability: 1.63% RMSE	Real-time automatic calibration, operative without interruptions during culturing, generic (applicable to cell culture involving different modalities, cell lines, media composition, and process and operating conditions)	More expensive
IgG titer	NIR spectroscopy: see Glycosylation							
	Raman Spectroscopy [140]	In-line	8		PLSR	0.29 @ 4.2 g/L	Scale-independent	The blinding effect caused by the presence of other analytes, Low SNR, nonspecific and less accurate PLSR titer models, system-specific sample sets

	Localized surface plasmon resonance spectroscopy [113]	Online (simulated)				LOQ: 0.0015mg/mL	Short response time (seconds to minutes) and a large and tunable dynamic range (0.0015 mg/mL - 30 mg/mL), less complex optical setups, less sensitive to temperature fluctuations and changes in the sample background	mAb binding depends on the surface concentration of immobilized ProtA and their relative orientation on the sensor surface
	Flow-induced dispersion analysis (FIDA) [125]	At-line				LOQ: 135 ng/mL (two orders of magnitude lower than HPLC)	4 minutes of analysis time, relatively simple operation, straightforward data analyzing (compared to spectroscopy and spectrometry)	Nonspecific surface adsorption
	2D-fluorescence spectroscopy (see Aggregation), NIR spectroscopy: see Glycosylation							
Aggregation	2D-fluorescence spectroscopy [141]	Online	1	Exponential growth	PLSR	ANS Extrinsic dye, mAb > 20 mg/L, aggregate: 1.7 @ 20-60 mg/L	Unaffected viability, negligible interaction of dye and media proteins	Reduced cell growth with dye, product safety concern

Glycosylation (macro-heterogeneity)	NIR spectroscopy [106]	In-line	9	Exponential growth and death	PLSR, LWR	VCD: 5.5 @ 90 × 10^5 cells/ mL, mAb: 45 @ 250 mg/L, NG-mAb: 11@ 80 mg/L	Capable to handles strong nonlinearity (LWR), considering the nature of the culture medium (cell death phase)	The model is strongly influenced by changes in mAb properties (NG-mAb ratio)
	Raman Spectroscopy [111]	In-line	9.8		PLSR	Real-time, T-IgG: 17.9 @ 0–380 mg/L, NG-IgG: 5.7 @ 0–98 mg/L	Capture sudden variations	Low SNR, fluorescence inference, limited sensitivity
Glycosylation (macro- and micro-heterogeneity)	NIR [107]	Online		Lag, exponential, stable, and death	LWR, SVR	Real-time, mAb >30 mg/L, sialylated and high mannose glycoforms > 15 mg/L, accurate and stable estimations of mAb (0-240 mg/L), NG-mAb (0-75 mg/L), high mannose, fucosylated, galactosylated and sialylated isoforms	Handle non-linear relationships between gf and spectra, calibration considering the dynamic nature of cell culture processes	Lesser extension for the galactosylated glycoform fraction profile, multiplicative effect (offset of spectra), and a likely wavelength-dependent effect observed in spectra of stationary and cell death phases, unable to differentiate sugar moieties

	HPLC-UV-MS [131] or other MS methods	At-line				LOQ: 6.1 ng/mL Resolution: 80 Da	Intact mAb, relative as well as absolute quantification of protein species based on UV-HPLC and MS detection.	Costly IP-RP-HPLC-UV-MS system, manual multistep sample preparation, not directly analyzing broth sample, complex data evaluation

PLSR: Partial least squares regressions; RT-JITL: Real-time Just-in-time learning; OPLS: Orthogonal Partial least squares regressions; MCR: Multivariate curve resolution; MAM: Multi-Attribute Method; PCA: Principal component analysis; LWR: locally weighted regression; SVR: Support Vector Regression; LOQ: limit of quantification.

LC: light chain; HC: heavy chain; NGHC: non-glycosylated heavy chain;

NG-mAb: Non-glycosylated mAb; G-mAb: Glycosylated mAb; F-gf: Glycoforms containing Fucose; G-gf: Glycoforms containing galactose; S-gf: Glycoforms containing sialic acid; HM-gf: Glycoforms of high mannose structures

CBC: case-by-case

A2: GlcNAc2Man3GlcNAc2; FA1: GlcNAcMan3GlcNAc2Fuc; FA2: GlcNAc2Man3GlcNAc2Fuc; FA2G1: GalGlcNAc2Man3GlcNAc2Fuc; FA2G2: Gal2GlcNAc2Man3GlcNAc2Fuc; M5: Man5GlcNAc2; M6: Man6GlcNAc2; M7: Man7GlcNAc2.

Table 5 List of analytical methods used in upstream (Pre-Protein A) perfusion CHO cell culture monitoring

Attribute	Analytical methods	Mode	Specs, RMSEP @ range	Advantage	Disadvantage
VCD	Dielectric spectroscopy [142]	Online	20 minutes	Non-contact in-line measurement, in situ analysis possible	Non-image-based analysis; growth phase-dependent variations
	Raman spectroscopy [143]	Online	Real-time, VCD: 0.0098, viability: 0.0121	JITL-based generic model, viability measurement, accurate, robust, scalability, minimal data preprocessing	Susceptible to unaccounted process deviations and unknown disturbances
	MIR spectroscopy: see IgG titer				
IgG titer	Microarray-based MALDI-TOF mass spectrometry [93]	At-line	< 30 minutes, IgG 0.2 g/L	Unpurified cell supernatant, semi-quantitative determination of LC and HC, sensitivity to phosphorylated species, minimal sample preparation and short analysis times, high sample throughput, high salt tolerance, and high reproducibility	Limited resolution (500 Da @ 150 kDa) and sensitivity, cause aggregation, semi-quantitative, unable to characterize micro–heterogeneities, MALDI requires homogenous matrix-analyte spots
	Raman spectroscopy [92]	Online	Near realtime	Increased the predictive power when conditions vary, less training data set	Scale-to-scale changes, degradation under dynamic operations

	Surface plasmon resonance spectroscopy [112]	Online	Sample prep: 25 minutes, detection limit: 21 ng/mL, max IgG (amine coupling): 10 µg/mL	Simultaneous monitoring of bioactive and total mAb titer, low analyte volume, shorter assay time, label-free analysis, biosensor reusability (1000 cycles, 1 month)	Narrow dynamic analysis ranges, need dilution
	MIR [97]	In-line	100×10^6 viable cells/mL, 445-day perfusion, 10–20 s per measurement	Fast, no water interference, measure two quality attributes at one time, multifunction (measure protein concentration, aggregation, charge variants, and host cell proteins)	Expensive equipment
Aggregation	Nanofluidic system [123]	Online	IgG: 12-120 mg/L, 4% - 175% deviation compared to electrophoresis	Three size groups, small sample volume, automated continuous operation (sample preparation and monitoring), small-scale operation, steady- and transient-state IgG1 production monitoring	Delay (~5 h), incomplete online denaturation, limited separation resolution, and detection sensitivity, potential device degradation and damage

1.6 Scope of this thesis

Real-time monitoring of product titers is an essential tool for implementing quality-by-design principles and optimizing the production process in the development and production of biotherapeutics. This approach enables rapid decision-making, which ultimately leads to faster and more efficient production.

This thesis focuses on developing a novel nanofluidic system for continuous adalimumab titer measurements. Adalimumab (*a.k.a.* Humira) used to be the top-grossing biologic prior to the COVID-19 pandemic, still grossing ~20 Billion USD per year. However, the key patent is set to expire soon, prompting many companies to market comparable biosimilar products in many countries. In this new era of biosimilar or 'bio better' products, it is especially critical to have a reliable assay to monitor the product quality directly, as early as possible, and as frequently as possible, to ensure the safety and efficacy of many drugs targeting the same biological target.

A ligand-binding based analysis is used to characterize the protein titer directly in the supernatant without requiring sample purification. In this research, the analyte is adalimumab, and TNF-α was chosen as the indicator. TNF-α, conjugated with fluorophores, was utilized as a selective adalimumab binder to bind adalimumab in the unprocessed cell culture supernatant. The nanofluidic device is capable of separating the bound complex (TNF-α-Alexa488-adalimumab) from the unbound TNF- α (TNF-α-Alexa488) and selectively concentrating the bound complex. Based on the fluorescent intensity from the concentrated bound complex, an intensity *vs.* titer curve can be

generated, which was used to determine the titers of samples from filtered and unpurified CHO cell cultures continuously. Further, the binding between adalimumab and TNF-α, which is directly relevant to the exaction function of adalimumab - binds and neutralizes the inflammatory cytokine, can indicate if the product has the right biomolecular structure (*i.e.*, product integrity).

Nanofluidic analysis is a ligand-binding assay and shares characteristics with ELISA, SPR, and BLI-based techniques. However, nanofluidic probes detect in-solution binding events, making the assay development simple as functionalizing the sensor surface is not required. In addition, because nanofluidic assay does not involve surface chemistry, problems due to nonspecific adsorption of analytes and assay components are avoided, allowing direct detection in complicated sample matrices, such as unpurified supernatant. The measurements rely on a specific interaction, and in this case, only the free and active analyte is identified. If the indicator interacts with another molecule in the sample matrix, the results will be skewed; however, this is typically not the case due to the high specificity of TNF- α for adalimumab and the lack of other possible binders in CHO cell culture. This approach can be used to characterize a number of analytes if the appropriate indicators are selected.

1.7 Thesis outline

In Chapter 1, continuous biopharmaceutical processing is discussed with an emphasis on upstream processes such as the perfusion bioreactor and continuous cell clearing devices. Due to the inherent complexity of cell culture processes, upstream activities are susceptible

to multiple errors and require constant process monitoring with quick turnaround times. A review of the CQAs of therapeutic proteins revealed that biologic products typically possess complicated structures that are susceptible to the cell culture environment. The CQAs must be monitored in order to maintain product quality. The next section compares different online/in-line monitoring techniques, and at-line tools with the potential for online implementation are discussed as well. This session highlights the required characteristics of a PAT tool and advises that for online titer monitoring in process development and manufacture, instrumentation with a smaller footprint, less complicated operating methods, and little requirement for advanced data analytics must be developed. This thesis overcomes some of the limitations of existing online titer monitoring systems by developing a ligand-binding based nanofluidic system to monitor the titers as well as probe the activity of the protein products. Chapter 2 details the cleanroom fabrication of the nanofluidic device. Chapter 3 discusses ligand binding assay development and the simulated online implementation of the nanofluidic system for titer monitoring. Chapter 4 will provide a summary of the thesis's work and its merits and disadvantages in comparison to existing systems, as well as a discussion of prospective system improvement.

CHAPTER 2. DEVICE FABRICATION

The rapid development of micro/nanofabrication techniques has accelerated the development of nanofluidics, allowing the fabrication of fluidic devices with well-defined nanometer-sized geometries on diverse functional materials. Current nanofabrication techniques have demonstrated a powerful capability of fabricating nanofluidic devices on a wide range of functional materials, ranging from traditional inorganics such as silicon, glass, and quartz to organic polymers such as polydimethylsiloxane (PDMS), polymethylmethacrylate (PMMA), and others, allowing for the rapid development of nanofluidic studies and applications. Nanofluidic device fabrication differs significantly from regular nanostructure fabrication in that it requires the formation of sealed nanoscale hollow channels without collapsing and/or the connection of these key nanometer-sized components to a supportive fluidic network, typically constructed by microchannels, for system integration.

Although state-of-the-art photolithography tools in the semiconductor industry allow for minimum feature sizes as small as 3 nm, current research facilities can only provide patterns with characteristic sizes around or above 1 μm using photolithography, which is much larger than the critical dimension of nanofluidic devices. Through etching, the nanoscale scale is attained in this case in the vertical direction (depth rather than width). To create nanofluidic devices, several nanolithography techniques with lateral nanometer resolutions are employed, including electron beam lithography (EBL), focused ion beam lithography (FIB), nanoimprint lithography (NIL), interferometric lithography (IL), and

spherical lithography (SL). The EBL and FIB techniques are excellent for directly writing single or small-scale nanochannels. The other three, NIL, IL, and SL, are typically used to generate large-scale nanopore/nanochannel arrays. Because the electron beam has a significantly shorter wavelength than UV light in convectional photolithography, it can produce features as fine as 10 nm. Furthermore, EBL is ready to be combined with other standard microfabrication techniques, such as sacrificial layer releasing (SLR), to create complex micro/nanofluidic systems. However, due to its relatively high cost and slow scanning/writing speeds, EBL is not a suitable tool for the mass manufacture of nanofluidic devices. FIB can manufacture nanoscale features (sub-5 nm) directly [144] on the substrate and is compatible with other fabrication techniques. Unfortunately, because of the direct milling/deposition mode, this approach still requires expensive equipment and has a lower fabrication yield than EBL. Unlike traditional lithography, NIL physically presses preset molds into imprint resist to copy nanoscale features (10 nm) and thereby overcomes the diffraction limit. NIL is relatively inexpensive, but it is only employed in limited circumstances because the manufacture of the imprint modes necessitates the employment of more expensive nanolithography processes. IL can create features as small as 200 nm, but it can only fabricate regularly patterned structures. Another low-cost technology for patterning large-scale two-dimensional ordered nanostructure arrays, particularly nanopore arrays, is SL. While the compatibility of the assembly-based nanoparticle monolayer preparation process with traditional microfabrication remains a hurdle.

Although the nanolithography-based technologies discussed above can create diverse nanostructures, the most popular nanofabrication approaches continue to rely on regular

MEMS techniques due to their high throughput and low cost, as well as their wafer-scale processing capability. Defining structure using normal photolithography is often followed by structure development via a sequence of subtractive (etching) procedures, followed by bonding to seal the nanochannels. This is the method employed in this study to create the nanofluidic device. Figure 5 depicts the nanofluidic device diagram.

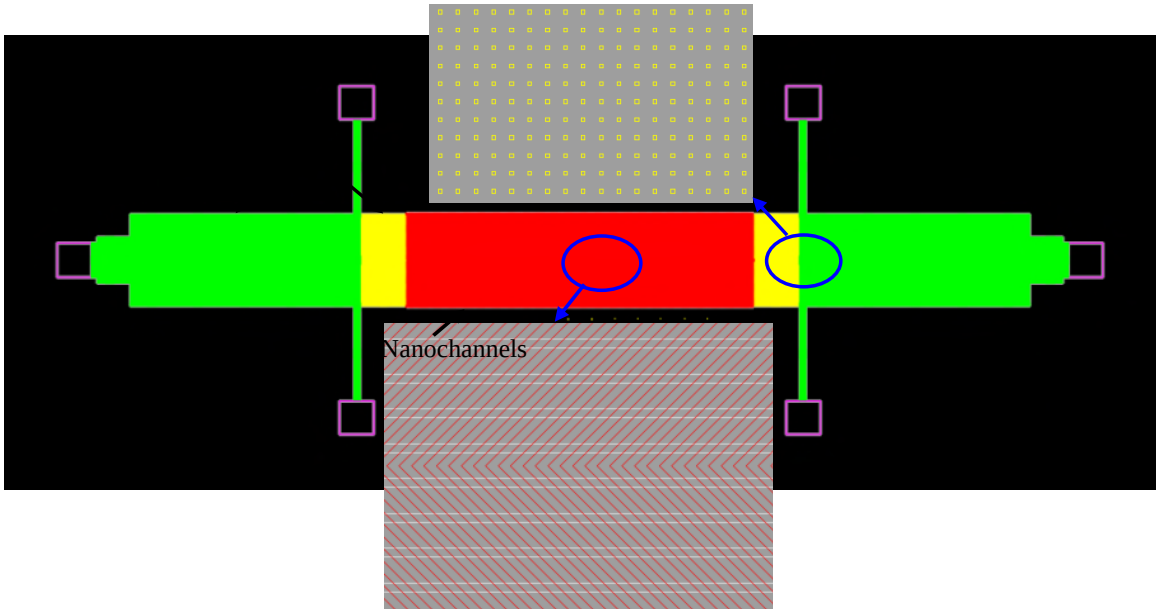

Figure 5 Design of the nanofluidic device. The red nanochannels have 1um width, 2 µm pitch; white parallel nanochannels have 3 µm width, 4 µm pitch; yellow nanochannels and green microchannels are 5 µm square pillars at 25um separation; Through-holes are 1.2 mm square holes.

2-D planar nanochannels in this thesis are created by etching nanometer-deep trenches in a substrate and then bonding it to another substrate. This method of manufacture begins with a typical photolithography stage (Heidelberg MLA 150) on a silicon (100) or fused silica substrate. The width and length of the nanochannel are defined via photolithography. The patterned photoresist is then used as a mask in the etching stage (SAMCO ICP) to generate a shallow trench on the substrate, which defines the height (10-100nm) of the

nanochannel. Following this, identical photolithography and etching are utilized to build nanochannels of varying depths, as well as microchannels that are used to introduce the liquid into the nanochannel and connect other fluidic components like tubing. DRIE (SPTSs Rapier system) or KOH etching (20 wt percent KOH solution at 80 °C) are used to create reservoirs on the silicon wafer. A 250 nm thick LPCVD low-stress nitride was used as the etching mask for KOH etching. For fabrication using fused silica wafers, the reservoirs are laser drilled. For the silicon substrate, a thick oxide layer of 500 nm was produced using thermal oxidation (Thermco 10K) on all exposed surfaces, which acts as an electrical insulation layer. Finally, after a surface activation process, this substrate is anodic-bonded (EV501, Electronic Visions) or fusion-bonded with another substrate to enclose the open channels. Finally, the bonded substrates were diced into separate devices using a die saw (Disco DAD-3240). The widths of the nanochannels were measured using scanning electron microscopy (Zeiss Sigma 300 SEM, Zeiss Gemini 450 SEM) after each pattern was etched, and the depth was evaluated using atomic force microscopy or profilometry (Veeco D3100 AFM, Asylum Research Jupiter XR AFM, Dektak-XT stylus profilometer). Ellipsometry was used to determine the thickness of the nitride layer (Semilab SE-2000 Spectroscopic Ellipsometer). The oxide layer thickness was evaluated by SEM imaging of the channel cross-sections. A cross-section view of the nanochannels was also examined by SEM after bonding to analyze the change in nanochannel depth caused by the bonding process.

Because the smallest dimension of the nanochannel is at the limit of the laser writing device (~1 μm), cross-exposure during laser writing is a significant barrier to exposing the

nanochannels with the target dimension. Two different photoresists were examined to inspect their sensitivity at different exposure conditions, *i.e.*, the laser wavelength and power. For uniform and repeatable development, auto photoresist development recipes were created. Photoresist coating and baking conditions are tuned to improve etch selectivity under various etching conditions (different substrates, photoresists, ICP RIE, DRIE). To improve etching uniformity and consistency, several gas chemistries were evaluated on a range of plasma etching devices. The wafers tend to break during long hours of KOH etching, lowering the process yield. This thesis investigated methods for increasing the yield. In terms of wafer bonding, chemical and plasma surface pretreatment methods were investigated, and their effectiveness was evaluated by extensive XPS surface characterizations in order to reliably bond channels of various aspect ratios and fabricated on different materials. Details on specific problems are addressed below.

2.1 Exposure of dense patterns at the resolution limit

For prototyping and low-volume manufacturing, scanning laser and probe-based exposure is an appealing alternative to traditional mask-based lithographic processes, as it allows for quick design modifications since no mask is required. The channels are patterned using a positive photoresist. A positive photoresist is a form of photoresist in which the exposed area of the photoresist becomes soluble in the photoresist developer. The photoresist developer cannot dissolve the unexposed region of the photoresist.

The nanochannels are 1 μm wide at 2 μm pitch (the distance between channels is 1 μm). In such close spatial proximity, writing structures generate fabrication artifacts as

polymerization appears to depend on the local photochemical environment and the intensity distribution further away from the desired focal spots, as shown in Figure 6. As the scan paths get closer, the laser beam profile overlaps, broadening the region where the power is above the polymer reaction threshold of the photoresist and creating “crosstalk” between exposed spots (proximity effects). A typical image of the channels exposed and developed is shown in Figure 7 (a), in which the tested pitches are 4 μm, 6 μm, and 8 μm. This crosstalk/bleeding creates features much larger than the design, especially as the pitch reduces. Reducing the pitch of structures to 2 μm with this photoresist (AZ3312) is impossible, even under proper baking and exposure conditions. At 1 μm feature size, the variation of the width of the exposed area is significant in the direction perpendicular to the wiring direction of the laser head, as shown in Figure 7 (b), and writing channels with uniform width proves to be challenging with this photoresist.

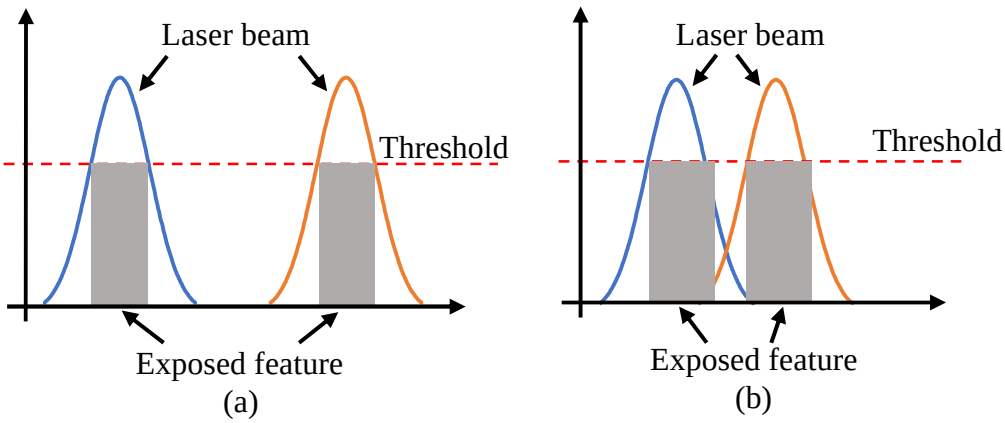

Figure 6 Cross-talk between adjacent features during laser writing. (a) Features further away from each other; (b) Features close to each other, proximity effect.

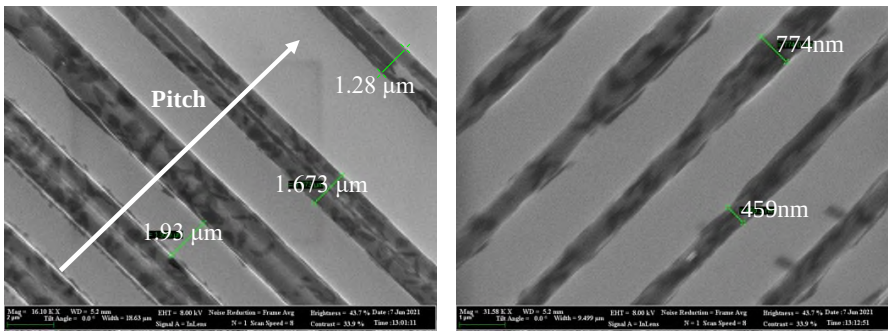

(a) (b)

Figure 7 Images of the channel exposed on photoresist AZ3312. (a) Broadening due to cross-talk; (b) Nonuniform width due to stitching in direction not along the wring direction of the laser head.

A new photoresist, SPR955, was chosen to circumvent the cross-talk issue. This photoresist is known to produce dense lines and spaces, and it can be coated at a smaller thickness, which also contributes to an improvement in contrast, since a thinner resist layer shows less dark erosion (erosion of the unexposed resist) and thus better resolution. Softbake is employed to lower the residual solvent concentration, which can further reduce dark erosion. The theoretical resolution limit is proportional to the square root of the wavelengths, so the difference between 405 nm and 375 nm is less than 5% resolution gain. But the exposure time using the 375 nm wavelength can be twice as long. An optimized exposure dose is another requirement for attaining the maximum resolution of a given resist. An important requirement to attain the maximum resolution of photoresist patterning is a maximized contrast. Only if the development rate of the exposed resist is sufficiently high, and the erosion rate of the unexposed photoresist is as low as possible (vice versa in the case of negative photoresists), the total dark erosion after development will not deteriorate the smallest features. If the exposure dose is too low, the development time increases, which increases total dark erosion. Too high exposure doses cause an undesired

exposure by scattering, diffraction, and reflection of the part of the photoresist that should not be exposed, making it soluble in the developer. The optimum exposure dose and the focus are determined with an exposure series test.

Although this SPR955 photoresist is thinner (700 nm), it is not as UV-sensitive as AZ3312. Therefore, a higher dose was required to properly expose the features in the photoresist. This relative insensitivity could also contribute to the significant reduction in terms of the cross-talk issues present in the AZ3312 photoresist. The exposure threshold of SPR955 is much higher than the combined exposure of the two adjacent lines, therefore, the bleeding did not alter the defined line exposure as in AZ3312. The dose and focus test should be performed periodically to capture any possible machine performance shift (Figure 8 (a) and (b)). The dose and focus used in Figure 8 (a) were from the dose and focus test performed a month prior to exposure, and the machine conduction shifting resulted in overexposure. After retesting the machine using the does and focus matrix, the exposure conditions were optimized again, and the new exposure using the updated conditions is shown in Figure 8 (b).

The first layer of the device is about 85 nm deep, which means the photoresist in the etch region, where the first layer is patterned, is thicker than the rest of the area of the wafer. As the SPR955 photoresist is relatively thin (about 700 nm), the thickness difference due to the existence of the patterned trenches is significant. Therefore, the optimal dose and focus combination for the patterned region differs from the rest. An increase in dose and defocus should be expected in this case (Figure 8 (c)-(e)). It is clear in Figure 8 (e), the channels are properly exposed in the area that is not pre-exposed, while in the area where the first

layer was patterned, the photoresist was underexposed, *i.e.*, the width of the channel is narrower than the design. A systematic issue with the MLA150 is uneven exposure, which could be caused by the stage-laser misalignment (Figure 8 (f)). Post-exposure baking and developing are programmed on the pTrack control software after the developing time was optimized in a manual development setup. The channels exposed with SPR955 photoresist are shown in Figure 9, and the variation of the channel width was reduced from 40% to 8% for 1 μm wide features. With proper baking conditions, this photoresist can withstand 300 nm Si etching (RIE, SAMCO ICP) with a selectivity of around 1.76:1. The same photoresist was also used to pattern nanochannels on fused silica wafers, as shown in Figure 9 (d).

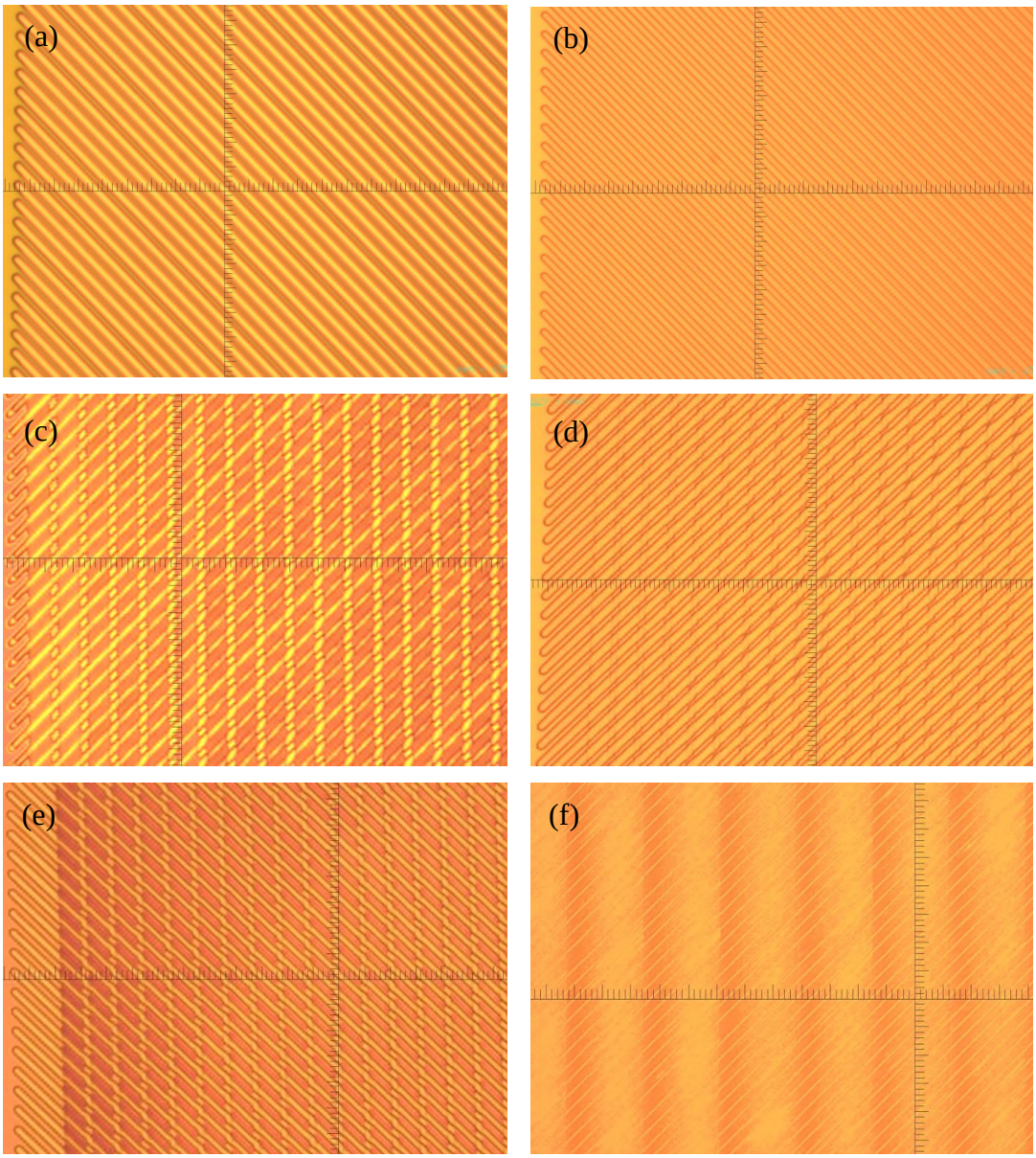

Figure 8 Exposure of SPR955 photoresist using MLA150. (a) First-layer exposure, overexposed due to machine performance shift; (b) First-layer exposure, properly exposed based on updated dose and exposure matrix tests; (c) Second-layer exposure, underexposed on the unexposed region and on the region with the first layer patterned; (d) Second-layer exposure, overexposed on the unexposed region and on the region with the first layer patterned; (e) Second-layer exposure, overexposed on the unexposed region and a little overexposed on the region with the first layer patterned; (f) Uneven exposure, a systematic issue with MLA150.

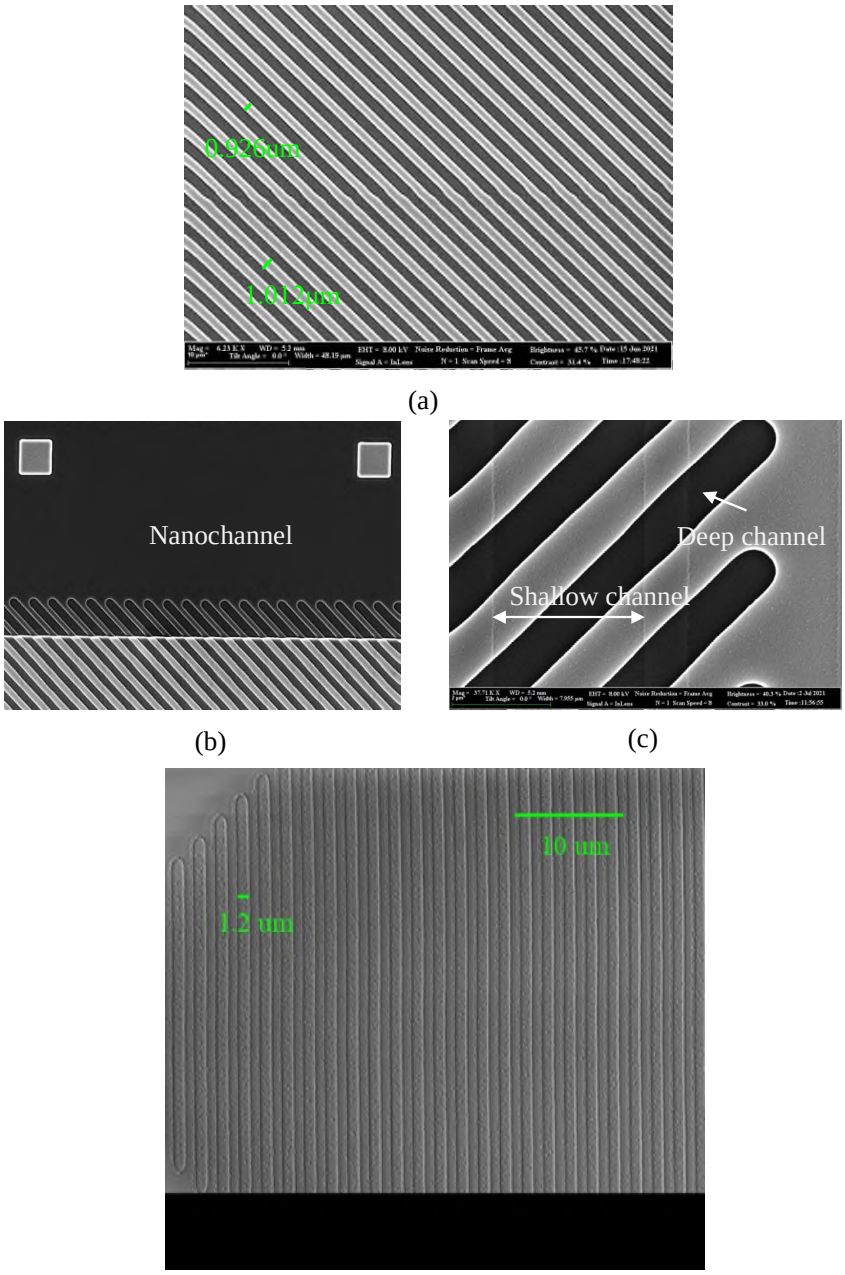

Figure 9 Nanochannel under SEM after RIE etching, patterned using SPR955 photoresist with MLA150. (a)-(c) are the features on the Si substrate. (a) 1 µm wide nanochannels; (b) Herringbone nanochannels and the transition nanochannels; (c) Nanochannel region showing the first layer shallow channel and the second layer deep channel; (d) First layer nanochannel on fused silicate substrate.

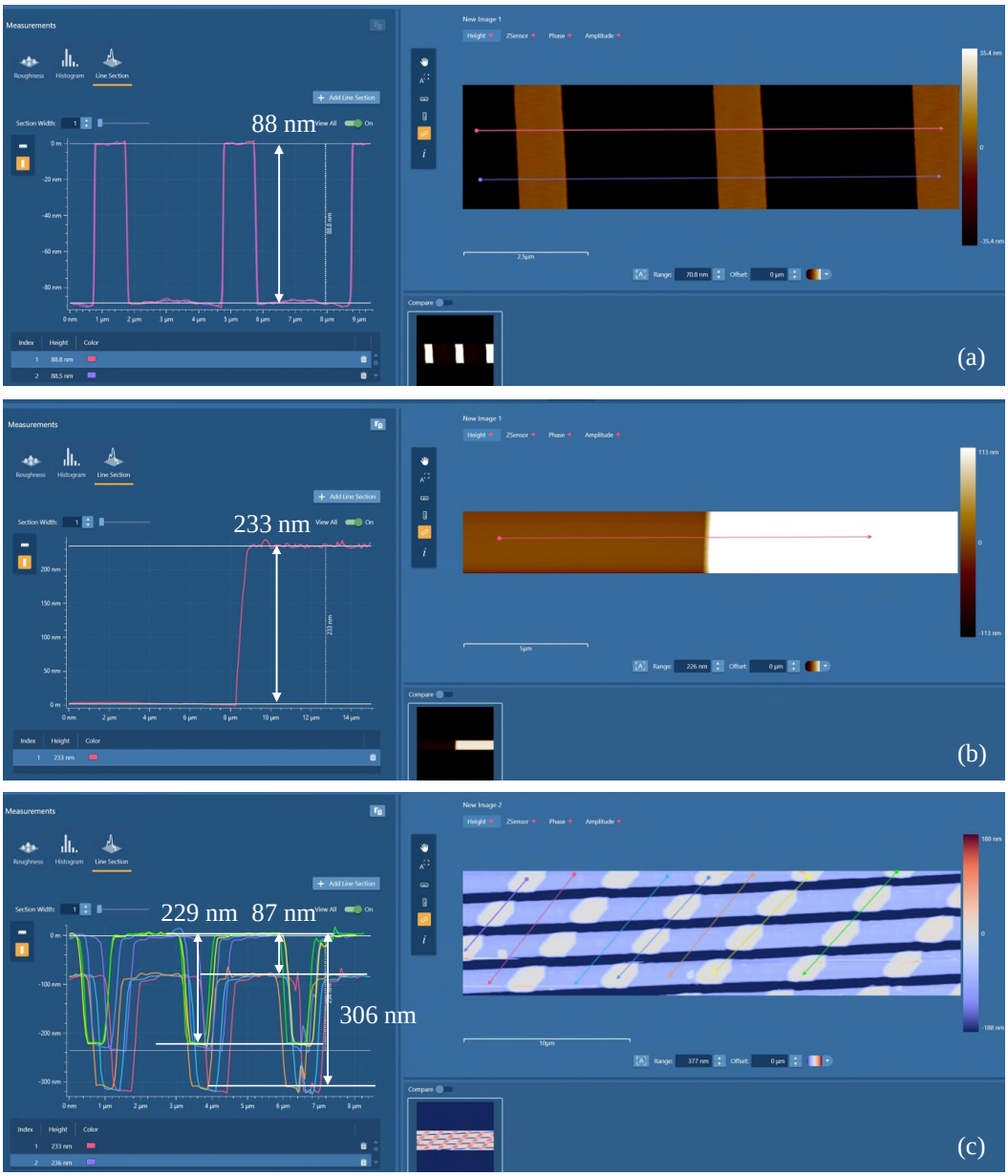

Figure 10 (a) Channel depth of the first layer (shallow channel) as measured by AFM. (b) Channel depth of the second layer as measured by AFM. (c) Channel depths measurement of 2-layer channels. The deep channel is the combined thickness.

2.2 Yield improvements

Wet anisotropic etching is the main process of silicon bulk micromachining for the fabrication of different types of microstructures (*e.g.*, cantilever, diaphragm, cavity, etc.). 67

Potassium hydroxide (KOH) and tetramethylammonium hydroxide (TMAH) are the two main etchants used for wet anisotropic silicon bulk etching. These etchants are thoroughly investigated under various etching conditions. KOH is preferred over TMAH to achieve high etch selectivity between the {111} and {110}/{100} planes. The process most often takes advantage of the etching ratio between the crystal planes in the silicon lattice. The sidewalls of the etch are defined by the <111> plane, and the <100> plane is etched at 54.7° relative to the <111> plane. An etchant with a high etch rate may also provide high etch selectivity between the silicon and mask layer, which is very useful for using the same thickness mask layer for prolonged etching. The important parameters that affect the etch rate and surface morphology are etchant concentration, etching temperature, ultrasonication/microwave irradiation during etching, and the addition of different kinds of additives to the etchant. Each method has its benefits and drawbacks. Maximum etch rate of Si{100} and Si{110} is obtained in KOH with a concentration range from 15 to 25 wt%. Due to the nature of this etch, careful thought must be given when designing the feature, as well as ensuring proper alignment during lithography. Here, 20% KOH solution at 80 °C was used to etch through the Si substrate; the Si etch rate was about 1.33 μm/min, and the low-stress SiN selectivity was 33000:1.

A 200 nm thick silicon nitride film was deposited (LPCVD, VTR low-stress SiN deposition) on the Si wafer for a hard mask upon KOH etching after RCA cleaning of the surface. The nitride layer thickness was measured using a spectroscopic ellipsometer (Semilab SE2000, the refractive index of the VTR nitride is 2.25), and the thickness is around 230 nm. Hexamethyldisilazane (HMDS) was vapor primed on the silicon nitride

film as an adhesion promoter using the YES oven (Yield Engineering Systems), followed by spin-coating the positive photoresist AZ10XT-520 cp (MicroChemicals). The spin time was 40 seconds at 1800 rpm following an initial 500 rpm and 5 seconds spin [142]. No edge removal of the photoresist was performed. The photoresist film was baked at 97 °C for 30 minutes in the oven, and the thickness of the photoresist was confirmed using an ellipsometer and a Dektak-XT stylus profilometer (measured thickness was 8 μm instead of 10 μm). The photoresist was rehydrated for 30 minutes before being exposed to 405 nm UV light using MLA150 to define the patterns. The dose and focus matrix was used to optimize the exposure conditions. The exposed photoresist film was developed in AZ 435 (MicroChemicals) using pTrack with a customized recipe that involves cycles of spray, stream, and puddle. The developed pattern was checked under an optical microscope equipped with a color filter. The wafer was then baked in the oven at 97 °C for 30 minutes before RIE etching of SiN using SAMCO F (60 nm/min). Jupiter XR was used to measure SiN etch depth. The photoresist was stripped using Piranha, and the wafers with exposed Si loading holes were etched in KOH. Hot phosphoric acid was used to etch away VTR SiN (4 nm/min, 90 minutes total).

Wafer yield though this above single side-KOH etching was low (20%) as the Si wafer became brittle after 11-hour KOH etch. One way to improve on this process is by patterning both sides of the SiN, which allows KOH to etch both sides of the Si substrate. To do that, both sides of the wafer were coated with AZ10XT photoresist using the procedure as follows: the front side was coated with 10 μm resist and baked at 97 °C for 15 minutes in the oven, then the back was coated, and baked for another 30 minutes at 97 °C in the oven.

Following a 30-minute rehydration, the front side and the back side of the wafer were exposed using MLA150 (front side 300 mJ/cm^2 dose, 0 defocus, backside 400 mJ/cm^2). The wafer was loaded on a 25-wafer cassette and developed manually using AZ435 developer (one wafer at a time). The developer bath was agitated manually in a non-repetitive pattern as the development was diffusion rate limited. After developing, the wafer was rinsed with DI for at least 2 minutes and dried with a nitrogen blower. Following a 30-minute hardbake, the wafer was etched using SAMCO F (a quartz handling plate was used to prevent possible contamination of the chuck as the photoresist might leave residues due to the wafer heating up during etching). The yield using this method was about 80%, and the loading holes can be designed smaller as well (1.4 mm squares *vs.* 2 mm squares for single-side KOH etched wafers).

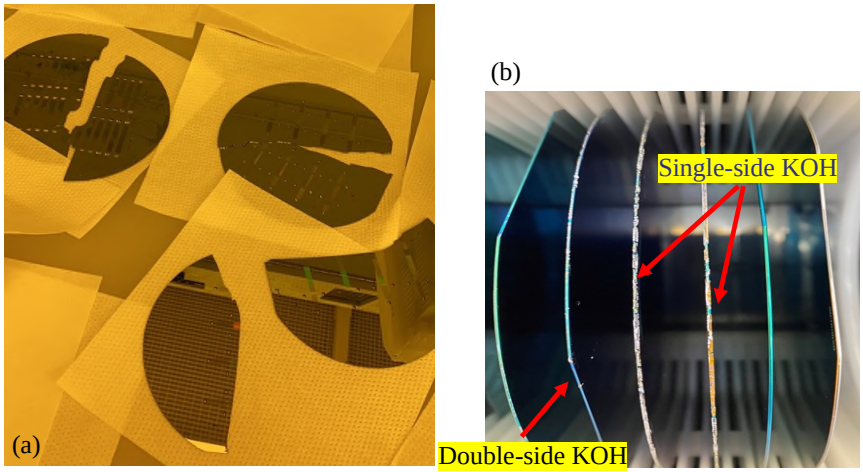

Figure 11 Loading hole etching using KOH (a) single side patterned; (b) double side patterned.

High-aspect-ratio (defined as the ratio of width to depth) structures fabricated from silicon can be achieved by deep reactive-ion etching, most commonly the Bosch process [146].

This method was explored as an alternative to KOH etching of the loading holes. A 20 μm thick photoresist was employed as the etching mask. A 10 μm AZ10XT 520 cp photoresist was coated first, followed by a 30-minute partial soft bake in a 95 °C oven. And another 10 μm of AZ10XT 520 cp was coated, and the wafer was baked for 60 minutes in the 95 °C oven. Sufficient baking is critical so the photoresist can withstand long DRIE etching. The actual thickness of the photoresist is about 16 μm, as shown in Figure 12. After a rehydration hold of 60 minutes, the photoresist was patterned. Dose and focus tests were performed to ensure the resist was thoroughly exposed (700 mJ/cm^2 dose, 0 defocus was used to pattern the halo holes). Manual photoresist development was performed by immersing the wafer in the AZ435 developer solution. The solution needs to be agitated in a non-repetitive pattern to prevent the pink "cloud" of saturated developer from forming above the sample and slowing the developing process (no agitation will cause streaks after baking). A recipe was developed on the Ptrack as well to perform auto-developing, which involves multiple cycles of spray-stream-hold, with a thorough rinse at the end of the process. The developing results were checked thoroughly before post-baking. This step is of critical importance for thicker photoresists as the exposure and development can easily be insufficient, especially in areas not readily accessible, *e.g.*, the corner of the halo hole (Figure 13 (a)). Further, the exposure using MLA150 seems to be uneven, as shown in Figure 13 (b), with residual lines of the photoresist indicating that these areas were underexposed, but the rest of the area was properly exposed. This uneven exposure contributes to the variation of the line width when writing the patterns on the thin photoresist. Particles typically originate from the photoresist coating step, which should be

minimized because it can interfere with patterning or development. Even if they are located in the area without patterns in the current layer, they will reduce the adhesion of the photoresist, leading to photoresist damage and failure to protect the patterns beneath from previous layers during DRIE etching.

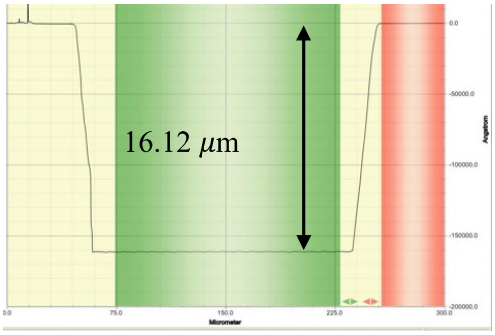

Figure 12 Fully developed halo hole pattern. The actual thickness of the photoresist is 16.12 μm instead of 20 μm.

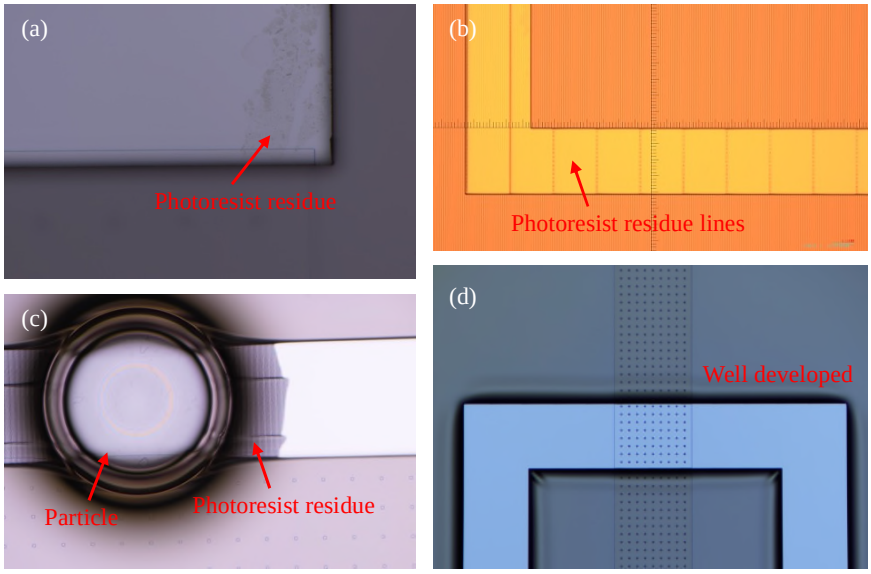

Figure 13 The halo hole features patterned on 20 μm photoresist after developing. (a) Photoresist residual at the corner of the halo square, suggesting under develop; (b) Photoresist residual lines, possibly caused by the uneven exposure of MLA150, exposure dose should be increased; (c) Particles cause selective area being underdeveloped, particle might be originated from developing process or photoresist coating; (d) Well developed wafer with proper exposure dose and focus.

During DRIE, the vertically focused ion bombardment of conventional reactive-ion etching is periodically interrupted by passivation periods, which coat the sidewalls and trench bottom with a thin coating of polymer. The trench bottom polymer is preferentially destroyed during etching, followed by a brief isotropic silicon etch. In order to minimize over-etching of more open features, masks are often patterned as halo geometries, with all etching occurring in constant-width trenches. The DRIE parameters were chosen to give initial near-vertical sidewalls. The aspect ratio of the etched features has been observed to influence the vertical etching rate. Etch 'lag' is most noticeable in narrower etched sections, which do not etch as quickly as more open structures. This has important consequences for the etching of high aspect ratio features, for which the energy flux to the bottom of the etching trench decreases with increasing aspect ratio. For good-quality DRIE, etching and passivation should remain in balance at the sidewalls throughout the etch, although etching should dominate at the trench floor. For the sidewalls, if etching dominates, the sidewall polymer will be removed, allowing subsequent silicon etching with the slow erosion of the initial scalloping. If passivation dominates, the polymer layer will thicken with time, becoming thickest toward the top of the sidewall. Sidewall quality and profile are highly dependent on the width of the etched channel. When etching through 525 μm thick silicon (100) wafers, if the width of the trench is greater than 100 μm, over-passivation of the sidewalls was observed, with a region of thick polymer build-up followed by vertical striations and a very rough surface, but with an overall vertical profile [147]. Channels narrower than 100 μm, in contrast, generally show good sidewall smoothness, though with

a bowed profile. This profile leads to ion-induced damage towards the bottom of the channel sidewall [147].

For through-hole etching, the wafer must be mounted on a carrier wafer. Adding a carrier wafer prevents helium from escaping into the plasma chamber once the wafer has been engraved. During etching, the device wafer (the wafer being etched) is subjected to a heat flux caused by the plasma within the chamber. The heat flux constitutes a significant portion of the RF power supplied to the chamber. During etching, the temperature of the device wafer increases until the heat transfer to the chuck equals the heat input from the plasma. As a result of low gas pressure, mounting on a standard planar carrier wafer impedes the efficient passage of heat from the wafer to the chuck electrode. The excessive and unpredictable temperature has a significant impact on photoresist degradation and process selectivity. Variability in the heat input to the wafer and insufficiency of the cooling procedures make it difficult to provide reliable temperature and etching uniformity control over wafers. Even when the chuck electrode is independently cooled, the wafer temperature can easily reach 100 ° C or more over that of the chuck electrode, making it extremely difficult to provide effective temperature control via the chuck electrode temperature. In this thesis, the chuck temperature is set to 0 ° C, which nonetheless causes the photoresist to burn during through-hole etching.

In this study, a grooved carrier wafer (design credited to Jorg Scholvin, MIT.nano) is employed to facilitate cooling during DRIE etching. The groove pattern was exposed on 10 μm AZ 10XT 520 cP photoresist (actual thickness is 8 μm) utilizing a 4-cycle constant time interval regime with 5 seconds exposure time and 5 seconds delay time on a Karl Suss

MA-6 mask aligner. The groove pattern was etched by DRIE using the recipe in Figure A 3 (all etching recipes can be found in the Appendices). With this recipe, 157-170 etching loops were used to achieve a depth of 100-126 μm (Figure 14 (c)). The grooved carrier wafer is illustrated in Figure 14 (b), with grooves shown in Figure 14 (d). The carrier wafer is coated with 1 μm of PECVD oxide to protect the Si during DRIE. To mount the device wafer on the carrier wafer, the back of the device wafer is coated with a photoresist, and the carrier wafer is mounted to the device wafer by applying gentle pressure, followed by 30 minutes of baking at 95 °C. The gaps generated between the grooves and the device wafer are crucial for removing heat during DRIE etching. During the DRIE process, the cooling helium will fill these gaps and provide a thermal channel to evenly cool the surface, and during the vacuum pumpdown, the trapped gas will be evacuated. After etching four to five device wafers, the carrier wafer must be replaced as it begins to wear down; continued usage of a worn carrier wafer (the edge is much thinner) will result in photoresist burn, as illustrated in Figure 14 (e).

In this thesis, a channel width of 100 μm was chosen for the halo hole. The final sidewall was almost vertical, as demonstrated in Figure 15 (a), showing an overall balance between the etching and passivating stages. The sidewall near the front side of the wafer loses the scalloping (Figure 15 (b)), which can be seen as a result of over-etching, while near the back of the wafer, a scalloped look can be clearly seen in Figure 15 (c). As the aspect ratio of the trench changes during etching, it is impractical to assume a single set of process parameters to maximize the balance between sidewall passivation and etching for a through-wafer etch. Additional DRIE recipe optimization may involve parameter ramping

to promote sidewall quality. Complete polymer removal is essential for future thermal oxide layer growth. Following the removal of the photoresist with Piranha, the wafer was ashed with O_2 plasma for 20 minutes before being cleaned with Piranha. Using DRIE to create through holes often yields a 100% success rate if the burnt photoresist issue is totally avoided. This process is quite complicated, as it requires the preparation of carrier wafers and the replacement of carrier wafers on a regular basis. Further, it utilizes a substantial amount of chemicals to remove the passivation polymer. The DRIE process has a low throughput since only one wafer can be etched at a time, and the DRIE etching per se takes between 1.5 and 2 hours. The rough edge caused by the DRIE etching is the prime location for electrical breakdown. Comparatively, a double-sided KOH bath can etch 25 wafers in around 6 hours per batch, and the hot phosphoric acid used to remove the nitride mask can be reused. However, the LPCVD low-stress nitride mask is required for KOH etching, which adds complexity to the process.

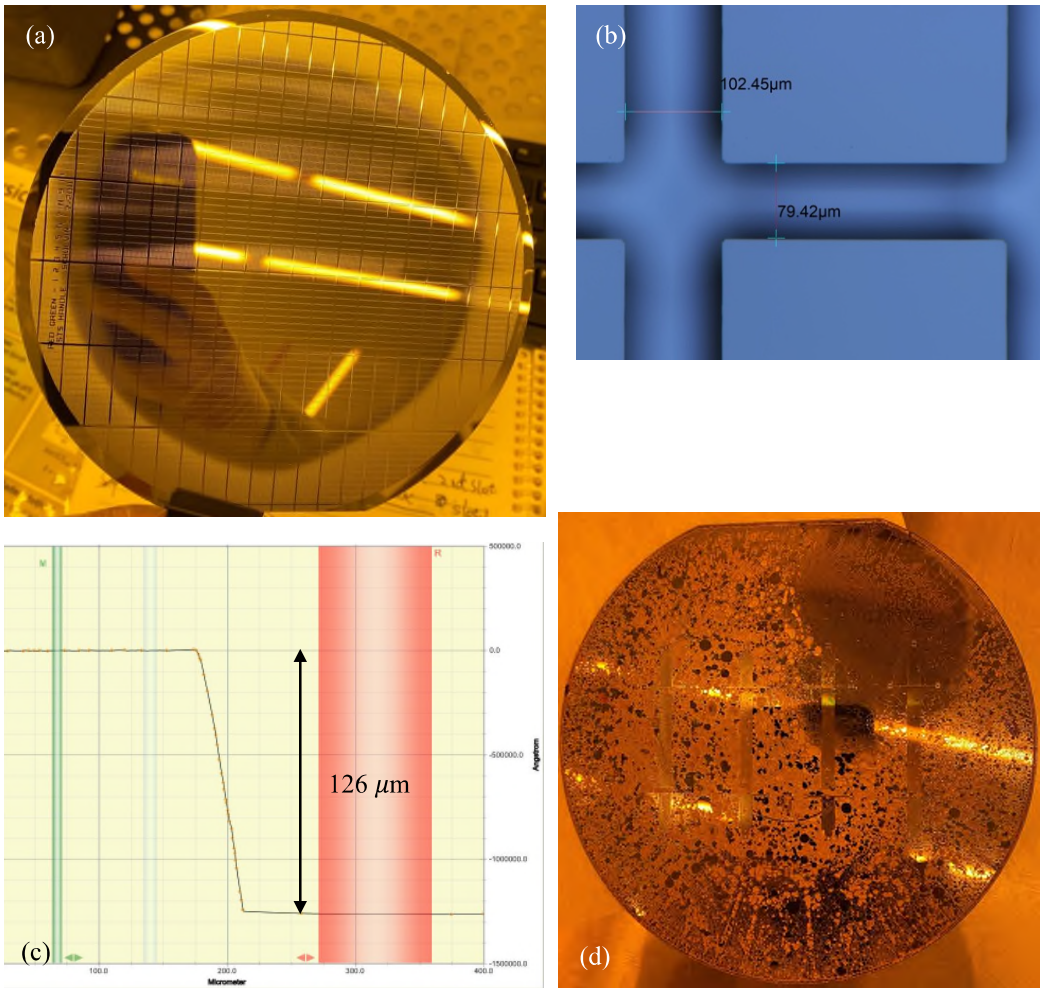

Figure 14 (a) Grooved carrier wafer. (b) Groove height measured by a stylus profilometer, 170-loop DRIE etching. (c) Dimension of the groove. (d) Burnt photoresist during DRIE etching due to carrier wafer wear.

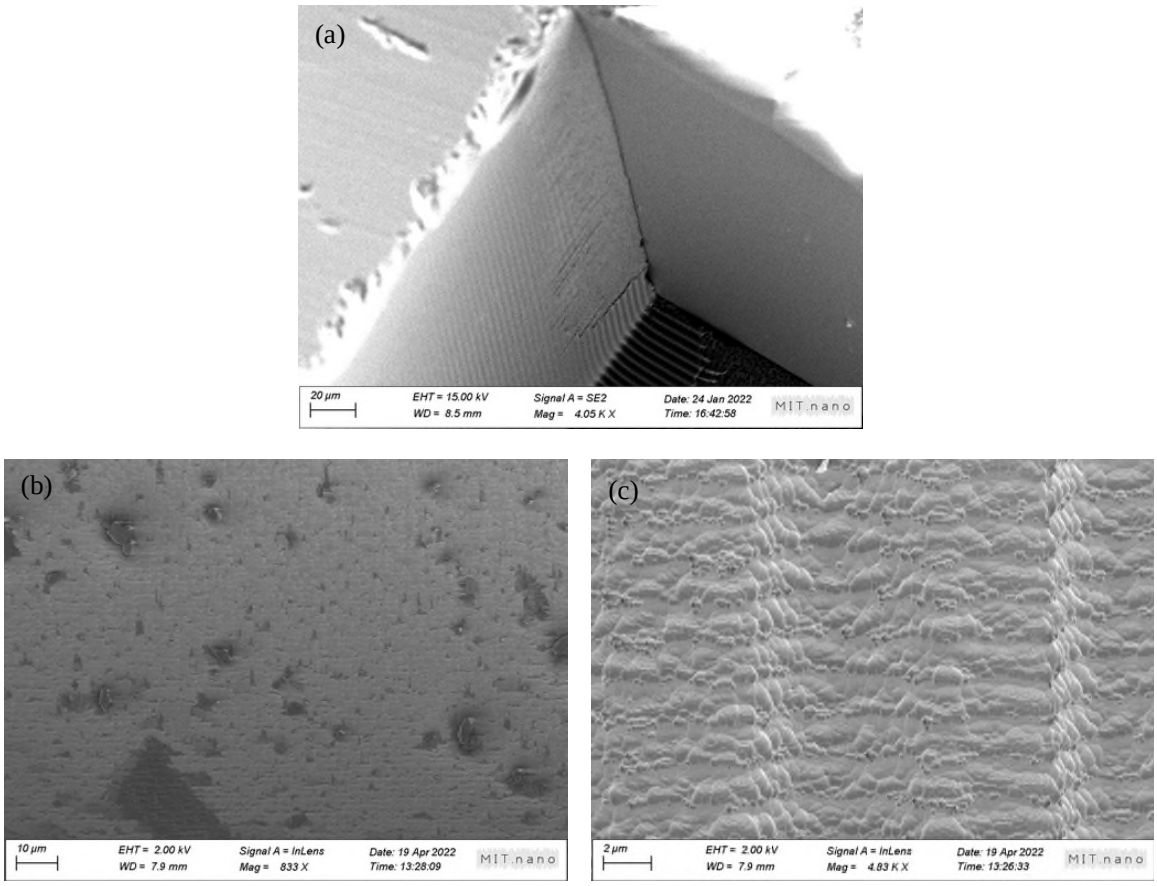

Figure 15 (a) Through hole on the 650 µm thick wafer etched using the halo mask pattern. (b) Sidewall of the through-hole near the front side of the wafer. (c) Sidewall of the through-hole near the back side of the wafer with clearly visible scalloping.

2.3 Wafer bonding

Wafer bonding is required to close the open channels. Since a thermal oxide layer of 500 nm was grown on the silicon wafer, the bonding between the silicon wafer and the borosilicate glass wafer was essentially a bond between oxides. Anodic bonding is usually used to bond a silicon wafer to an alkali ion-containing borosilicate glass substrate. This is a field-assisted bonding or electrostatic bonding process that joins ion conductive materials to silicon through a sufficiently strong electrical field. It is a well-established technology

used in the semiconductor industry for microsensor fabrication and MEMS packaging. The schematic process of silicon–silicon anodic bonding is shown in Figure 16. The wafer and glass substrates are placed between two metal electrodes and heated to 400 °C [145], which needs to be sufficiently high to render the non-conductive material electrically conducting. In a silicon–glass anodic bonding pair, the silicon side and the glass side are biased as the anode and the cathode, respectively, and a DC potential of up to 1 kV is applied. When the sandwiched anode-silicon-glass-cathode structure is subjected to a strong electrostatic field, the mobile alkali ions in the glass are drifted away from the bonding interface, leaving a depletion region of a few micrometers thick. The charges left in the glass create a large electric field, which pulls the wafer surfaces into contact. The oxygen ion left behind will form a strong covalent silicon dioxide (SiO_2) bond with silicon atoms.

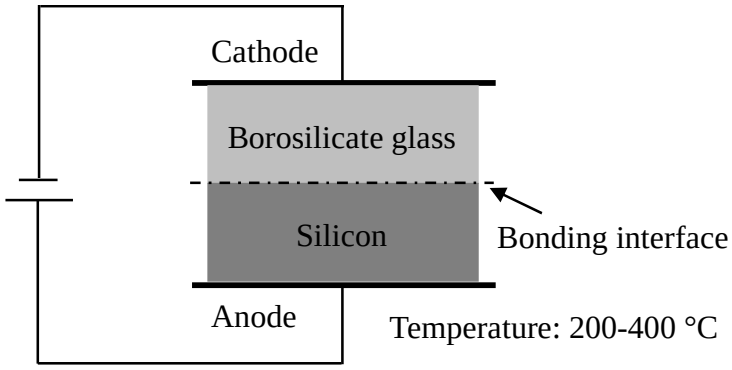

Figure 16 Schematic view of silicon- borosilicate glass anodic bonding.

However, the large pulling force causes the channels to collapse when the aspect ratio (depth to width ratio) of the channels is small, as shown in Figure 18 (a). In this process, the bonding was performed at ambient pressure with a temperature of 350 °C and a voltage of 900-1000 V applied at once. Ramping up to the bonding temperature generally takes 30

minutes. After the current dropped to around 0 mA, the heat was turned off, and the sample was cooled down to around room temperature. One possibility to avoid the channel collapse is to ramp up the voltage in a few steps to the maximum value, which can gradually draw the sodium ions away from the interface and lower the electrostatic force. Figure 17 shows the parameters for a process performed at a higher voltage (750 V) with the voltage ramping in five steps: 400 V, 500 V, 600 V, 700 V, and finally 750 V. It can be observed that the highest current peak was reached when the 700 V voltage was applied. The other voltage ramping steps produced only low current peaks. The cross-section of the channel was examined under SEM, showing that the channels were not collapsed after the bonding, as illustrated in Figure 18. The bond quality is excellent, and no voids were generated during dicing. A qualitative bond strength test was performed as well by inserting a blade at the Si-borosilicate glass interfaces. For both interfaces, the test resulted in wafer edge breakage, showing very high bond strength. Further, anodic bonding is not strongly dependent on the surface smoothness and ultraclean environment thanks to the large pulling forces, which can be used to bond wafers with large bows. Some of the borosilicate glass wafers used in this thesis featured a large wafer bow of 86 μm as measured by KLA-Tencor FLX, making it impossible to bond with silicon wafers (the bow of silicon wafers was around 10 μm regardless of how the through-holes were processed) using thermal bonding as discussed below. Wafers of large bow, as mentioned above, can be reliably bonded using anodic bonding with the voltage ramping scheme, as shown in Figure 21, whereas fusion bonding failed to bond (Figure 20).

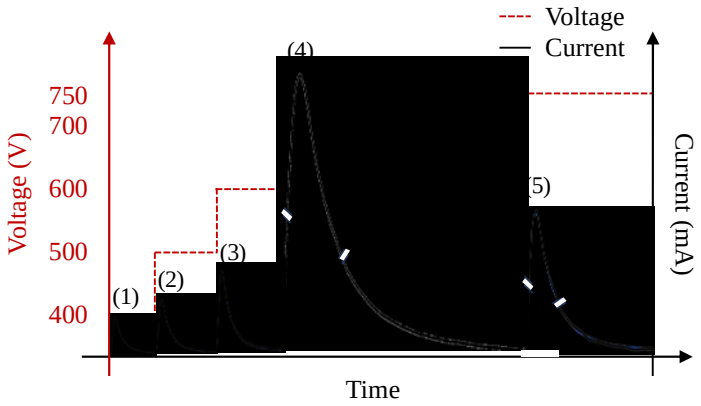

Peak current (1) 0.98 mA, (2) 1.07 mA, (3)1.4 mA, (4) 11 mA , (5) 5.7 mA.

Figure 17 Voltage ramping scheme during anodic bonding, which can prevent channel collapsing.

Anodic bonding is limited to joining ion conductive materials as sufficient amounts of mobile charge carriers are required, which makes it incompatible with bonding between fused silica wafers. Fusion bonding was explored to bond fused silica substrate pairs as well as borosilicate glass and silicon substrate pairs. When two materials with clean and flat surfaces come into close contact, it is known that the two materials will attach and establish bonds across the interface without the need for an intermediary layer. Van der Waals interactions or hydrogen bridge bonds are used to hold two mating surfaces together [149]. Because the strength of such adhesion is significantly lower than that of a covalent bond, high-temperature annealing is typically used to improve wafer bonding after the room-temperature pre-bond stage. Good bond strength in silicon-to-silicon direct hydrophilic bonding can only be attained with a high-temperature anneal at temperatures over 800 °C [150]. Bonding energy, surface cleanliness, roughness, and flatness are all critical criteria in the process flow to enable adequate wafer bonding. To begin the fusion bonding process, a physical force is applied to one place (typically at the center) on the

wafer, allowing the bond front to propagate. The propagation of the bond front to a sealed interface is determined by the balance between surface energy dissipation required to establish the bond and strain energy required to bend the wafers [151]. Second, a clean surface is essential in wafer bonding procedures. Furthermore, it is critical to guarantee that the cleaning process will not result in extreme surface roughening. Two hydrogen peroxide-based cleaning stages, RCA1 (NH_4OH: H_2O_2: H_2O = 1: 1: 5) and RCA2 (HCl: H_2O_2: H_2O = 1: 1: 6), are typically employed for RCA cleaning. RCA1 is meant to remove organic pollutants, particularly hydrocarbons, by oxidizing H_2O_2 and solvating NH_4OH. RCA2 is designed to eliminate metallic (ionic) pollutants. It is recommended to use a low ratio of NH_4OH for surface cleaning in order to avoid surface roughening caused by ammonia in RCA1. In addition to organic and metallic contaminants, particles can act as spacers to impede intimate wafer contact and generate intrinsic gaps. During wafer bonding, an ultraclean environment is preferred since the presence of a small particle can result in a large void. Thirdly, the surface roughness of the wafer is a significant metric. It is proposed that if the root mean square (RMS) roughness is less than 1 nm, it does not impede fusion bonding at ambient temperature through hydrogen bonds [152]. Fusion bonding also takes into account the surface's flatness, which can be defined by the total thickness variation (TTV). TTV is the height difference between the top wafer's highest and lowest locations. If two wafers with different TTVs must be joined, they will be distorted into a single shape during the bonding process. If the TTV is tiny, bonding can be achieved by simply bringing two polished wafers into close contact at ambient

temperature, assuming the TTV is small. When TTV is large, the space between wafers prevents them from bonding, resulting in expansive, unbounded regions.

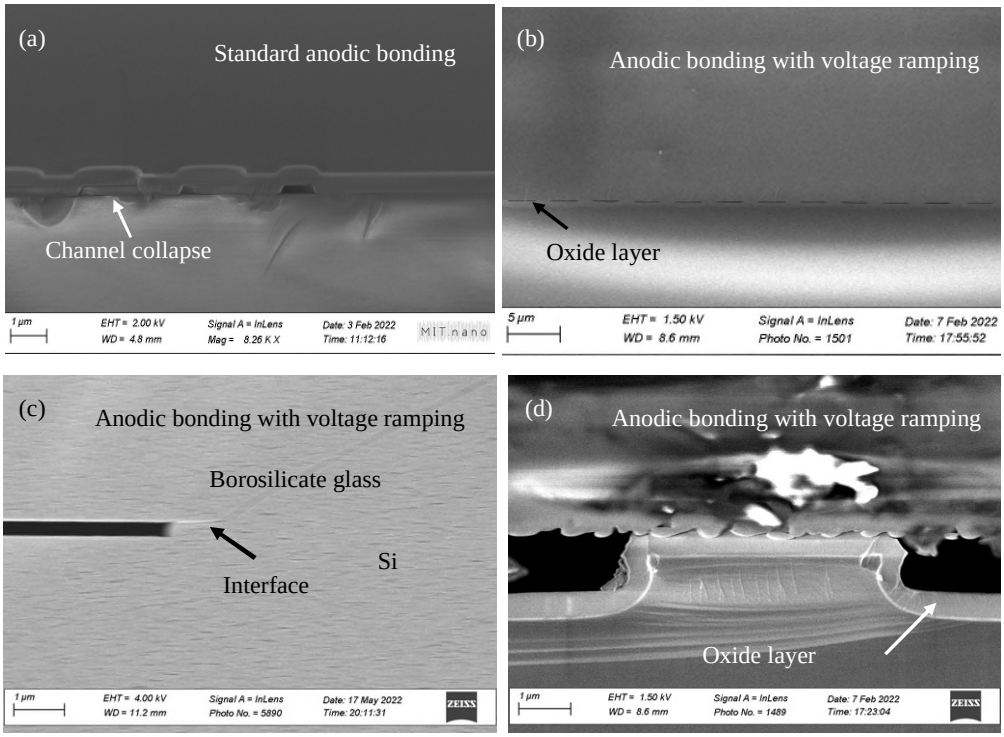

Figure 18 Bonding silicon wafer with borosilicate glass wafer using anodic bonding by (a) applying the maximum voltage at once, which leads to channel collapse; (b)-(d) voltage ramping scheme of channels that are (b) 80 nm deep and 2.65 μm wide; (c) 20 μm wide and 300 nm deep; (c) 1 μm deep and 25 μm wide.

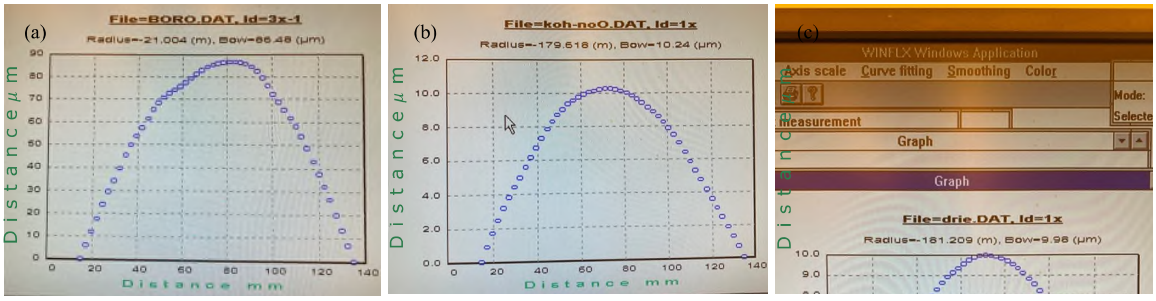

Figure 19 Wafer bow measured using a KLA-Tencor FLX optical profilometer. (a) Borosilicate glass wafer; (b) Patterned silicon wafer with through-holes made using double-side KOH etching; (c) Patterned silicon wafer with through-holes made using DRIE.

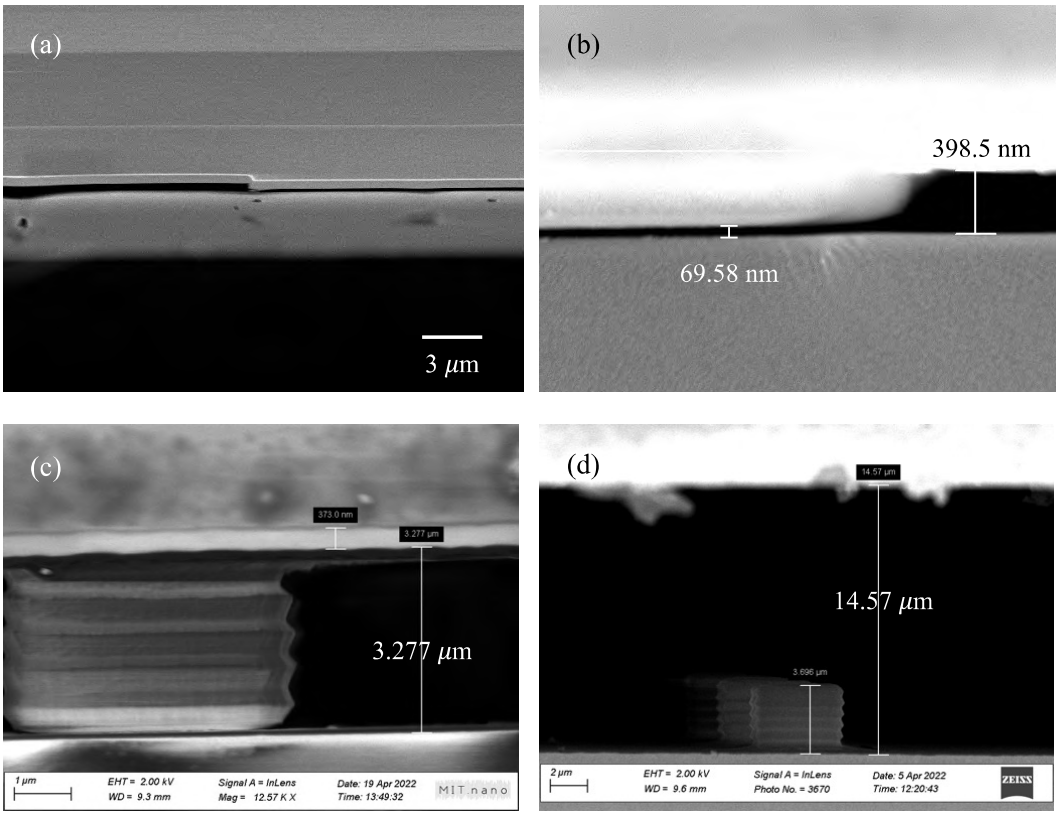

Figure 20 Fusion bonding of wafers with large bows. The borosilicate glass wafer used has a bow of 86 μm as measured by a KLA-Tencor FLX and the silicon wafer has a bow of around 10 μm. (a) and (b) Channel depth is 328 nm and the pillar failed to bond to the substrate, leaving a gap around 70 nm; (c) and (d) Channel depth is 3.277 μm, and wafer bow caused a gap of around 11 μm between the substrates.

The basic fusion bonding process involves pressing two substrates together and applying heat for an extended period of time; for instance, borosilicate glass substrates can be heated up to 600 °C and fused silica substrates can be heated up to 1000 °C, allowing the material to partially slump and fuse with the opposite substrate but without melting. Such high temperatures are undesirable for the application in this thesis when bonding shallow channels, as the channel can deform at high temperatures. Besides, when bonding two substrates with different thermal expansion coefficients, thermal stress can build up during bonding; therefore, it is necessary to design a low-temperature fusion bonding procedure.

Fortunately, the annealing temperature can be significantly reduced with wafer surface treatments.

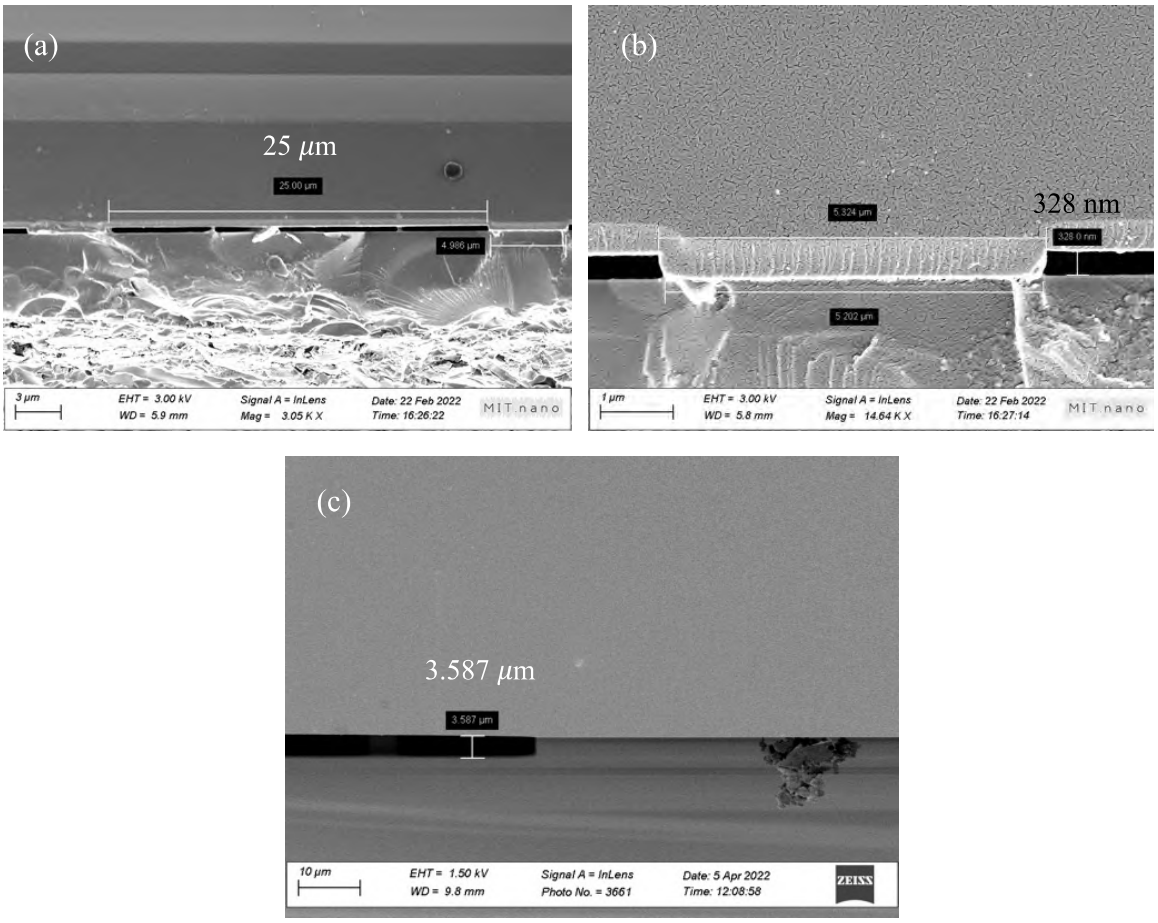

Figure 21 Anodic bonding of wafers with a large bow showed no gap between the two substrates. The borosilicate glass wafer used has a bow of 86 μm as measured by a KLA-Tencor FLX, and silicon wafer has a bow of around 10 μm. (a) and (b) Channel depth of 328 nm; (c) channel depth of 3.587 μm.

It has been found that hydrogen bonds between Si–OH groups on bonded hydrophilic surfaces will convert to Si–O–Si covalent bonds at room temperature:

$$\text{Si–OH} + \text{HO–Si} \rightarrow \text{Si–O–Si} + \text{HOH}. \quad (1)$$

The transformation of two neighboring silanol bonds into siloxanes is an exothermal process. These transformations spontaneously occur during the pre-bonding process, which is reversible at temperatures lower than 425 °C. As a result, the covalent connections will revert to Si–OH hydrogen bonding. However, if the water produced by the preceding process is totally eliminated, the covalent bonds can then remain, resulting in full covalent bonding at room temperature. Wafers can be hydrophilically activated in a number of ways. Wet activation involves dipping the wafer surfaces in chemicals. Previously, our group devised a method for bonding borosilicate glass wafers and silicon wafers by immersing the wafers in NH_4OH for 30 minutes. And the bonding pair was heated in an oven at 550 °C for 12 hours to strengthen the bond [122]. Many Si–OH groups are converted to Si–NH_2 after the NH_4OH dip following

$$Si–OH + NH_4OH \rightarrow Si–NH_2 + 2H–O–H \quad (2)$$

During low-temperature annealing (250 °C [153]), the Si–NH_2 and Si–OH terminated surfaces can form more Si–O–Si covalent bonds via

$$Si–OH + Si–NH_2 \rightarrow Si–O–Si + NH_3 \quad (3)$$

In addition to forming Si–O–Si, the following reaction may also take place when the two Si–NH_2 terminated surfaces are in sufficient proximity [154]. It is worth noting that this process is less likely to occur because more hydroxyl groups are generated than amino groups.

$$Si–NH_2 + Si–NH_2 \rightarrow Si–N–N–Si + H–H \quad (4)$$

The bond energy of each Si–N bond is 4.6 eV which is very close to the Si–O bond of 4.5 eV (the bond energies of molecules involved in Si-based materials are listed in Table 6). Therefore, the number density of the Si–NH_2 groups plays an important role in the bonding strength. To avoid the formation of an internal gas pressure that might lead to low bonding energy, the chemical by-product H_2 must be eliminated from the bonding contact. Moreover, due to the smaller size of hydrogen molecules (diameter of 2.5 *vs.* 3.3 Å of water), hydrogen molecules can diffuse in oxide much faster than water molecules. The bonding energy of wafer pairs with an NH_4OH dip has been shown to increase quickly with storage time and reaches a much higher value than that of wafer pairs without an NH_4OH dip [155]. Low-temperature annealing can also be utilized to close nanogaps containing unbound active surface groups. The applied heat induces the local deformation of the unbound activated surface groups, allowing the remaining surface groups to react with their neighboring groups, closing nanogaps and enhancing surface bonding. Simultaneously, products such as H_2O, NH_3, and H_2 slowly diffused through the partially dehydrated layer or into the bulk, filling oxygen gaps.

Table 6 Bond energies of molecules involved in the bonding of Si-based materials [156]**.**

Bond elements	Bond energy (eV)
Si–Si	1.9
Si–O	4.5
Si–N	4.6
Si–F	5.6

Silicon wafers can also be hydrophilically activated using plasma to lower the annealing temperature. It is shown that more aggressive ion bombardment (RIE) techniques produce a low-density interface layer that fills the gaps caused by surface roughness over the course of tens to hundreds of hours of storage or low-temperature annealing. This is not the case with chemical activation or ambient plasma, such as microwave-generated plasma. It is also shown that RIE bombardment-style plasmas tend to smooth surface roughness while ambient plasma treatment does not. Plasma activation effectively covers a siloxane surface with hydroxyl groups while causing essentially no topological alterations. RIE plasma activation results in a low-density, highly active oxide layer coated by a dense layer of hydroxyl groups. After a low-temperature anneal, this low-density layer plastically deforms to fill microgaps, resulting in extraordinarily high strength bonding of more than 2.5 J/m^2 [157]. In native oxide-covered wafers, the high energy bombardment creates a damage layer in the silicon, and this, combined with the low-density oxide, allows interfacial moisture to easily oxidize the crystalline silicon, releasing large quantities of hydrogen at annealing temperatures above 200 °C. It has been hypothesized that when the silicon surface is plasma treated, a thin, porous plasma oxide is formed, which is very reactive and attracts excess water [158]. The porous silica structure is most likely created by the physical impact of energetic ions on the silicon dioxide surface. The water dip after plasma treatment rinses away possible particulate contamination and nonvolatile contaminants from the plasma treatment and enables spontaneous bonding [159]. Further, when the two wafers are brought into contact, the bonding is spontaneous since the hydrogen bonding interactions of the water simplify the contact of the two wafer surfaces

and therefore decrease the risk of forming voids due to trapped air. Water prevents the surface hydroxyl groups from instantly reacting with one another, whereas porous silica enables fast diffusion of water from the bonded interface, allowing the hydroxyl groups at the wafer surfaces to react with each other, forming covalent bonds as shown in (1.

Typical plasma treatment employs oxygen [158], argon [160], or NH_3 [161] RIE or ICP RIE. There are many papers concerning plasma-activated wafer bonding, typically reporting on a new plasma generator source or an optimized set of parameters that allow for high-strength bonding at low annealing temperatures with minimal annealing voids. A significant number of these results are applicable only to the precise experimental setup of the reporting authors or are simply unrepeatable. In this research, argon plasma surface activation was developed using SAMCO ICP RIE for surface activation before bonding. 6-inch wafers were used to test the wafer bonding, and the silicon wafers have 500 nm thermal oxide. The wafers were cleaned with Piranha for 15 minutes prior to the Ar plasma treatment in the ICP-RIE. To compare the efficacy of the NH_4OH dip with the Ar plasma treatment, some wafers were soaked in NH_4OH for 30 minutes. The third batch of wafers had a 30-minute NH_4OH dip followed by an Ar plasma treatment in ICP-RIE. During the exposure, the coil power, platen power, and process pressure were varied within the range of the values set. In the ICP-RIE, a chamber pressure of 4 Pa, an Ar flow rate of 50 sccm, a platen rf power (bias) of 12 W, a coil rf power (ICP) of 600 W, and an exposure time of 30 seconds were used (recipe shown in Figure A 4). After plasma exposure, the wafers were immediately dipped in deionized water, spun-dried, and bonded in a cleanroom environment. The substrates were brought together, and the spontaneous bonding was

initiated by hand-pressing the center of the wafer. To achieve an irreversible bonding of the pre-bonded substrates, an annealing process was conducted in a programmable furnace (Model BF51894C-1, Lindberg/Blue M) at 350 °C for 12 hours with a heating rate of 2 °C/min and a cooling rate of 4 °C/min.

Since the effectiveness of the plasma treatment highly depends on the presence of hydroxyl and amine groups on the surface, X-ray photoelectron spectroscopy (XPS) was used to obtain information on the surface-element composition as well as the chemical state. XPS analyses were carried out with PHI Versaprobe II XPS using a monochromatic Al Ka X-ray radiation source with an excitation energy of 1486.6 eV (Physical Electronics, MN, USA). Samples are transferred into the XPS ultrahigh vacuum chamber through an intro chamber that is pumped down to 4×10^{-4} Pa. The XPS data collection commenced when the ultrahigh vacuum analysis chamber reached $\sim 2 \times 10^{-8}$ Pa. The survey and high-resolution scans were performed on all of the samples. The standard take-off angle used for the analysis was 45°, producing a maximum analysis depth in the range of 3-5 nm. The spectra were recorded from at least three different locations on each sample. The analyzer pass energy was set to 117.4 eV for survey spectra and 23.5 eV for high-resolution elemental spectra, which enabled resolutions of 1.76 eV and 0.35 eV, respectively. The survey spectra covering a wide binding energy range of 1100 eV to 0 eV were acquired with a 1.0 eV step, while high-resolution elemental spectra were acquired with a 0.1 eV step. High resolution scans focused on N(1s), C(1s), O(1s), and Si(2p) photoelectron lines. Low-energy electrons were used for charge compensation to neutralize the sample. All the samples were prepared at the same time, and a total of 12 samples were analyzed (the

sample arrangement is shown in Figure A 5). The spectra were analyzed using the CasaXPS software and charge-corrected to the main line of the C(1s) spectral component (C–C, C–H) set to 284.80 eV. Once calibrated, the spectra were deconvoluted using a Gauss-Lorentz function with an iterative Shirley background correction and fitted to symmetric Gauss-Lorentz curves with the line shape, peak width, and binding energy being the adjustable parameters. No *in situ* cleaning was applied to the samples before measuring.

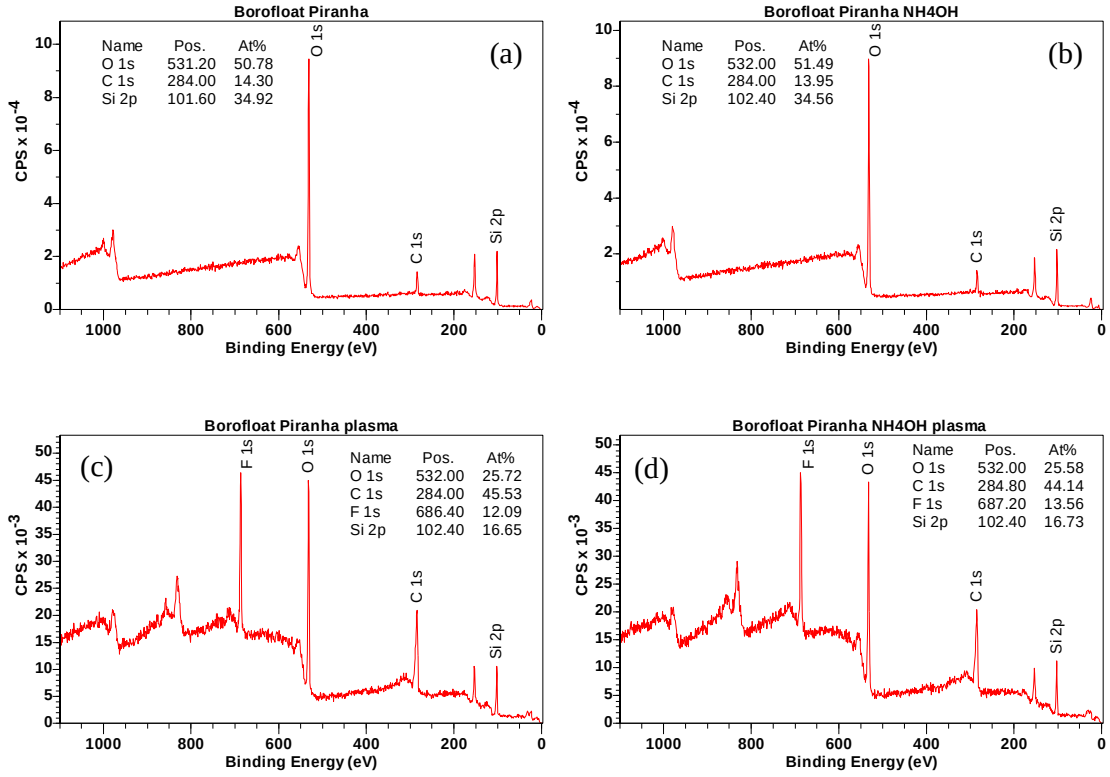

Figure 22 XPS survey spectra of the borosilicate glass substrates treated with (a) 15 minutes Piranha cleaning; (b) 15 minutes Piranha cleaning + 30 minutes NH_4OH soaking; (c) 15 minutes Piranha cleaning + 30 seconds Argon ICP RIE plasma; (d) 15 minutes Piranha cleaning + 30 minutes NH_4OH soaking + 30 seconds Argon ICP RIE plasma. No C correction was performed.

The XPS survey spectra of each substrate after each treatment, *i.e.*, 15 minutes of Piranha cleaning, 15 minutes of Piranha cleaning + 30 minutes of NH_4OH soaking, 15 minutes of

Piranha cleaning + 30 seconds of Argon ICP RIE plasma, and 15 minutes of Piranha cleaning + 30 minutes of NH_4OH soaking + 30 seconds of Argon ICP RIE plasma, are shown in Figure 22 for borosilicate glass, in Figure 23 for silicon with 500 nm thermal oxide, and in Figure 24 for fused silica (the 15 minutes of Piranha cleaning + 30 minutes of NH_4OH soaking + 30 seconds of Argon ICP RIE plasma spectrum is missing), respectively. Carbon contamination is ubiquitous on practically all materials exposed to ambient conditions, and the intensity of the C(1s) on the activated surfaces has greatly increased. The Si(2p) and O(1s) binding energies found in these materials are in good agreement with the reported values [162]. It is surprising that the F1s peak can be seen after the Ar plasma treatment. The F(1s) peak at 687.2 eV (after shifting the C(1s) to 284.8 eV) can be assigned to the formation of the F–Si bonds on the surface [163]. The F–Si bond is the most possible on the surface compared to the peaks of the F–C at 688.9 eV and the F–O at 692.1 eV bonds, and it is close to the F–Si bond for F atoms bonded to SiO_2 at 686.6 eV [164] and 687.1 eV [165]. This peak can be introduced after $CF_4 + O_2$ plasma treatment by substituting O atoms with F atoms in silicon oxide as the F radicals discharged from ($O_2 + CF_4$) plasma break the Si–O bond. During this study, no CF_4 is intentionally introduced into the chamber. Florine can come from the residual gas in the ICP RIE chamber as a low amount of CF_4 can introduce the F–O peak on the surface (CF_4:O_2 gas flow = 1.25:500 sccm) [165]. Nevertheless, incorporating Si–F on the surface promotes strong bonding at the interface as fluorinated oxide promotes the diffusion of water inward away from the bonding interface [165].

High-resolution XPS spectra of the samples treated at different conditions are shown in Figure 25, Figure 26, and Figure 27 together with their deconvolution. Detailed analysis of the O(1s) emission peak showed evidence of silanol species (Si–OH) on the surface and the presence of a small amount of non-crystalline, amorphous silica, leading to the low energy wing of the O(1s) line. After wet or plasma surface treatments, the peak of the siloxane component (Si–O–Si) on borosilicate glass and silicon substrates with thermal oxide shifted to a higher energy. In contrast, on fused silica substrates, it shifted to a lower energy. The peak at the lowest binding energy can be assigned to SiOx species [166], which are present in a relatively significant amount after plasma treatment. The peak with medium binding energy can be well assigned to Si–OH groups [166], which increased significantly by more than 5 percent following any treatment on a silicon wafer with 500 nm thermal oxide. However, for the other two materials, this percentage only increases following plasma treatment. The full width at half maximum (FWHM) of the Si–OH peak on the modifier-containing glass, like borosilicate glass, is greater than those of the thermal oxide and fused silica. The Si–OH peak on all substrates generally shifts to the higher binding energy after either wet or plasma surface treatments, and the FWHM widens as well. The binding energy change and related peak position shifts in the XPS spectra suggest that the chemical state of oxygen changes with chemical composition. The N(1s) peaks indicate the existence of two types of nitrogen bonds on the surface. For borosilicate glass, the XPS spectra of the N(1s) can be found even on Piranha-cleaned and NH_4OH-treated surfaces, and the peaks at 402.34 eV and 401.83 eV might represent a dative bonding ($Si–NH_2$ + – C) with the surface [167]. Whereas the peaks at 400.02-400.09 eV and 400.22 eV represent

free amine groups (–NH_2) on the surface [168], which were produced only after plasma treatment. Interestingly, on a silicon substrate with 500 nm thermal oxide, the O(1s) and Si (2p) peaks shifted to the higher energy side by 0.8 eV after wet or plasma treatments. Additionally, it took overnight to accomplish the XPS analysis after plasma treatment in our case, indicating Si–OH and Si–NH_2 bonds are chemically stable on the surface. In summary, during the plasma treatment for all substrates, silicate rings on the glass surface are broken, and then more activated groups (–OH and –NH_2) are attached to the Si atoms.

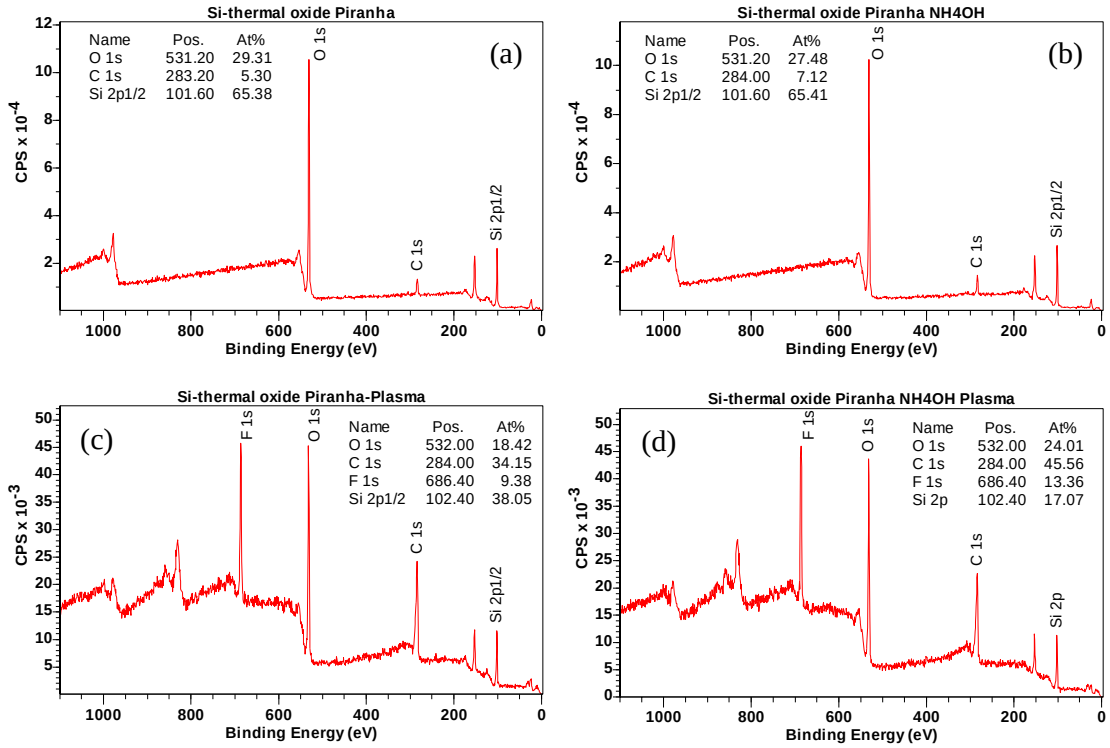

Figure 23 XPS survey spectra of silicon substrates with 500 nm thermal oxide treated with (a) 15 minutes Piranha clean; (b) 15 minutes Piranha cleaning + 30 minutes NH_4OH soaking; (c) 15 minutes Piranha cleaning + 30 seconds Argon ICP RIE plasma; (d) 15 minutes Piranha cleaning + 30 minutes NH_4OH soaking + 30 seconds Argon ICP RIE plasma. No C correction was performed.

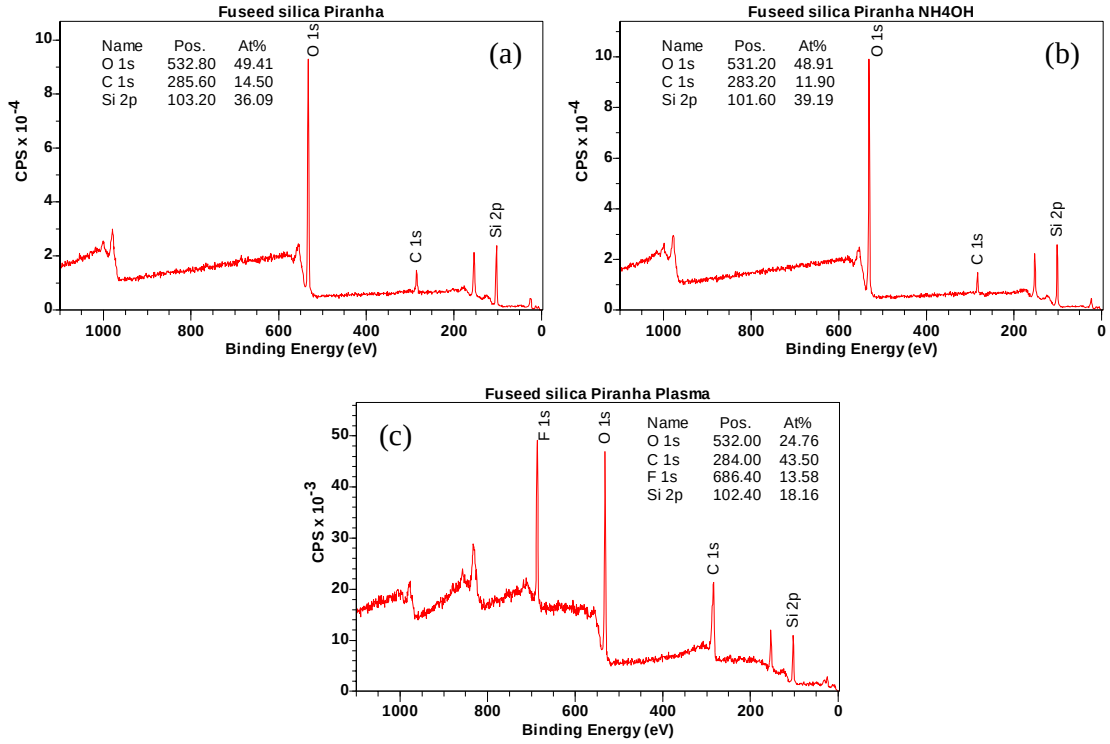

Figure 24 XPS survey spectra of fused silica substrates treated with (a) 15 minutes Piranha clean; (b) 15 minutes Piranha cleaning + 30 minutes NH_4OH soaking; (c) 15 minutes Piranha cleaning + 30 seconds Argon ICP RIE plasma. No C correction was performed.

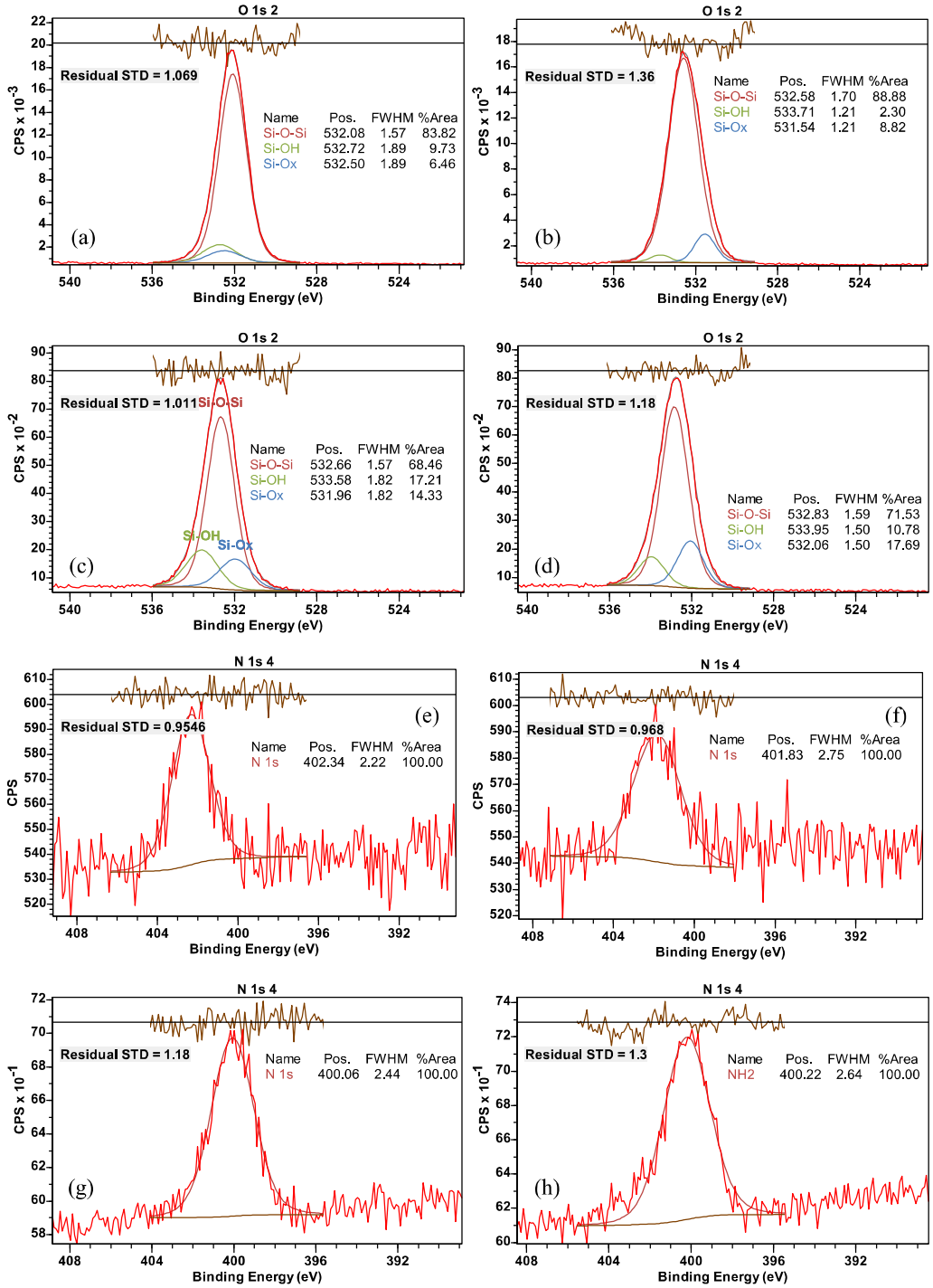

Figure 25 High-resolution XPS spectra of borosilicate glass substrates treated with (a) (e) 15 minutes Piranha clean; (b), (f) 15 minutes Piranha cleaning + 30 minutes NH_4OH soaking; (c), (g) 15 minutes Piranha cleaning + 30 seconds Argon ICP RIE plasma; (d), (h) 15 minutes Piranha cleaning + 30 minutes NH_4OH soaking + 30 seconds Argon ICP RIE plasma. (a)-(d) O(1s), (e)-(h) N(1s). After C correction.

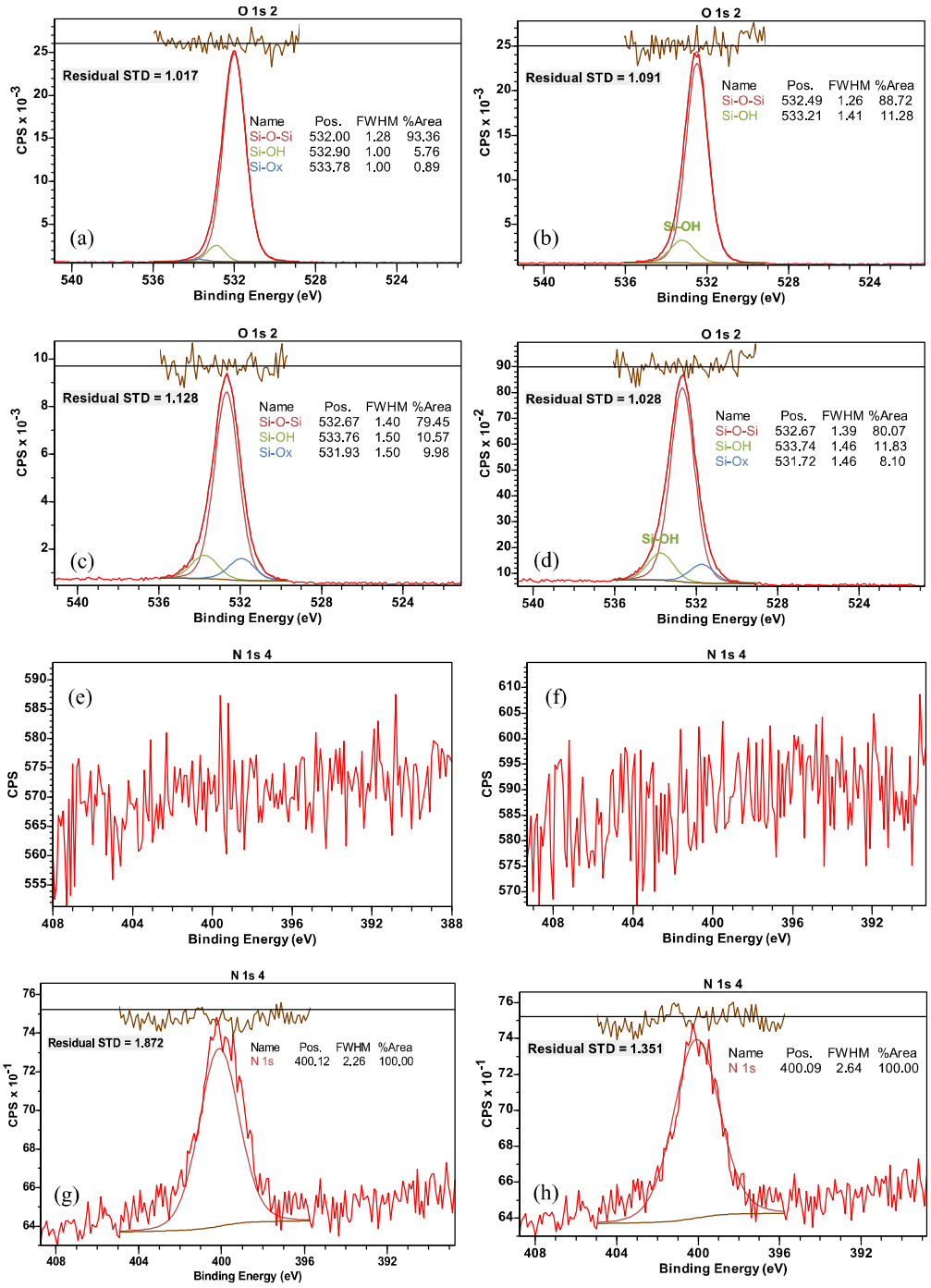

Figure 26 High-resolution XPS spectra of silicon substrates with 500 nm thermal oxide treated with (a), (e) 15 minutes Piranha clean; (b), (f) 15 minutes Piranha cleaning + 30 minutes NH_4OH soaking; (c), (g) 15 minutes Piranha cleaning + 30 seconds Argon ICP RIE plasma; (d), (h) 15 minutes Piranha cleaning + 30 minutes NH_4OH soaking + 30 seconds Argon ICP RIE plasma. (a)-(d) O(1s) and (e)-(h) N(1s) peak. After C correction.

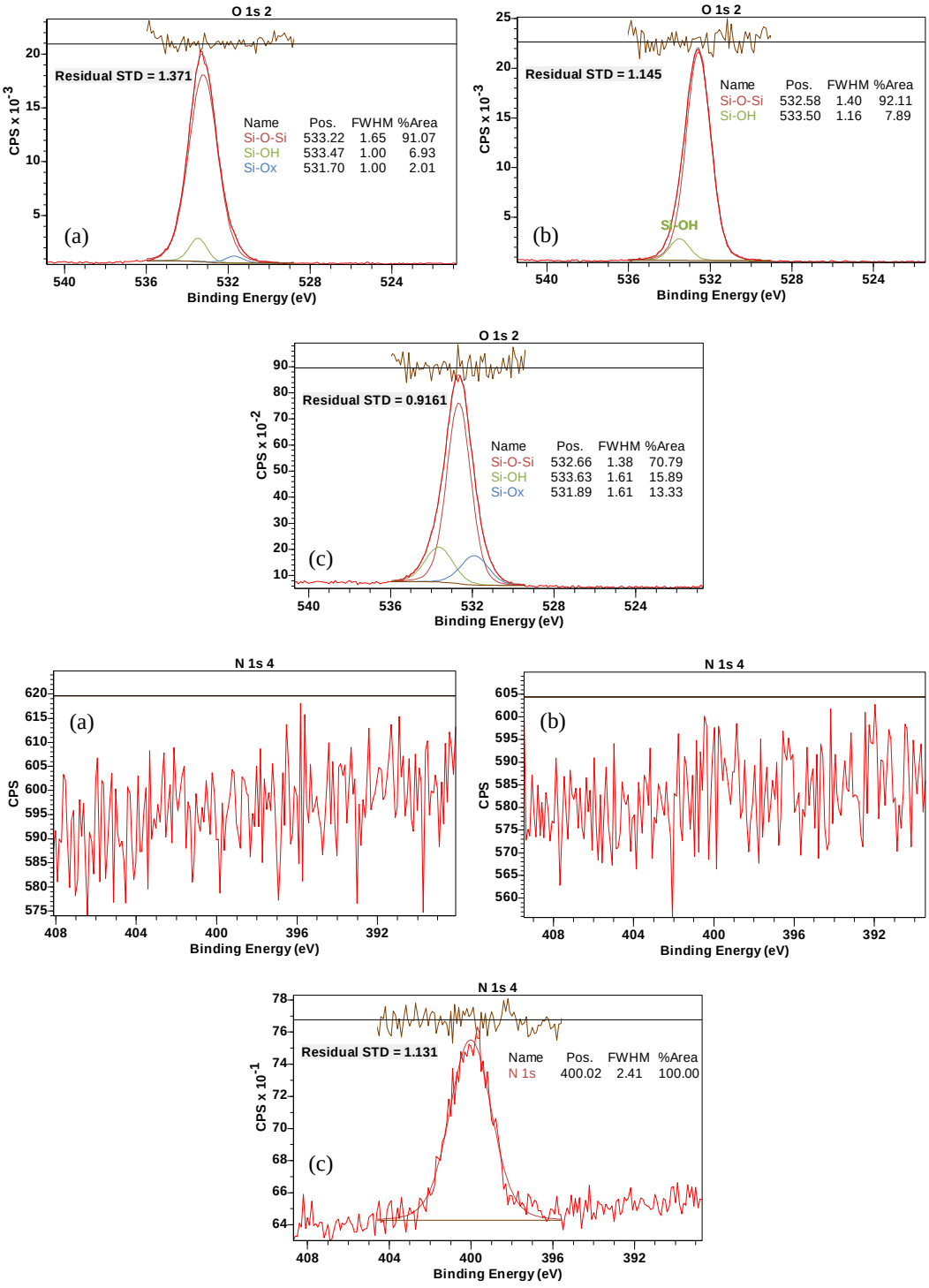

Figure 27 High-resolution XPS spectra of fused silica substrates treated with (a), (e) 15 minutes Piranha clean; (b), (f) 15 minutes Piranha cleaning + 30 minutes NH_4OH soaking; (c), (g) after 15 minutes Piranha cleaning + 30 seconds Argon ICP RIE plasma. (a)-(c) O(1s) and (d)-(g) N(1s) peak. After C correction.

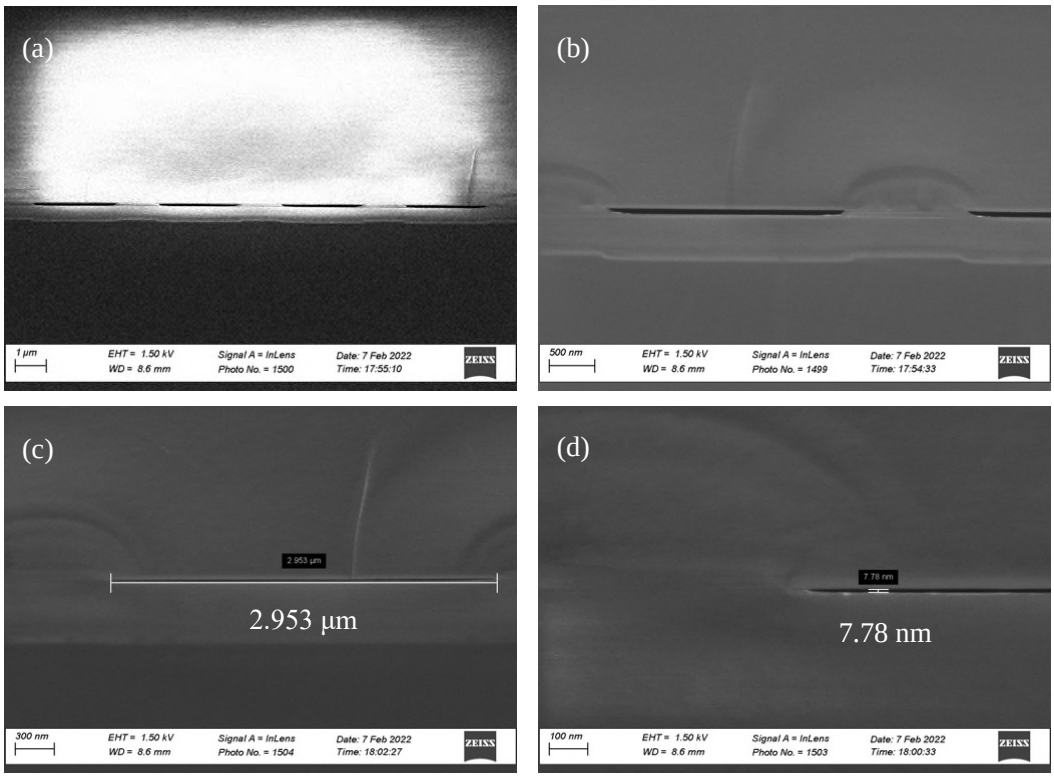

Figure 28 SEM images of the cross-section of the wafers bonded using fusion bonding at 350 °C with Ar plasma surface activation. (a)-(b) Channels with 52 nm depth and 3 μm width. (c)-(d)) Channels with a depth of 7.78 nm and width of 2.953 μm, equivalent to an aspect ratio of 0.0026 (depth over width).

After a post-annealing at 350 °C, strong bonding interfaces with no defects or microcracks were obtained. Examples of the cross-section image (SEM) of the bond substrates are shown in Figure 28. In the first example (Figure 28 (a)-(b)), the depth of the nanochannel is 52 nm, and the width is 3 μm. And in the second example (Figure 28 (c)-(d)), the depth of the nanochannel is 7.78 nm, and the width is 2.953 μm, equivalent to an aspect ratio of 0.0026 (depth over width), which is the minimum aspect ratio reported according to the author's knowledge. With prior knowledge of the chemical bonds that contribute to surface bonding, XPS can be used to characterize the efficacy of surface activation without the need for annealing.

2.4 Additional remarks on photoresist thickness optimization

To pattern microchannels with 3 μm depth on Si, a thicker photoresist, 2 μm of AZ3312 (actual photoresist thickness measures around 1.8 μm), was used. Intermittent cooling during RIE etching was used to reduce photoresist heating (recipe in Appendix Figure A 2 (c)). The selectivity of this resist under the current baking and etching conditions is 2:1. After etching, there was 307 nm photoresist left; therefore, 2 μm of thickness is sufficient to protect the 300 nm channels already patterned on the wafer. As fused silica etches much slower compared to Si (35 nm/min *vs.* 180 nm/min), a 2 μm photoresist is not sufficient to withstand long RIE etching. All the 2 μm photoresist was etched away, and 1.1 μm of the additional fused silica underneath was etched, which means that the 2 μm photoresist lasted for 1.9 μm of etching. Therefore, a 5 μm AZ10XT was used for patterning microchannels on fused silica wafers.

The fabricated device (on silicon substrate) and the cross-section of the nanochannel region are shown in Figure 29.

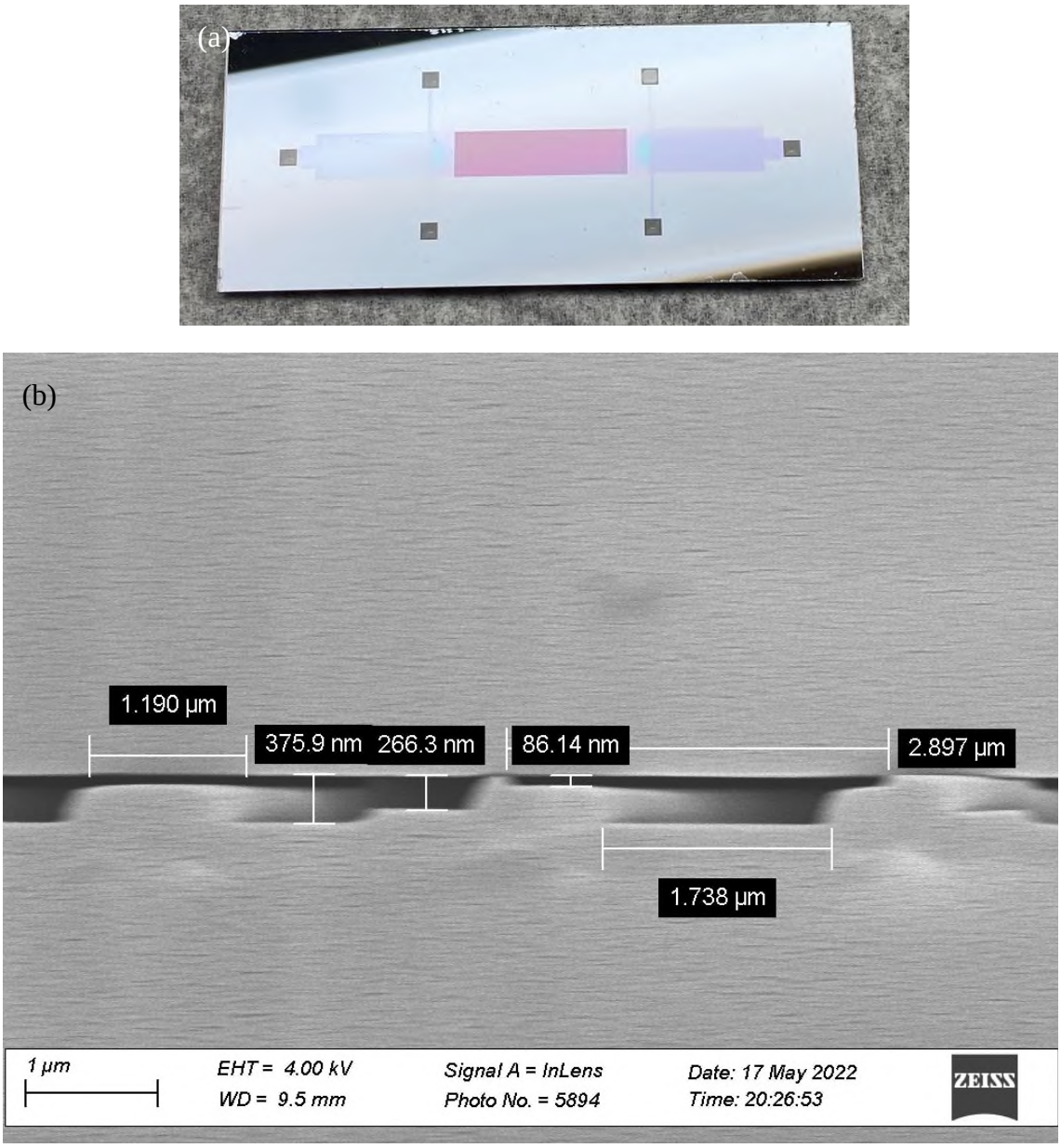

Figure 29 (a) Final device fabricated in the cleanroom. (b) Cross-section of the nanochannel.

CHAPTER 3. CONTINUOUS ONLINE TITER MONITORING USING NANOFLUIDIC SYSTEM

Nanofluidics, the study of the behavior, manipulation, and control of fluids in channels or pores with at least one characteristic dimension below 100 nm [169], is currently attracting significant interest. The large surface-to-volume ratio in nanochannels results in capillarity-induced negative pressure in water [170] and diffusion-limited reactions [171]. Nanofluidics is much more than a scaled-down version of microfluidics, as fluids on this small-scale display unique properties not observed on the microscale or in bulk. For instance, water confined in nanochannels possesses exceptional structural and dynamical features, such as a higher viscosity, a lower dielectric constant and refractive index, and a higher proton mobility compared to bulk water [172]. Other unique, confinement-induced effects in nanochannels were reported in terms of hydrodynamic flow, conductivity, and ionic transport. Some ion transport processes that are absent or inconsequential in microchannels become prevalent in nanochannels, such as the localized amplification of the electric field and the overlap of the electric double layer (EDL). The strong electrostatic interaction between charged surfaces and ions in the nanochannel results in surface-charge-governed ion transport, which leads to ion selectivity [173]. In addition, in such a surface-governed space, the effect of the electric double layer (EDL, formed near the surface of a charged nanochannel) on the nanoscale space is not negligible. The conductivities measured in the nanochannels and nanopores were greater than those of the bulk liquid because the EDL conductivity is often greater than that of the bulk liquid. Debye length,

which is dependent on the ionic strength of the liquid phase, determines the thickness of the EDL. For concentrations in the millimolar range, the Debye length is between 1 and 10 nm, while in the micromolar concentration range, the Debye length is between 10 and 300 nm. By flowing a buffer with a high ion concentration in a narrow channel, the thickness of EDL can exceed the channel size (EDL overlap). When an electric potential is given to the nanochannel, osmosis of ions induces the flow of liquid, which is referred to as electro-osmotic flow (EOF) [174].

Nanofabrication and fluidic control techniques have facilitated the development of nanofluidic devices in bioanalysis. It has been demonstrated that nanochannels with critical dimensions in the sub-100 nm range are achievable. This size range is comparable to that of biomolecules, such as DNA, viruses, and proteins, allowing direct manipulation of biomolecules via interactions with nanostructures. For bioanalysis, numerous nanofluidic device configurations, such as nanocavities, nanogaps, nanopores, nanopipettes, and nanoporous membranes, have been developed. The physical confinement and denaturation of DNA molecules in nanofluidic channels, for instance, have enabled the engineering of single DNA molecules [175]. Utilizing the elongation of DNA molecules in nanofluidic channels, optical mapping of specific regions of interest was accomplished, which allows for high-throughput analysis without the use of enzymes [176]. Nanofluidic devices have been used to separate DNA and large macromolecules. Periodic structures of deep microfluidic and shallow nanofluidic channels were built to generate entropic traps for the size-dependent separation of DNA and protein molecules [177], [178], whereas an array of nanopillars was used to separate long DNA molecules [179]. The difficulty in detection is

the major impediment to using nanofluidic devices in analyses [169], [180]. In general, the number of molecules in a nanofluidic channel is relatively low. For instance, when the concentration of an analyte is 1 μM, there are 0.6 analyte molecules per 100 nm^3. For detection in a nanofluidic device, laser-induced fluorescence microscopy with single-molecule sensitivity is often used. Electrokinetic trapping in nanochannels was utilized to preconcentrate proteins and peptides a million-fold [181].

Anisotropic Nanofilter Array (ANA) has been developed for continuous-flow biomolecule separation, allowing for multivariate (size, folding, and activity) analysis of the biomolecules [122]. Steric hindrance of biomolecules within nanochannels enables the separation of biomolecules with sizes equivalent to or less than the nanofilter gap size [177]. The engineered structural anisotropy in the ANA induces biomolecules of varying sizes to migrate along different trajectories, leading to efficient and continuous separation. Nanofluidic devices as alternative monitoring systems could enable a comprehensive biologics quality assessment, including size, folding, and activity. Simple continuous operation and better detection sensitivity and resolution make it a promising candidate for protein quality assessment. Our group previously demonstrated the detection of protein aggregation down to around 50 ng/mL by using a built-in post-concentration step in denatured protein sizing and separation [122]. Continuous online monitoring of the protein size during perfusion culture using ANA structures has also been accomplished [182]. While the aggregation content of mAb products is an important safety CQA, it is also crucial to develop assays that measure the functional attributes of biologics (*e.g.*, binding to the antigen) directly.

This thesis demonstrates using nanofluidic devices to measure the titer (activity) of monoclonal IgG antibodies (adalimumab) directly in CHO cell culture supernatant with continuous sample sampling. Protein titer measurement using the nanofluidic system relies on selective interaction between the indicator molecule (TNF-α) and the analyte mAb (adalimumab) in the sample matrix. TNF-α was selected as the indicator due to an expected selectivity towards the Fab region of adalimumab and, hence, not interacting with other components of the sample matrix. The binding affinity between TNF-α and adalimumab is high [183], although it is highly dependent on the buffer properties such as the ionic strength and pH [184]. Furthermore, the TNF-α was considered a promising indicator due to the relatively small hydrodynamic size compared with adalimumab since the size difference between the indicator and the indicator-analyte complex is critical to ensure the selective concentration in the nanofluidic device. In addition, Adalimumab is one of the TNF-α inhibitors that have been successfully developed and employed in the clinical treatment of autoimmune diseases due to the involvement of TNF-α in the pathogenesis of autoimmune diseases [185]. Using TNF-α as the indicator offers the advantage of probing the activity of the adalimumab as early as the upstream bioprocessing. TNF-α was conjugated to a fluorophore, and due to the size-selective concentrating effect of the nanofilter array, only the large bound complex is concentrated along the centerline of the device. Hence, the intensity of the fluorescent signal of the centerline is determined by the concentration of the TNF-α-bound adalimumab in the supernatant, as long as sufficient TNF-α is present in the assay. The nanofluidic device was calibrated using supernatant samples containing adalimumab of known titers, and the standard calibration curve was

subsequently used to access the adalimumab of unknown titer in unprocessed CHO cell culture supernatant. The titers measured by the nanofluidic assay were compared with those determined by biolayer interferometry (BLI).

3.1 Design and operation of the nanofluidic device

The nanofluidic devices used for continuous titer monitoring were designed based on the previous generation ANA device developed in our group [122] (refer to Chapter 2 of this thesis for full detail). Briefly, the ANA device consists of periodically patterned shallow channels (85 nm) and slanted deep channels (250 nm) oriented 45° relative to the shallow channels. The electric field is applied in the direction of the shallow channel direction (x-axis, Figure 30 (a)). On the application of an electric field, undenatured proteins migrate with the electroosmotic flow in the nanochannels to the side with a lower electrical potential (the main flow direction). For molecules smaller than the dimensions of the channels, the nanofilter can separate molecules of different sizes based on the Ogston sieving effect [186]. In this regime, the configurational freedom of the molecules inside the shallow channel is limited due to steric repulsion from the wall, and this creates a size-dependent configurational entropic barrier for the passage of the molecules from the deep channel to the shallow channel in the nanofilter. Smaller molecules will have less resistance to jumping across from the deep channel to the shallow channel as they migrate across the nanofilter array, so their trajectory marginally deviates from the main flow direction. On the other hand, larger-sized molecules encounter a larger configurational entropic barrier when transitioning from the deep channel to the shallow channel, resulting in a lower frequency of jumping across the nanofilter to the shallow channels [187]. Therefore, larger

molecules spend a longer time trapped in the deep region and migrate along the deep channels, thus traveling toward the center of the herringbone structure, and the trajectory has a considerable deflection angle from the main flow direction (Figure 30 (a) and (b)). In this way, molecules of different sizes are differentially concentrated in a continuous-flow manner. The concentration capability of this device is obtained by the herringbone geometry. As large molecules from both sides are drawn towards the center, the center line of a herringbone pattern represents a symmetric boundary condition. In such a situation, the central region becomes a sink where large biomolecules accumulate. Only by hopping across the shallow zone can the trapped molecule escape the local sink. The concentration factor of big biomolecules in the device's center would depend on its diffusion coefficient, trapping time, magnitude of driving forces, and the device's width (which determines the number of molecules to be concentrated in the center). One can also design devices with varying critical depths to achieve optimal separation and concentration of the target biomolecules.

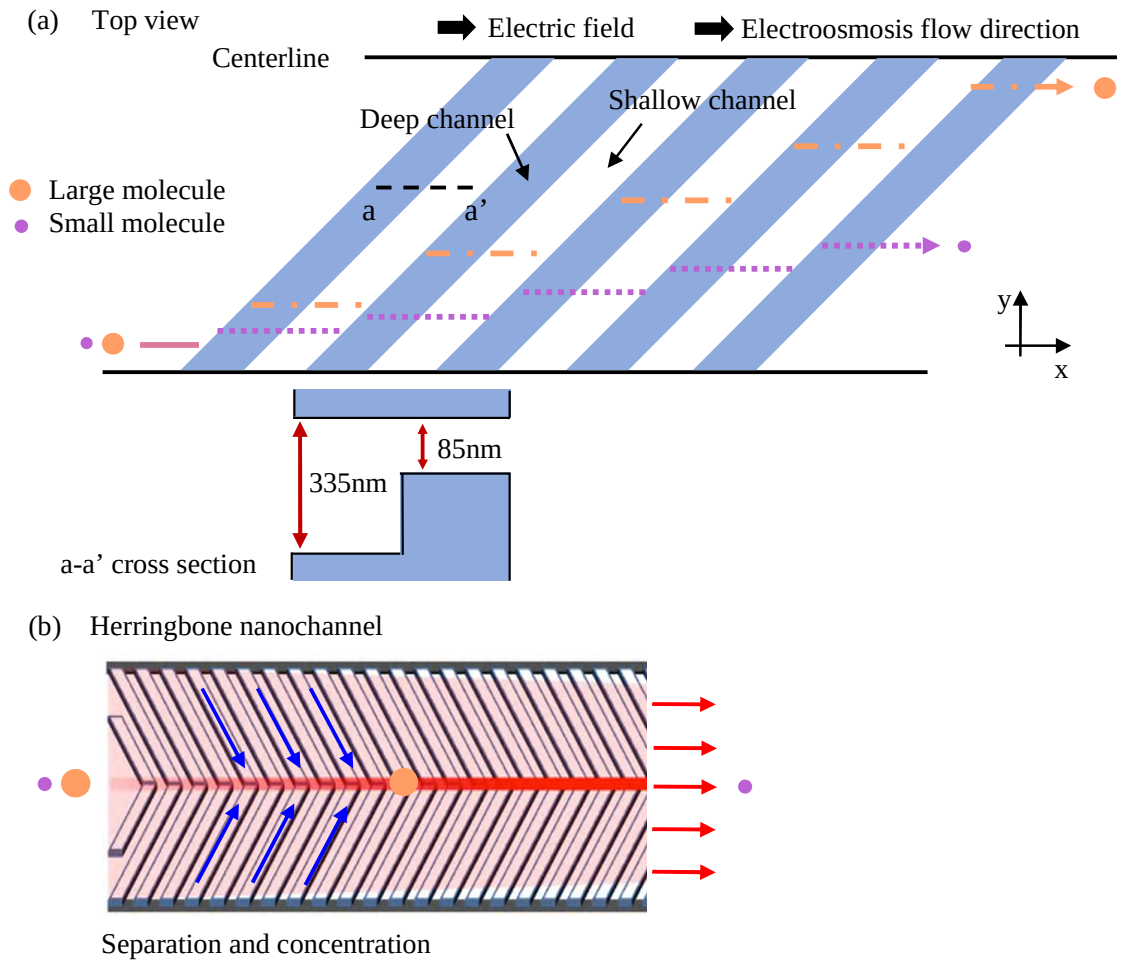

Figure 30 (a) Size-based separation of molecules under electroosmosis flow. The shallow channels are 85 nm deep and the deep channels are 335 nm deep as shown in the cross-section aa' of the nanofilter array. (b) Sized-based separation and selective concentration in herringbone structure nanofilter array.

For continuous monitoring, microfluidic channels are patterned on two sides of the nanofilter array to accommodate fluid loading as connecting channels between the reservoirs and the nanoarray (Figure 31 (a)). A device holder was designed to provide easy sample loading with fluid ports connecting to the inlet and outlet reservoirs of the nanofluidic device and with electrode insertion channels connecting to the side reservoirs of the device (Figure 31 (b)). The nanofluidic device holder, which houses the nanofluidic

device, was connected to the online sample preparation system that can continuously feed the sample and buffer into the nanofluidic device (Figure 32). The continuous sample preparation system performs supernatant sample dilution, as well as mixing with TNF-α-alexa488. Peristaltic pumps (RP-TX series, Takasago Fluidic Systems) were used to adjust the flow rates of the supernatant and the nanofluidic running buffer (contains 712 mM Tris, 1068 mM Boric acid, and 1 w/v% BSA, TB-BSA) buffer. By adjusting the ratio of the flow rates, the supernatant dilution factor can be modified. By matching the flow rates of the diluted supernatant and the TNF-alexa488 streams, the analyte and TNF-alexa488 titers are halved after mixing (1:1 mixing). Diffusion mixing caused a 35-minute delay in the sample preparation system, which could be reduced to a few seconds using a micro-mixer [188]. The electrode inserts of the nanofluidic device holder are connected to reservoirs of the nanofluidic device (Figure 31(d)), and the electric field can be applied through the platinum electrodes (711000, A-M SYSTEMS). The fluorescent intensity was recorded using an Olympus inverted microscope, IX71 (6.4×, binning 4) at 7 mm downstream of the herringbone region with the centerline of the device positioned along the center of the image, as demonstrated in Figure 33. Unless stated otherwise, all the fluorescent signal was collected at the same location. MATLAB was used to analyze the images and calculate the relative fluorescent intensity of the centerline. The intensity signal used for titer quantification is located in the plateau region of the fluorescent intensity curve.

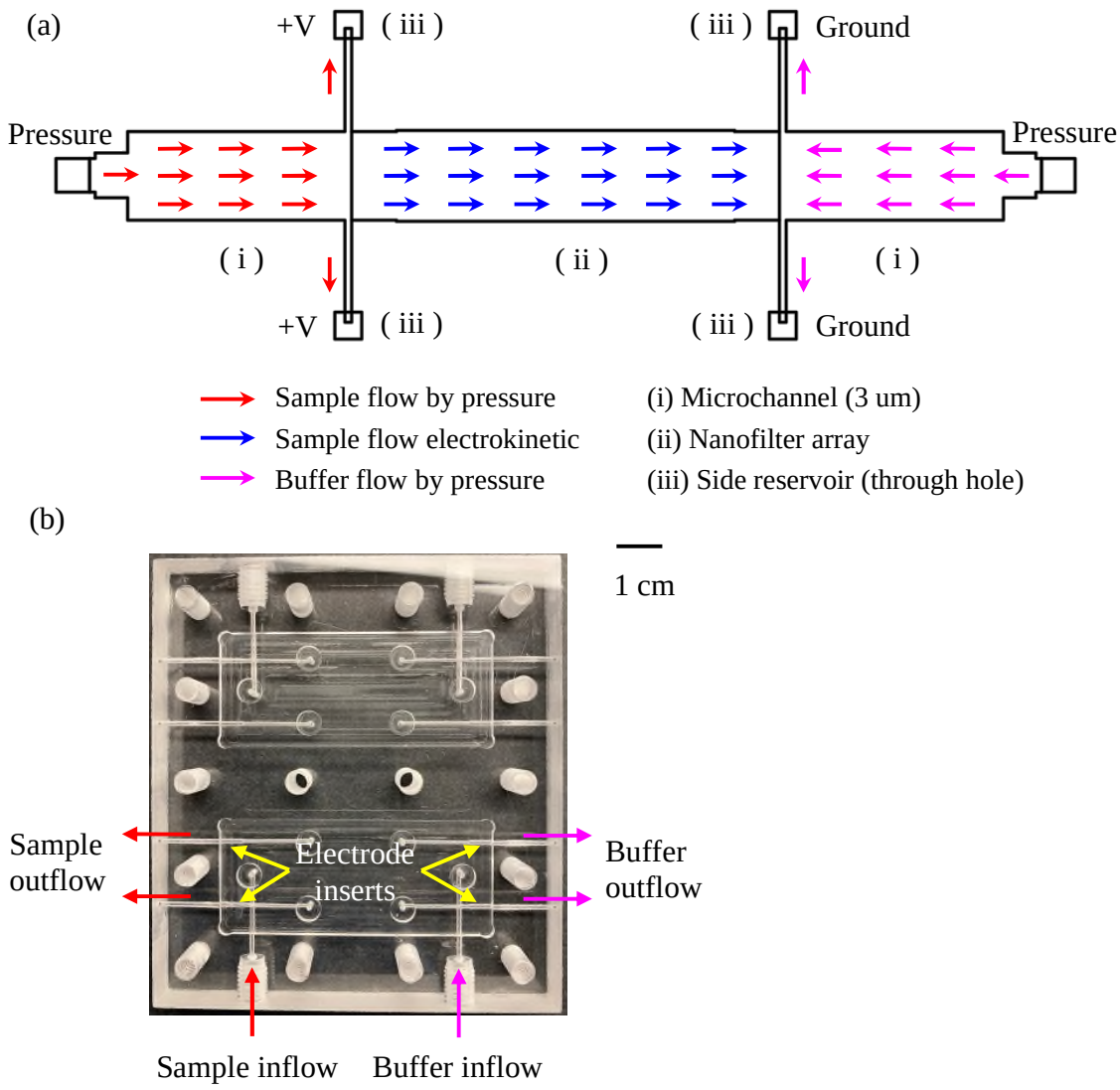

Figure 31 The continuous nanofluidic device used for titer monitoring. The microchannels were designed on both sides of the nanofilter array to accommodate pressure-driven sample or buffer flow. The voltages were applied using electrodes inserted into the electrode inserts in (d), which connect to the side reservoirs of the device. (d) The continuous nanofluidic device holder with fluid loading ports and electrode inserts.

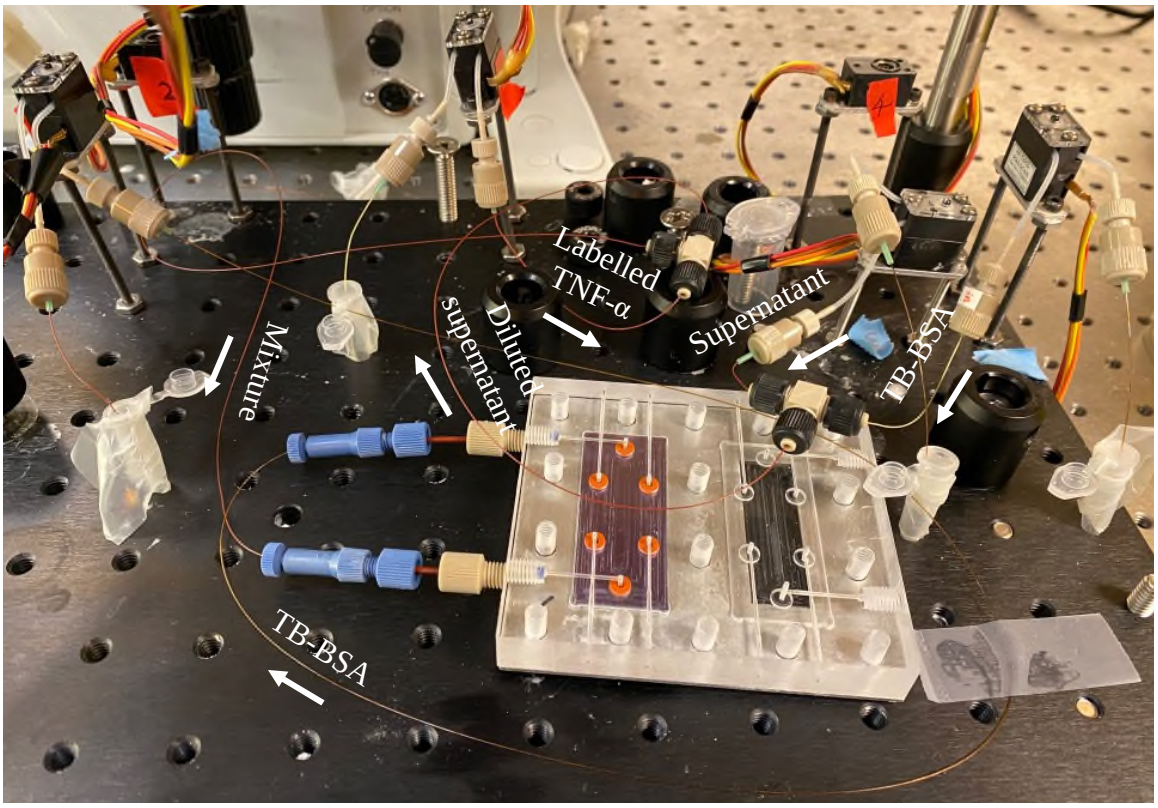

Figure 32 Picture of the continuous titer monitoring system consisting of the nanofluidic device, device holder, and sample preparation system. TB-BSA is the nanofluidic running buffer that contains 712 mM Tris, 1068 mM Boric acid, and 1 w/v% BSA.

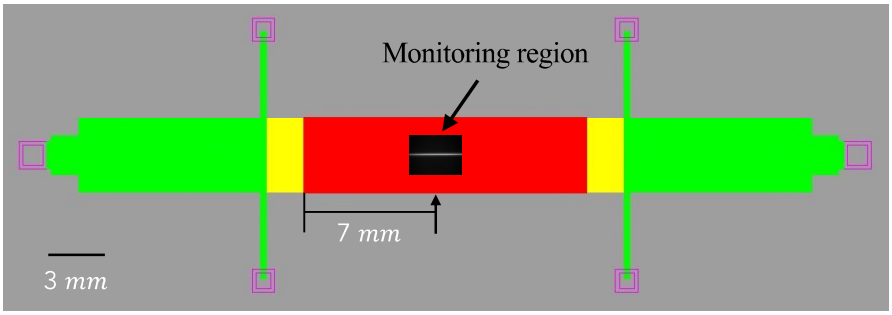

Figure 33 Diagram of the nanofluidic device demonstrating the monitoring region.

The supernatant samples containing adalimumab came from two perfusion bioreactors. Bioreactor #1 is a CHO cell perfusion bioreactor with integrated microfluidic cell retention

devices (the detailed operational procedures using microfluidic cell retention devices were described elsewhere [50]). CHO cells were cultured in a single-use flask with a working volume of 250 mL. The pH (7.1) and dissolved oxygen (60%) of the bioreactor were automatically adjusted by a commercial bioreactor controller (MiniBio reactor 250 mL, Applikon Biotechnology). The inoculated cells were grown and proliferated in the batch mode until the cell density reached 3-4 × 10^6/mL (usually takes 3 days), followed by the perfusion mode with continuous fresh medium addition and cell retention using the microfluidic cell retention system to achieve high cell concentrations (20-40 × 10^6/mL). The fresh cell culture medium was continuously supplied into the bioreactor while the cell culture supernatant was removed by the microfluidic cell retention device. The culture harvest removed from the bioreactor was collected in a harvest bottle, which was replaced daily. An automated cell culture analyzer (FLEX II, NovaBiomedical) was used to monitor the cell culture parameters daily, such as cell concentration, viability, live cell diameter, pH, glucose or lactate concentrations, and oxygen level. Bioreactor #2 is a CHO cell continuous testbed [189], which consists of 4 parallel upstream systems, including 4 perfusion devices (Repligen ATF2), with one bioreactor assembly integrated within a fully continuous downstream system, including Protein A chromatography, viral inactivation, and ion exchange chromatography. The cell-free perfusate samples were collected using a Gilson GX-271 liquid handler. Bioreactor #2 was operated for 25 days, with the perfusion run starting on day 3.

To reduce the online sample preparation time, TNF-α (A37570, Thermos Fisher Scientific) indicator was labeled with fluorescent dye offline. TNF-α was reconstituted in 0.1 M

sodium bicarbonate (S6297, Sigma-Aldrich) at a concentration of 2 mg/mL (pH 8.3). Alexa Fluor 488 TFP ester (A37570, Thermos Fisher Scientific) was dissolved in N, N-Dimethylformamide (DMF, anhydrous, 99.8%, 227056, Sigma-Aldrich) freshly before labeling, and a molar excess of 20 was added to the reconstituted TNF-α solution. The mixture was incubated at room temperature for 1 hour. Then unconjugated fluorophores were removed using Pierce™ Dye Removal Columns (22858, Thermos Fisher Scientific) twice. Afterward, the buffer was exchanged to 1× PBS using Zeba™ Spin Desalting Columns (7 K MWCO, 89882, Thermos Fisher Scientific), and the aliquots were stored at -20 °C for future use. The TNF-α-alexa488 conjugate concentration and the degree of labeling (DOL) were 0.595 mg/mL and 1.37, respectively, as determined using a microvolume spectrophotometer (NanoDrop One, Thermo Fisher Scientific, Wilmington, Delaware, USA) applying the extinction coefficient of TNF-α ($\varepsilon = 60{,}500\ cm^{-1}\ M^{-1}$) at 280 nm [190] assuming trimeric TNF-α.

The isoelectric point (pI) of the recombinant human TNF-α used in this study has a pI of 7.23 (DNASTAR [191]) and 6.98 (Pro pi [192]) respectively, as calculated based on the amino acid sequence provided by Abcam [193], and that of adalimumab is approximately 8.7 [194] with the theoretical value being 8.36 (ExPASy [195], DNASTAR [191]). The pH of the nanofluidic running buffer is chosen at 8, which is achieved by adjusting the molar ratio of the boric acid and tris in the buffer. At this pH, TNF-α is slightly negatively charged, and adalimumab is positively charged.

To determine the ionic strength of the nanofluidic running buffer, it is necessary to consider the buffer-specific pKa of each buffer composition. Any ion i in a nonzero ionic strength solution is surrounded by a number of ions with the opposite charge. This "shielding" effect causes the apparent concentration of the ion i to be less than its actual concentration $[i]$. This effect becomes more prominent as the ionic strength of the buffer increases. Due to this shielding effect, pKa is dependent on the ionic strength of the solution. To circumvent this problem, the concentration of species of interest is replaced by so-called activities. An activity α_i of ion i is defined as

$$\alpha_i = \gamma_i \cdot [i] \tag{5}$$

where $[i]$ is the concentration of the ion i (mol/L) and γ_i is the activity coefficient.

For ionic strengths between 100-500 mM, activity coefficients can be approximated by Davies equation [196]

$$log\ \gamma_i = -A \cdot {z_i}^2(\sqrt{I}\ /\ (1+\sqrt{I}\ ) - 0.2 \cdot I) \tag{6}$$

and therefore

$$pKa = pKa_0 + A \cdot (2z_i + 1) \cdot [\sqrt{I}\ /\ (1+\sqrt{I}\ ) - 0.2 \cdot I] \tag{7}$$

where, A is the Debye–Hückel constant, which is dependent on the dielectric constant of the solvent, and it is generally accepted that A = 0.509 for water at 25 °C; z_i is the charge number of ion i; pKa_0 is the pKa of the buffer at infinite dilution (buffer concentration =

0 M) at 25 °C, *i.e.*, thermodynamic pKa, and is a constant for a particular buffer. For tris and boric acid, pKa_0 are 8.06 [197] and 9.24 [198] at 25 °C, respectively.

The molar ionic strength, I, of a solution is a function of the concentration of all ions present in that solution

$$I = \frac{1}{2}\sum_{i=1}^{n}[i]\cdot {z_i}^2 \tag{8}$$

Using Eq. (6)-(8), the apparent pKa are calculated as 8.20 and 9.38, respectively. And therefore, the ionic strength of the buffer is 240 mM. At this high ionic strength, the thickness of the EDL is calculated based on

$$\lambda = 1e9\cdot\sqrt{\frac{k_b\cdot T\cdot \varepsilon_0\varepsilon_r}{2\cdot I\cdot q^2\cdot A_v}} \tag{9}$$

where, $k_b = 1.380649\times 10^{-23}\,(J/K)$ is the Boltzmann constant, $T = 25 + 273.15\,(K)$ is the absolute temperature, $\varepsilon_0 = 8.8541878128\times 10^{-1}\,(F/m)$ is the electric constant, $\varepsilon_r =$ 80.1 is the relative static permittivity of water, $q = 1.602176634\times 10^{-19}\,(C)$, is the elementary charge, $A_v = 6.022\times 10^{23}$ is the Avogadro constant. λ is calculated as 0.627 nm, much smaller compared to the depth of the shallow nanochannels. Thus, the electrostatic interactions of the analyte with the EDL are minimal, and Ogston sieving dictates the molecular transport behavior [199]. When an electric field is applied, the net free solution mobility of each protein is determined by the combined electrophoretic and electroosmosis mobilities. Under this buffer condition, the direction of the combined

mobility is in the same direction as the electroosmosis flow. Therefore, both protein samples migrate from the anode to the cathode.

3.2 Binding affinity characterization

Generally, experiments to characterize ligand and protein binding are carried out under 'favorable' conditions. For example, binding between adalimumab and TNF-α is typically examined in 1× PBS with cytoplasmic pH (7.4) [200]. High solvent viscosity has been reported to have a negative impact on protein-ligand affinity in general, whereas the dependence of protein-ligand complex formation on ionic strength is complicated, depending on the hydrophobic or hydrophilic nature of the binding site and ligand [184]. The nanofluidic running buffer differs in composition (Tris *vs.* PBS) and has a higher viscosity, pH, and ionic strength. It has been previously demonstrated that the diffusion-limited protein-ligand interactions are inversely proportional to the viscosity of the medium [201]. The direct dependence of binding on ionic strength has been recognized as a common feature of diffusion-influenced protein-protein interactions, and the electrostatic interactions provide the only mechanism for rate enhancement [202]. Changes in pH (5.5-8.5) can alter binding affinity by a factor of 10 [203]. Therefore, the binding between adalimumab and TNF-α in nanofluidic running buffer (BLI assay buffer #2) needs to be analyzed.

The adalimumab antibody sample from bioreactor #2 was used in the binding affinity characterization. The supernatant sample was purified using the Cytiva HiTrap MabSelect SuRe prepacked column (1 mL, 45000512, Fisher Scientific). 1× PBS with pH 7.2

(BupH™ Phosphate-Buffered Saline Packs, 28372, Thermos Fisher Scientific) was used as a binding buffer. 50 mM sodium acetate (Anhydrous, S2889, Sigma-Aldrich) at pH 3.5 (pH adjusted with acetic acid (>=99.7%, 695092, Sigma-Aldrich)) was used as the elution buffer. 1 M Tris-HCl at pH 9.0 (Trizma® base, 93362, Sigma-Aldrich) was used as the neutralization buffer. Buffers were filtered through a 0.2 µm filter (Acrodisc® Syringe Filters with Supor® Membrane, Sterile, 0.2 µm, NC0784274, Fisher Scientific) before use, and the supernatant was filtered through a 0.45 µm filter (Acrodisc® Syringe Filters with Supor® Membrane, Sterile, 0.45 µm, NC0332820, Fisher Scientific). The purification was carried out following the product manual [204]. Cleaning-in-place was performed immediately after the elution. The purified sample was buffer exchanged to 1× PBS, and its concentration was measured using Nanodrop One.

Binding kinetics studies were performed on an Octet RED96 instrument at 30 °C with a shaking speed of 1000 rpm using Octet® Anti-Human Fc Capture (AHC) Biosensors (18-5060, Sartorius). BLI assay buffer #1 is the standard kinetic buffer (1× PBS, 0.02% Tween 20, 0.1% BSA, 0.05% sodium azide) from Sartorius (Octet® Kinetics Buffer 10×, 18-1105, diluted in 1× PBS before use). All assays were performed in 96-well black microplates (Greiner Bio-One 655209). All the buffers were filtered through a 0.2 µm filter before use. Anti-human Fc (AHC) biosensors were loaded into the columns of a biosensor holding plate and pre-hydrated in BLI assay buffer for 20 minutes.

A serial dilution of adalimumab was performed to determine the optimal antibody loading density on the surface of the AHC sensor. These loading optimization experiments showed that the capturing rate of adalimumab on the AHC sensor was relatively high. Therefore,

adalimumab at a low concentration (4 μg/mL) was used in the kinetic assay to avoid oversaturating the sensor. Initial titration of TNF-α concentrations for BLI experiments revealed heterogeneous binding in both assay buffers at higher antigen concentrations (>5 nM). To overcome these effects, low TNF-α concentrations were used (0.25-4 nM), specifically, 0.25, 0.5, 1, 2, 3, and 4 nM. Kinetic assays were performed by first capturing adalimumab (4 μg/mL) for 240 seconds, followed by a baseline step of 300 seconds in the assay buffer. The adalimumab-captured biosensors were then submerged in wells containing TNF-α of different concentrations for 900 seconds (association), followed by a 3600-second dissociation in the blank assay buffer. The adalimumab-captured sensors were also dipped in wells containing only assay buffer (0 nM TNF-α) to allow single reference subtraction to compensate for the sensor drift and the natural dissociation of captured adalimumab. Initial sensor regeneration tests with 500 mM phosphoric acid (ACS reagent, ≥85 wt. % in H_2O, 695017, Sigma-Aldrich) revealed a significant baseline shift, rendering the results not reliable, which was also reported before [205]. Unless specified, fresh AHC biosensors were used without any regeneration step. Binding sensorgrams were first aligned at the beginning of the TNF-α association cycle followed by subtracting the 0 nM TNF-α concentration reference data from all binding curves. A 1:1 Langmuir binding model (Analysis Software version 8.0) was used with a global fit using all analyte concentrations to calculate association and dissociation rates as well as the binding affinity.

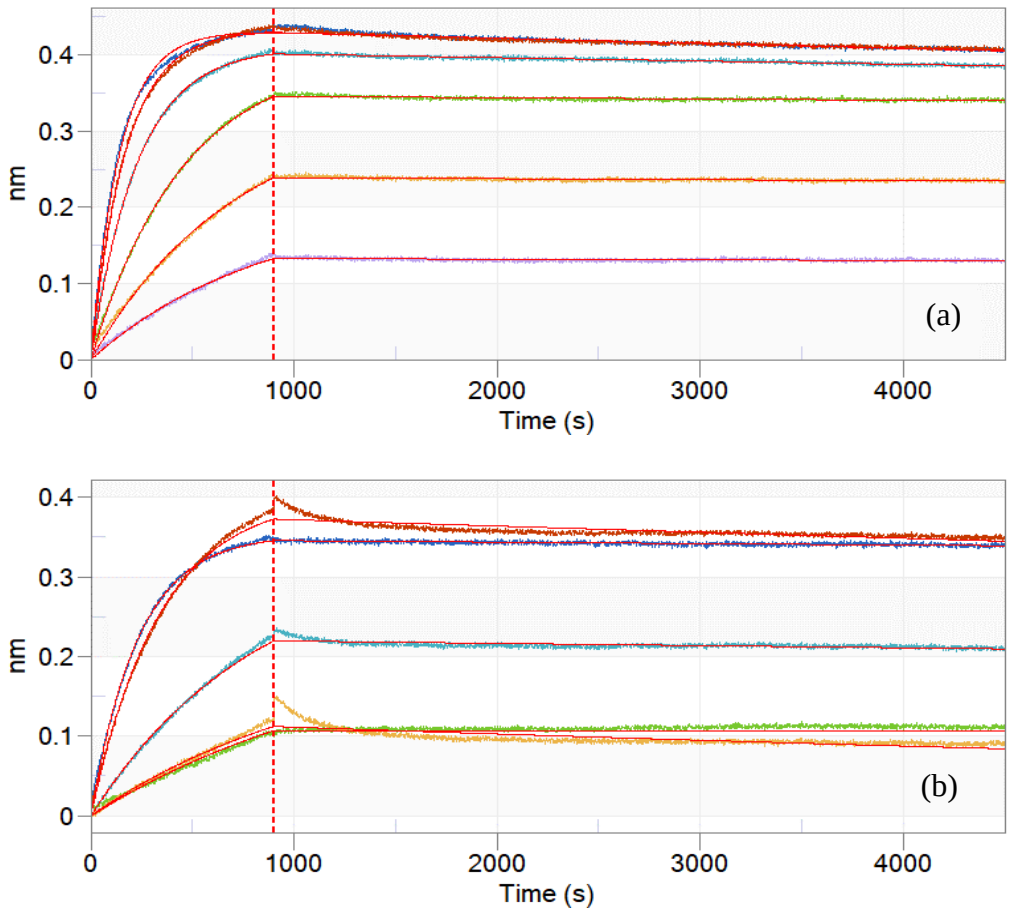

Figure 34 Representative binding curves showing the effect of buffer on antigen binding on the Octet AHC sensor. (a) BLI assay buffer #1, the standard kinetic buffer (1× PBS, 0.02% Tween 20, 0.1% BSA, 0.05% sodium azide). (b) BLI assay buffer #2, the nanofluidic running buffer (712 mM Tris, 1068 mM Boric acid, 1% BSA).

Table 7 Binding kinetic parameters from kinetics assays performed in the standard kinetic buffer.

Conc. (nM)	KD (M)	KD Error	kon(1/Ms)	kon Error	kdis(1/s)	kdis Error
4	9.24E-12	<1.0E-12	1.75E+06	2.88E+03	1.62E-05	1.24E-07
3	8.14E-12	<1.0E-12	1.94E+06	2.34E+03	1.58E-05	<1.0E-07
2	5.10E-12	<1.0E-12	2.17E+06	2.03E+03	1.11E-05	<1.0E-07
1	2.20E-12	<1.0E-12	2.21E+06	3.03E+03	4.86E-06	<1.0E-07
0.5	1.95E-12	<1.0E-12	2.78E+06	9.10E+03	5.41E-06	1.42E-07
0.25	1.40E-12	<1.0E-12	4.67E+06	2.68E+04	6.53E-06	2.15E-07

Table 8 Binding kinetic parameters from kinetics assays performed in nanofluidic running buffer.

Conc. (nM)	K_D (M)	K_D Error	k_{on}(1/Ms)	k_{on} Error	k_{dis}(1/s)	k_{dis} Error
4	4.94E-12	<1.0E-12	1.07E+06	1.24E+03	5.28E-06	<1.0E-07
3	2.20E-11	<1.0E-12	9.79E+05	3.13E+03	2.16E-05	2.34E-07
1	1.10E-11	<1.0E-12	1.20E+06	6.65E+03	1.31E-05	2.14E-07
0.5	<1.0E-12	<1.0E-12	1.41E+06	3.36E+04	<1.0E-07	
0.25	2.63E-11	<1.0E-12	3.05E+06	1.07E+05	8.02E-05	9.97E-07

3.3 Nonspecific binding

The nanofluidic device correlates the fluorescent signal intensity to the adalimumab concentration in the buffer. As a result, preventing nonspecific adsorption is critical since

the observed fluorescent intensity will continue to increase as the binding complex adheres to the surface.

Typically, a surface contributes to protein adsorption by a combination of electrical field overlap with that of the proteins and energy gain from dehydration and ion transfer [211], with hydrophobic dehydration being stronger than electrostatic effects. Electrostatic interactions rely heavily on the charge characteristics of both the protein and the surface, which are affected by the pH and ionic strength of the solution. Generally, protein adsorption on hydrophilic surfaces is mediated predominantly by charge-charge interactions [212]. Electrostatic attraction should increase adsorption if the protein and surface have a different (net) charge, whereas adsorption decreases an increased charge of the same sign.

According to the scientific literature, the pH point of zero charge (PZC) of silica is around 2 [213]. Borosilicate glass, which contains other elements such as aluminum oxide and boron oxide, exhibits a PZC of 1.7-2.0 [214]. The glass surface is highly negatively charged in the alkaline pH region, with the charge not appreciably varying between pH 12 and 7 [215]. Within this range, the surface-exposed Si–OH groups are largely dissociated. The initial Nanofluidic Running buffer (NR buffer #1) employed in this study had a pH of 8.3 (the ionic strength is 231.49 mM). At this pH, non-specific binding to the nanochannel surface was significant, resulting in residual protein in the channel following the experiments, as illustrated in Figure 35. Even after rinsing the channel overnight with the nanofluidic running buffer, the protein was still present, and the fluorescent line can be observed even after withdrawing the voltage applied across the device. Since the

nanochannel surface is not totally hydrophilic, dehydration processes (hydrophobic interactions) can contribute to protein adsorption. The non-ionic surfactant Tween 20 can be used to disrupt hydrophobic interactions. Initial studies conducted for this thesis revealed that Tween 20 was unsuccessful at preventing non-specific adsorption. Therefore, it is considered that the primary forces driving non-specific interactions in this system are charge-based. One way to reduce charge-based non-specific binding is to increase the net charge of protein molecules by increasing the pH values above the pI. Accordingly, the adsorbed quantities substantially decrease at pH > pI (as shown in Figure 35 (b)-(c)). While high pH might alter the binding affinity between the TNF-α and adalimumab, negatively affecting the titer monitoring. It has been demonstrated that a high concentration of BSA can minimize nonspecific binding between the positively charged protein and the negatively charged surface by coating the surface wall and surrounding the protein analyte to the extent that it prevents interactions with the surface [213]. In this thesis, 1% BSA was added to the nanofluidic running buffer at pH 8 (TB buffer) to test its effectiveness in reducing non-specific adsorption. As shown in Figure 35 (d), the nanochannel is free of any residual protein even after running the titer monitoring for 7 days using 1% BSA-containing buffer, suggesting that 1% BSA is effective in reducing the non-specific binding.

To further evaluate how reducing non-specific binding can contribute to the tier titer monitoring, the fluorescent intensity of the centerline was monitored over time. Mixtures of fluorescently labeled TNF-α and unlabeled adalimumab (TNF-α-alexa488-adalimumab) in TB buffer (712 mM Tris, 1068 mM Boric acid) with and without 1% BSA were used.

For short-term testing, the mixtures were manually injected into the device reservoirs, and a voltage was applied to drive the mixture into the nanofilter array. The fluorescent intensity was monitored immediately after the voltage was applied to the device. Figure 36 depicts the fluorescent signal intensity collected without and with 1% BSA. The relative fluorescent intensity would continue to increase without 1% BSA due to nonspecific adsorption to the channel surface (Figure 36 (a)). With 1% BSA passivation (Figure 36 (b)), the fluorescent intensity plateaued after around 25 minutes, when the intensity signal could be collected for quantification. The long-term signal stability was also tested, as shown in Figure 36 (c), and in this test, an online sample preparation system was used to pump the sample into the device. It can be concluded that the interferences from nonspecific adsorption on the nanofluidic channels can be effectively minimized or eliminated in the running buffer with 1% BSA (TB-BSA buffer).

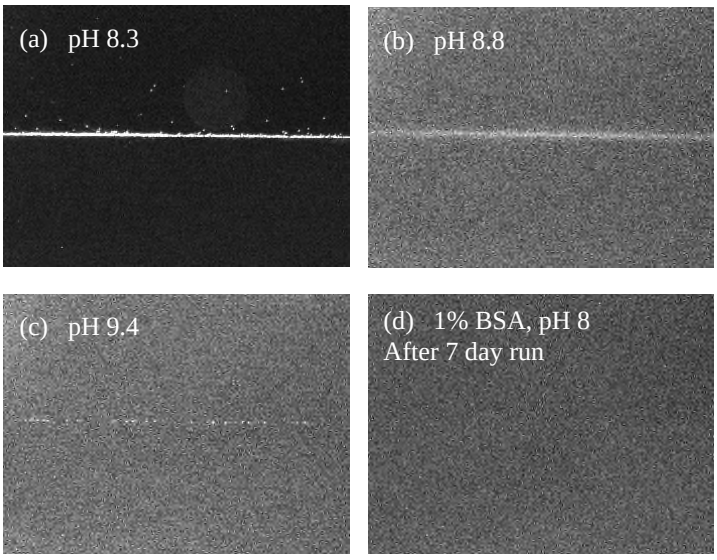

Figure 35 (a) Nanofluidic device running with NR buffer #1. Reduce nonspecific binding by (b)-(c) increasing the pH of the buffer; (d) adding 1% BSA into the buffer. All the buffers are tris and boric acid based. The pH is altered by adjusting the molar ratio between the tris base and the boric acid.

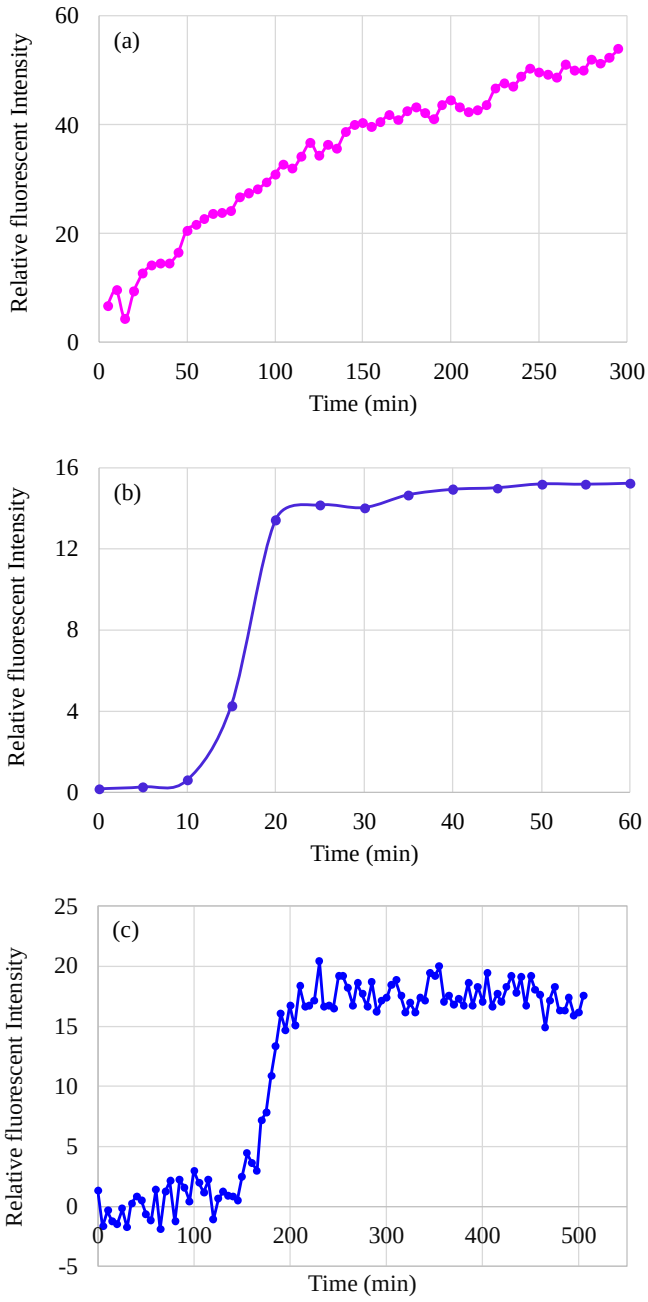

Figure 36 Fluorescent signal intensity of the centerline along the nanofluidic device running with TNF-α-alexa488-Adalimumab samples diluted in TB buffer (a) without 1% BSA; (b) with 1% BSA; (c) with 1% BSA, long-term signal stability test. To minimize device-related differences, all three tests are performed on the same device. In (a) and (b), the samples were manually injected into the reservoirs and pumped to the microchannels of the device using a syringe, whereas in (c), the sample was pumped to the device using the online sample preparation system. Monitoring began immediately after the voltage was applied to the device.

3.4 Characterizing the size separation resolution

The nanofluidic assay utilizes recombinant human TNF-α, conjugated to a fluorophore, as a selective adalimumab binder. The device relies on selectively concentrating the large molecules for titer monitoring. Therefore, the size separation resolution of the device needs to be characterized. Specifically, the device's capability to separate the Adalimumab-TNF-α complex from TNF-α must be evaluated.

The size resolution of the device was investigated using fluorescently labeled TNF-α (TNF-α-alexa488), adalimumab (Adalimumab-alexa488), and TNF-α-alexa488-Adalimumab. The hydrodynamic radii of the TNF-α, purified adalimumab, and Adalimumab-TNF-α complex were measured using dynamic light scattering (DLS, DynaPro NanoStar, Wyatt Technology, USA). The concentration of TNF-α and purified adalimumab was 1mg/mL. Adalimumab-TNF-α complex sample was obtained by mixing adalimumab (1 mg/mL) with TNF-α (1 mg/mL) at the molar ratios of 1:1, 1:2, and 1:3 before the measurement. All the samples were filtered through a 0.1 μm filter using Ultrafree™-MC Centrifugal Filters with Durapore™ Membrane (0.1 μm, MilliporeSigma™ UFC30VV25, Fisher Scientific) following the product instructions. DLS data were collected at 21 °C operating at 658 nm of laser wavelength. Samples were prepared in the nanofluidic running buffer without 1% BSA (712 mM Tris, 1068 mM Boric acid, TB buffer). 10 μL of the samples were analyzed in MicroCuvette (disposable, WNDMC, Wyatt Technology). The refractive index of the TB buffer was defined as 1.333, and the refractive index increment, dn/dc, for all samples was chosen as 0.185 mL/g, a consensus value for unmodified proteins [217]. The

hydrodynamic radii of the samples were calculated using Dynamics 7.1.2 software, using the parameters for a globular protein model.

The dynamic viscosity of the TB buffer was measured with an AR-G2 Rheometer (TA Instruments, USA) using a 40 mm plate and at a 56 μm gap. The temperature was set at 22 °C, and the shearing rate was between 1-100 s^{-1}. The viscosity is plotted against the logarithm of the shear rate, as shown in Figure 37. The viscosity was calculated by averaging over the stabilized region (Newtonian fluid), and the value is 1.678 ± 0.072 cP.

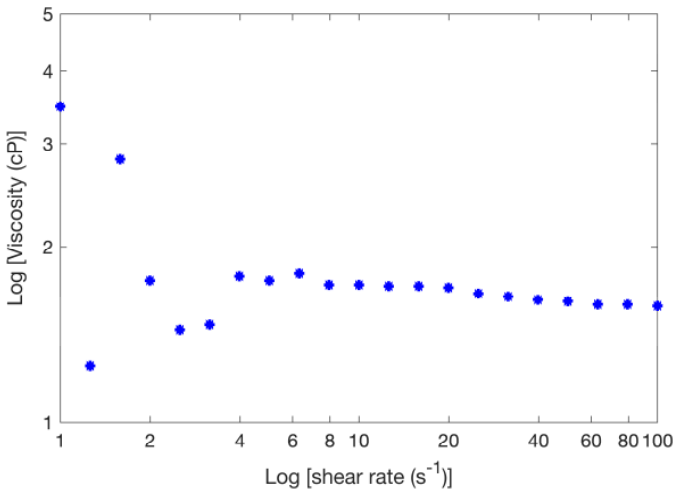

Figure 37 Log-log plot of the viscosity *vs.* shear rate of TB buffer measured with an AR-G2 Rheometer.

The hydrodynamic radii (Rh) of unbound TNF-α and adalimumab in TB buffer (nanofluidic running buffer without 1% BSA, Debye length is 0.604 nm) are 3.12 ± 0.35 nm and 5.23 ± 0.16 nm, respectively, as determined by DLS. The measured hydrodynamic radius of TNF-α confirmed the expected oligomeric state as trimeric [218]. No salting-out or isoelectric precipitation was observed in the TB buffer, and the Rh measurements suggest that there was no protein aggregation [219], [220]. The Rh of the Adalimumab-

TNF-α complex samples were estimated as 12.21 ± 1.74 nm, 11.15 ± 1.27 nm, 11.95 ± 1.49 nm, respectively, with the molar ratios between adalimumab and TNF-α at 1:1, 1:2, and 1:3.

The degree of labeling of Alexa 488 labeled TNF-α and adalimumab was 1.3 and 5.9, respectively, as analyzed by Nanodrop One. 135 nM TNF-α-alexa488, 60 nM adalimumab-alexa488, and the mixture containing 135 nM TNF-α-alexa488 and 60 nM adalimumab were used to test the size resolution of the device. The samples were manually loaded into the reservoirs of the device. A 150-volt voltage was applied at the inlet of the device, and the outlet was grounded. Images of the device were obtained 2 hours after the voltage was applied. Images of the device running the TNF-α-alexa488 samples with voltage applied for up to 12 hours were also taken to confirm that no fluorescent signal was detected. Figure 38 illustrates typical fluorescent intensity images, indicating that the device running TB-BSA buffer can differentiate samples with radii of 5.23 nm and 3.12 nm and can concentrate molecules with radii larger than 5.23 nm. The difference in the line widths in Figure 38 (b) and (c) reveals that the concentrating effect is stronger for molecules with a larger radius.

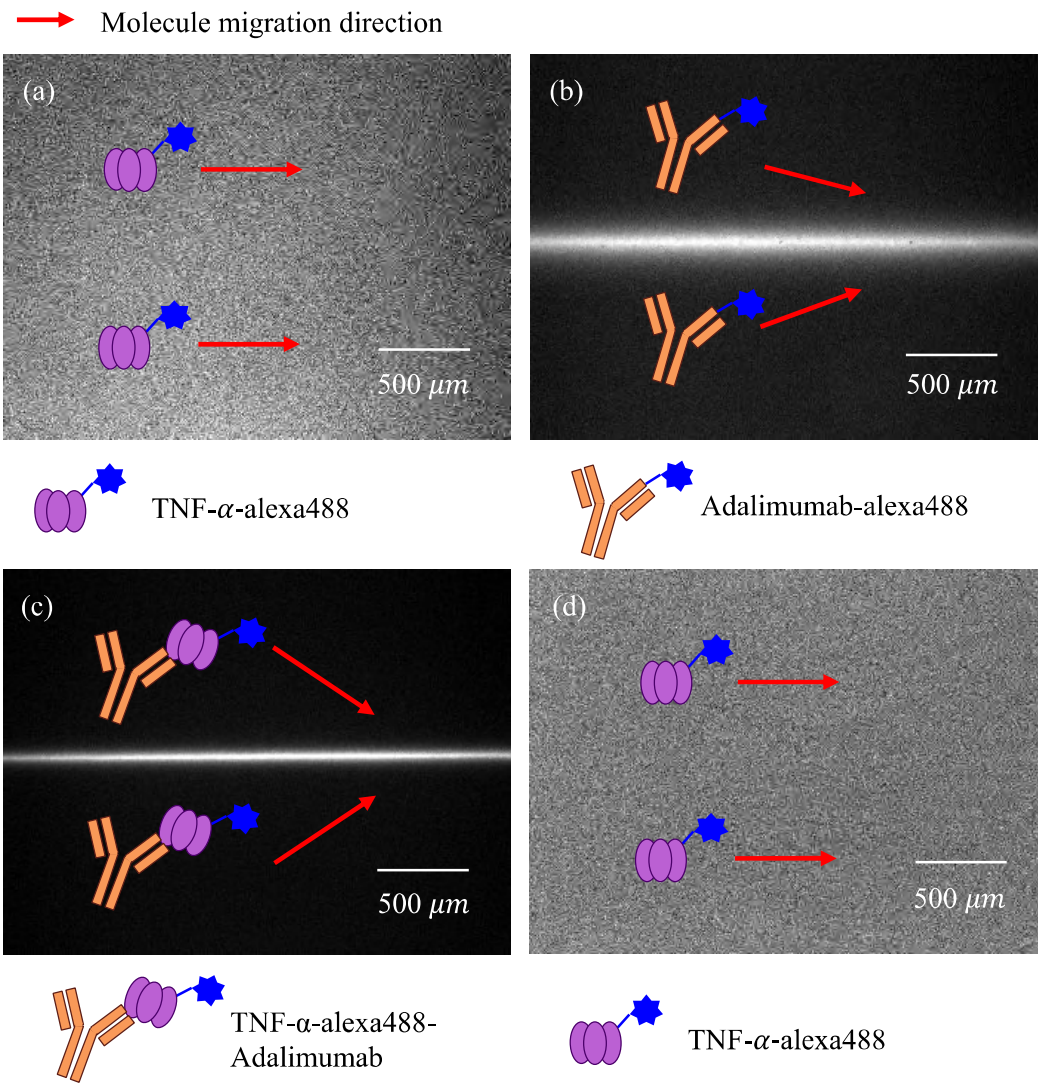

Figure 38 Fluorescent intensity images of the device operated using TB-BSA buffer, samples used to evaluate the size resolution of the system are (a) 135 nM TNF-α-alexa488, 3.12 nm radius; (b) 60 nM Adalimumab-alexa488, 5.23 nm in radius; (c) the mixture containing 135 nM TNF-α-alexa488 and 60 nM adalimumab, the complex radius is about 11.15 nm. Under this buffer condition, the device can concentrate molecules with a radius greater than 5.23 nm. Red arrows indicate the migration direction of the molecules. The deflection angle relative to the centerline of the device suggests the intensity of the concentrating effect, *i.e.*, the larger the deflection angle, the higher the concentrating effect.

3.5 Generating Standard calibration curves

The standard calibration curves were generated using a filtered crude bioreactor sample from bioreactor #2 on day 18 of the mAb production run, whose concentration was measured by an Octet RED96e biolayer interferometry system (Sartorius, USA). Eight ProA biosensors were presoaked in 1× PBS for 20 minutes before the measurements. The purified supernatant sample containing adalimumab with a titer of 250 μg/mL was diluted 2-fold in series in 1× PBS to generate 8 standard samples. The unknown supernatant sample was diluted 10-fold. A sample contact time of 2 minutes and a shaking speed of 400 RPM were used. The sensors were regenerated (10 mM glycine-HCL, pH 1.5) and neutralized (1× PBS) three times between each set of 8 samples. The samples were measured 3 times in total by repeating the process twice. The binding data were analyzed by the Octet data analysis software, and the initial binding rate of the standard samples was fitted to a four-parameter dose-response model. The response signals obtained from the standard samples were analyzed using Octet® BLI Analysis Software, and the binding rate for the initial slope of the binding curve was calculated. The measured binding rates were then plotted as a function of the concentration of the standard samples, and the data was fit into a dose-response equation, yielding a standard curve that was utilized in future quantitation of samples of unknown concentration using BLI.

The adalimumab concentration in the supernatant measured with BLI is 0.6 mg/mL. The dynamic range of the nanofluidic device is determined by the concentration of the TNF-α-alexa488 as the high concentration of adalimumab will saturate the binding curve between adalimumab and TNF-α [221]. Therefore, proper sample dilution into the nanofluidic

running buffer is required to perform adequate measurements once the TNF-α-alexa488 concentration is chosen. The supernatant sample was titrated manually to generate the device calibration samples, and 90 nM TNF-α-alexa488 was employed in the assay. The relative fluorescence intensity along the centerline of the device was monitored. Device 1 was calibrated using the sample preparation system to perform 1:1 mixing with the TNF-α-alexa488 indicator by using the same flow rate for each stream. Specifically, the nanofluidic device holder was connected to the microcentrifuge tube (Eppendorf Protein LoBind Tubes, 0030108434) holding the diluted supernatant samples, and the supernatant sample in the tube was replaced every 5 hours to simulate the online sampling of the bioreactor. For device 2, the mixing is done manually offline. The relative fluorescent intensity *vs.* adalimumab titer is shown in Figure 40 (a) and (b). The difference between the fluorescent intensities across the two devices might originate from the fabrication defects. The linearity of the standard curve was high, with R^2 values around 0.988 in both devices. The trendline generated from the calibration data can be used to calculate the titers of unknown samples based on the measured relative fluorescent intensity. Figure 40 displays the time-varying fluorescent intensity of device 1 during the simulated online run, demonstrating that the device is capable of continuously capturing the changes in fluorescent intensity originating from the titer variation. The time lag between sample replacement and signal stabilization is approximately 150 minutes, which is related to the delays in diffusion mixing (35 minutes), sample flow through the connecting tubing, and the delay in the nanofluidic device (60 minutes). Device calibration can typically be done offline, *i.e.*, by manual dilution of the supernatant sample followed by manual mixing with

TNF-α-alexa488. For online monitoring, programmable pumps can be used to adjust the flow rate, minimizing the time delay in the connecting tubing. Diffusion mixing between the supernatant sample and the buffer (online sample dilution), as well as between the supernatant sample and TNF-alexa488 (online sample mixing), can be conducted in two micromixers instead to achieve rapid mixing [188].

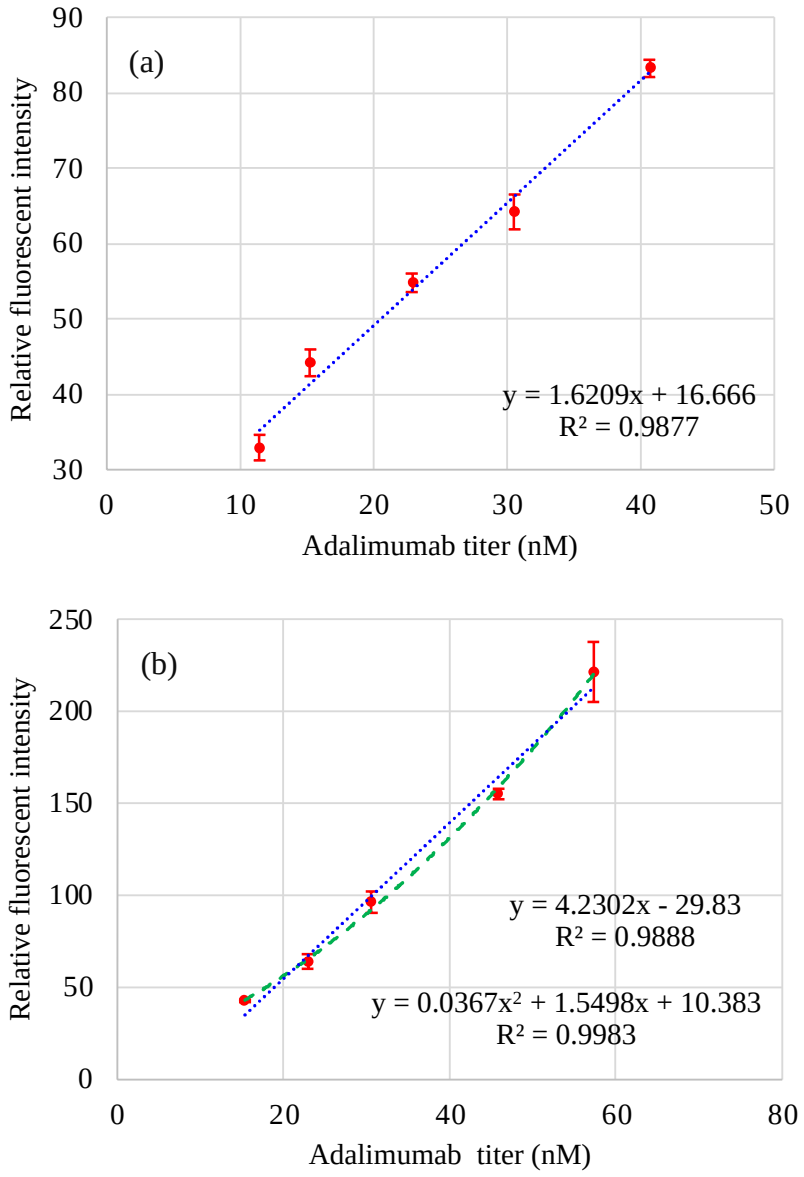

Figure 39 Device calibration with supernatant samples of known concentration. The calibration samples are titrated from the day 18 sample from bioreactor #2. Each measurement is repeated 3 times (n = 3, error bars represent standard deviation). The TNF-α-alexa488 concentration is 90 nM before mixing with the adalimumab test sample. (a) Device 1 calibration. (b) Device 2 calibration. The dotted line and dashed line represent linear and 2nd order polynomial fitting curves, respectively. The adalimumab titers in the plot are before mixing. Device 1 was calibrated online using the sample preparation system for sample mixing and pumping. Offline mixed samples were used for device 2 calibration.

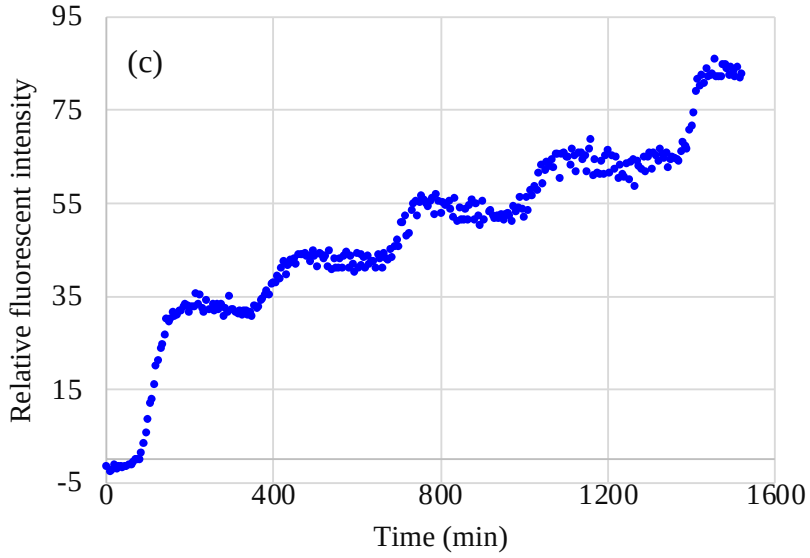

Figure 40 Time-varying relative fluorescent intensity during online calibration of device 1 using the sample preparation system for sample mixing and pumping. Offline mixed samples were used for device 2 calibration.

3.6 Continuous titer monitoring using the nanofluidic system

Supernatant samples of unknown concentrations from bioreactor #1 were diluted with TB-BSA nanofluidic running buffer. The samples were mixed with TNF-α-alexa488 at a 1:1 volume ratio controlled by the flow rate of the peristaltic pump. The titers of the unknown samples were measured using device 1 based on the relative fluorescent intensity of the centerline using the equation of the trendline in Figure 40 (a). The workflow of the continuous monitoring using the nanofluidic system is illustrated in Figure 41. The concentration of the unknown samples was later determined by BLI using the bioreactor #2 sample on day 18 as the standard (to mimic the nanofluidic calibration). Figure 42 shows the adalimumab titer (after mixing with TNF-alexa488) evaluated using the nanofluidic

device vs. the titer calculated using BLI. The correlation between BLI references and titers measured with the nanofluidic device in terms of the R^2 of the model was used to estimate the performance of the nanofluidic device. The R^2 closed to 1 was the estimation criteria. In these tests, the R^2 is equal to 0.9631, indicating that the agreement between the measurements using the two devices is high.

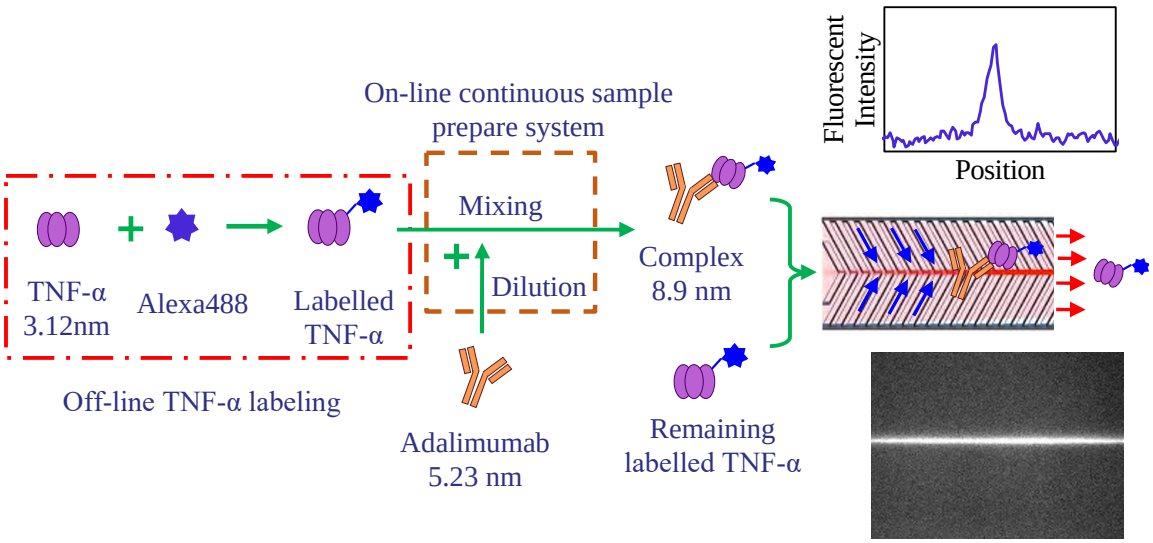

Figure 41 Workflow of using nanofluidic system for online titer monitoring. The TNF-α is labeled offline to reduce online sample preparation time and complexity. Online sample preparation includes supernatant dilution and mixing with TNF-α-alexa488. The complex is selectively concentrated along the centerline of the device and the fluorescent image is recorded.

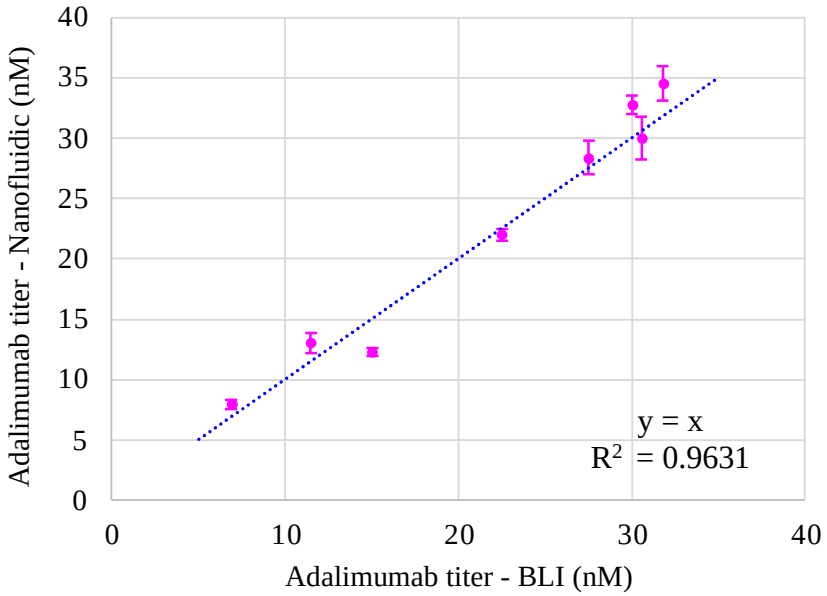

Figure 42 Samples of unknown titers measured with device 1. Testing samples were generated by diluting supernatant samples of unknown titers. The titers of the original samples were later determined by BLI. The linear model y = 1.6209x + 16.666 in Figure 40 (a) was used to calculate the titer of the diluted samples based on the measured fluorescent intensity. The titers in the plot are after mixing, and each measurement is repeated 3 times (n = 3, error bars represent standard deviation). The TNF-α-alexa488 concentration is 45 nM after being mixed with the Adalimumab test sample. To evaluate the reliability of the nanofluidic device, the results from the nanofluidic device were fitted to those from the BLI using y = x, as indicated in the blue dashed line in the figure.

In addition, root mean square error of prediction (RMSEP) and relative standard error of prediction (RSEP) values were utilized to measure the accuracy and precision of measurements in order to estimate the performance of the nanofluidic device. For the RMSEP and RSEP calculations, the following equations were used:

$$\mathrm{RMSEP} = \sqrt{\frac{\sum_{i=1}^{n}(y_{pred} - y_{ref})^2}{n}} \tag{10}$$

$$\text{RSEP} = \sqrt{\frac{\sum_{i=1}^{n}(y_{pred} - y_{ref})^2}{\sum_{i=1}^{n} {y_{ref}}^2}} \quad (11)$$

in which, y_{pred} is the titer measured using the nanofluidic device and y_{ref} is that measured using BLI, n is number of samples. A low value for these performance characteristics indicates that the devices are reliable. The unit of RMSEP is the same as the predicted titer, whereas RSEP is expressed as the percentage of the standard error of the measurements. The RMSEP associated with this measurement is 1.4510 nM within a test range of 6.88-31.77 nM, and the RSEP is 0.0782.

During real-time operation, the sample titer might fluctuate outside the calibrated range, for example, during the initial perfusion run or due to intentional adjustments of the bioreactor operation specifications. In theory, as long as the adalimumab titer is within the dynamic range of the binding curve, the nanofluidic device should be able to capture titers outside of the calibration range. To assess the capability to measure titers beyond the calibration range, a third device was calibrated using the identical supernatant sample (day 18, bioreactor #2 sample). The standard calibration curve was produced using three adalimumab samples with titers of 22.9 nM, 30 nM, and 60 nM after dilution into TB-BSA buffer. A bioreactor sample with an unknown titer (day 24 from bioreactor #2) was diluted to generate test samples (the titer was later measured using BLI). The relative fluorescence intensity acquired by the nanofluidic device was plotted against the BLI titer, as illustrated in Figure 43. The device was able to measure titers both within and outside of the calibration range. A further increase in the adalimumab titer will saturate the binding curve.

The dynamic range of the device is expected to be 0.15-1.5 fold of the TNF-α-alexa488 concentration. The dynamic range can be tuned by adjusting the TNF-α-alexa488 concentration in the solution.

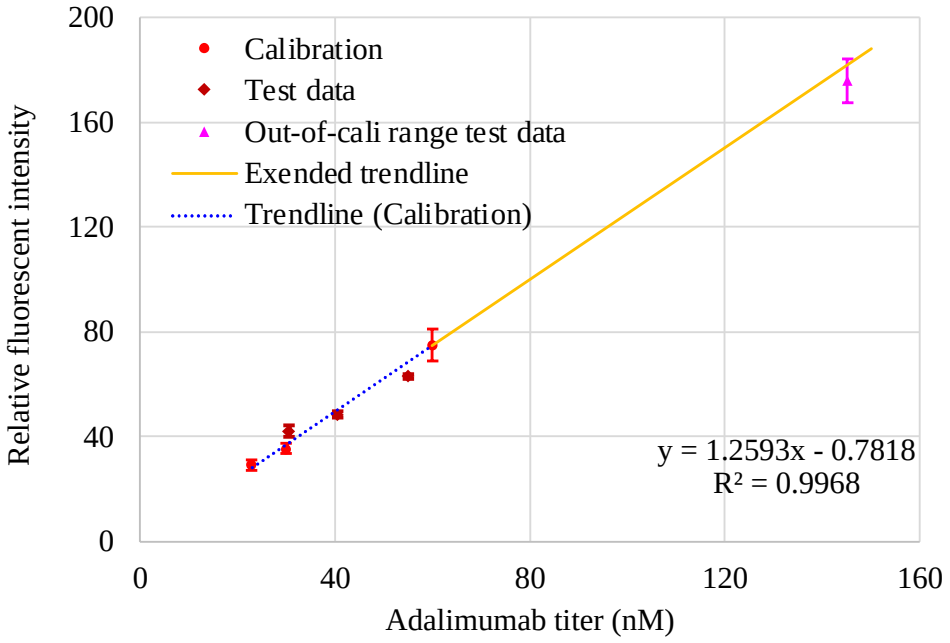

Figure 43 Device testing using supernatant samples with titers within and beyond the calibration range. Adalimumab titers in the plot are before mixing with TNF-α-alexa488 (90 nM). Out-of-calibration range sample was generated by purposefully diluting the sample with a lower dilution factor. The titers of the unknown samples before dilution were assessed with BLI after nanofluidic titer measurement. The ability to promptly and reliably quantify adalimumab titers over a wide concentration range

The ability to promptly and reliably quantify adalimumab titers over a wide concentration range in an upstream process step was further evaluated utilizing samples collected throughout the mAb production run from bioreactor #2. To simulate the actual online measurement settings, the sample preparation system was connected to the tube containing supernatant samples collected from the bioreactor, and the supernatant sample in the tube

was updated every 4 hours to mimic the online sampling of the bioreactor. The flow rate ratio between the TB-BSA buffer stream and the supernatant stream was tuned to adjust the sample dilution factor. The pre-calibrated devices 1 and 2 were used to measure the titers. Day 4 samples were diluted 10-fold, and day 5 samples were diluted 20-fold. Due to the high fluorescent intensity of the day 5 sample, the rest of the samples were diluted 50-fold to avoid oversaturating the binding curve. Figure 44 depicts the titers measured with the nanofluidic devices and their ratio over BLI readings (relative adalimumab titer). Figure 44 (a) depicts the results obtained from device 2 using linear and 2nd-order polynomial models, respectively, and Figure 44 (b) compares the titers measured with devices 1 and 2. For device 2, the linear model underestimates the titer when compared to the 2nd-order polynomial model, which revealed a higher degree of correlation with BLI data (R^2 = 0.9926, RMSEP = 10.8455 μg/mL in the range of 57.99-327.98 μg/mL, RSEP = 0.0277). Titers accessed with device 1 demonstrated a greater correlation with the BLI measurements. Despite the discrepancies, both devices demonstrated a high degree of correlation using the linear models with R^2 = 0.9866 and 0.9562, respectively, RMSEP = 24.7998 μg/mL and 14.6964 μg/mL (test range is 57.99-327.98 μg/mL), respectively; and RSEP = 0.0633 and 0.0375, respectively.

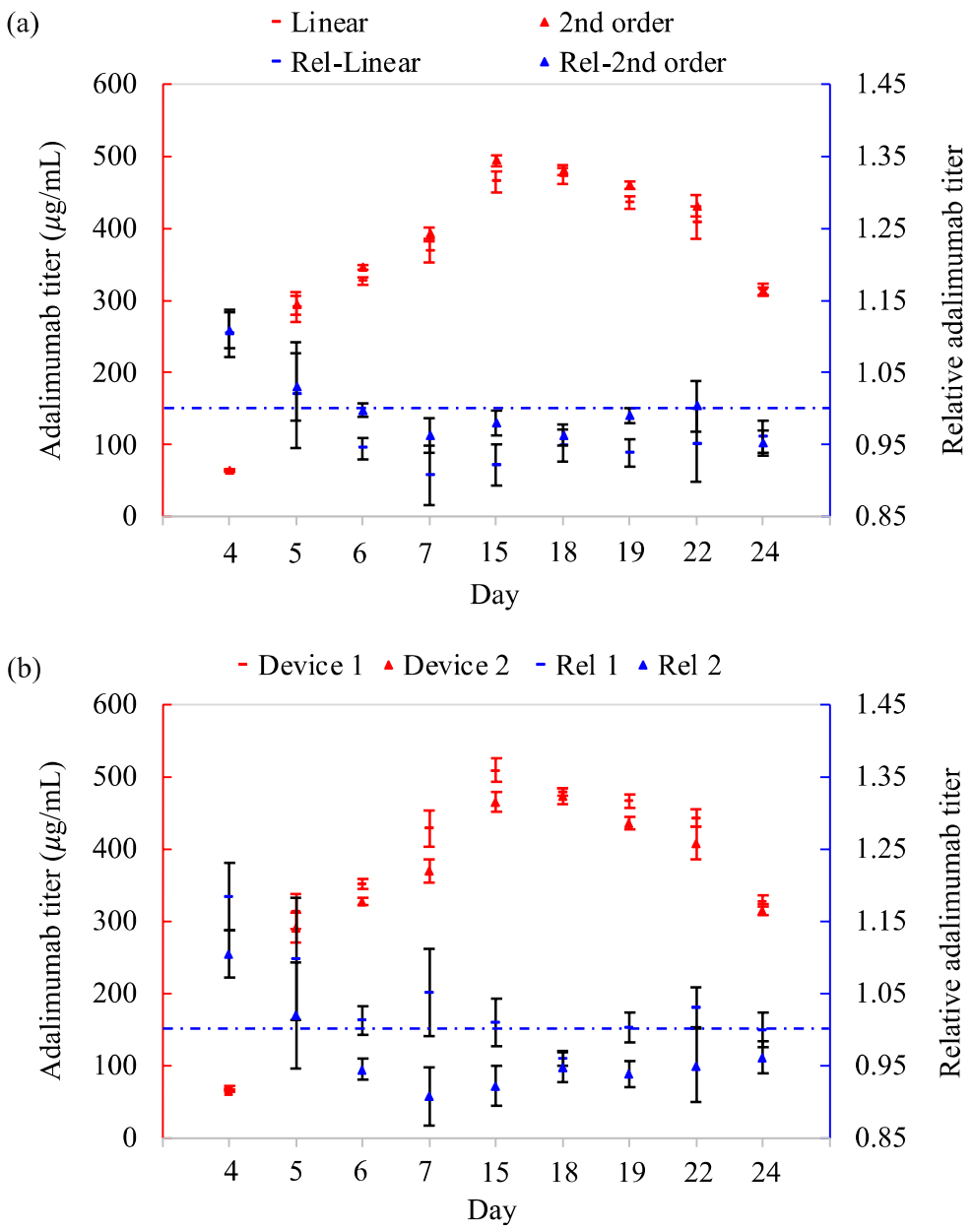

Figure 44 Simulated online monitoring of supernatant samples from bioreactor #2. The supernatant sample in the sample preparation system was replaced every 4 hours to simulate online monitoring. The sample from day 4 was measured at 10-fold dilution, the sample from day 5 at 20-fold dilution, and the remaining samples at 50-fold dilution. Relative adalimumab titer is the ratio of the titer measured using the nanofluidic system to that measured using the BLI. (a) Adalimumab titer measured using pre-calibrated device 2 with the titer calculated using the linear and 2nd-order polynomial models in Figure 39 (b). (b) Adalimumab titer measured with pre-calibrated devices 1 and 2 with the titer calculated using the linear models in Figure 39. All samples were measured in triplicate.

CHAPTER 4. CONCLUSION AND FUTURE

Efficient and cost-effective biologics production requires the ability to monitor and control the production process accurately. Guidelines concerning PATs released by the U.S. FDA initiated a large interest in the development and implementation of technologies for near real-time or real-time monitoring of KPIs and CQAs in bioproduction. For most of the decade, AbbVie's Humira (adalimumab) has been the most profitable drug in the world. It took a global pandemic to knock the injectable biologic for inflammatory diseases into second place in 2021, but it still reached $20.7 billion in sales, topped only by Pfizer's vaccine for COVID-19. In 2018, Humira ranked second on a list of the 25 best-selling drugs of all time, trailing only the cholesterol drug Lipitor (atorvastatin), which was launched in 1992. As biosimilars that reference the blockbuster originator will usher in a new era for the adalimumab market, 2023 will signal the official start of the adalimumab biosimilar market in the United States. Currently, there are 7 FDA-approved adalimumab biosimilars waiting to enter the US market, all of which are currently available in the European Union; most are also accessible in Canada and the United Kingdom. Possibilities to monitor the titers of adalimumab and its biosimilars during biomanufacturing are central to optimizing process conditions and achieving high yields as well as consistent and high product quality. The titer is naturally an important KPI in the production of mAbs. Current PATs either require complex equipment or necessitate sample handling, including purification, which complicates their implementation in bioproduction.

The study in this thesis suggests that the nanofluidic mAb-target binding assay is a promising technology for direct (no sample pretreatment) assessment of adalimumab titer in CHO cell supernatant with nanomolar sensitivity. The developed nanofluidic assay employs a selective anti-Adalimumab protein as the indicator, allowing for accurate determination of the adalimumab titer without necessitating any prior purification. This illustrates that the nanofluidic system is highly tolerant of the complex sample matrix, necessitating little or no sample pretreatment. Adalimumab quantification results from crude cell culture supernatants were highly comparable to conventional BLI methods. Furthermore, by altering the indicator concentration, the dynamic detection range may be modified. While all measurements in this work were carried out under simulated online settings, the continuous sample preparation system can be connected to a computer-controlled sampling system to perform on-demand sampling. Since the device is resistant to mechanical and chemical degradation, it can operate indefinitely. The device is suited for on-site (point-of-care) biologics monitoring due to its short operational time (less than one hour) and small sample volume. Other anti-Adalimumab-specific ligands, *e.g.*, protein A and affibody, are also applicable for adalimumab concentration measurement using nanofluidic devices. But, with TNF-α as the indicator, other than providing titer information of the protein in the complex sample directly form the bioreactor, the in-solution ligand binding technology used in the nanofluidic system can reveal the functionality of the protein product (CQA) without the need for detailed structural analysis (*e.g.*, glycoform).

With TNF-α as the indicator, we can utilize the system to monitor other TNF-α inhibitors such as etanercept, infliximab, golimumab, and certolizumab [222] with minimum modifications in the device operating settings. This protocol can be extended to determine the concentration of other biomolecules (analytes) by choosing a proper indicator that binds specifically to the analyte of interest. The requirements for a successful assay are: the indicator can be fluorescently labeled; the hydrodynamic radii difference between the binding complex and the indicator meets the size separation resolution of the device; the buffer is compatible with the analyte and the indicator and ensures relatively high binding affinity. The size resolution of the device can be optimized for a particular assay by modifying the buffer composition and redesigning the dimensions of the nanochannels. It is safe to say that this nanofluidic system can be applied to quantifying a wide range of analytes and probing their activity as well.

The sample preparation of the existing system can be streamlined into a microfluidic chip that conducts effective sample dilution and mixing while also enabling direct fluid transfer to the nanofluidic chip. Moreover, the miniaturization of light sources, detectors, and signal read-out components may assist the comprehensive integration of entire analytical processes, resulting in a compact and portable analytical device that can be connected at every stage of the biomanufacturing line [223]. Thus, we anticipate that online monitoring using nanofluidic systems will facilitate the development and production of therapeutic proteins.

APPENDIX

A. 1 Fabrication of nanofluidic device

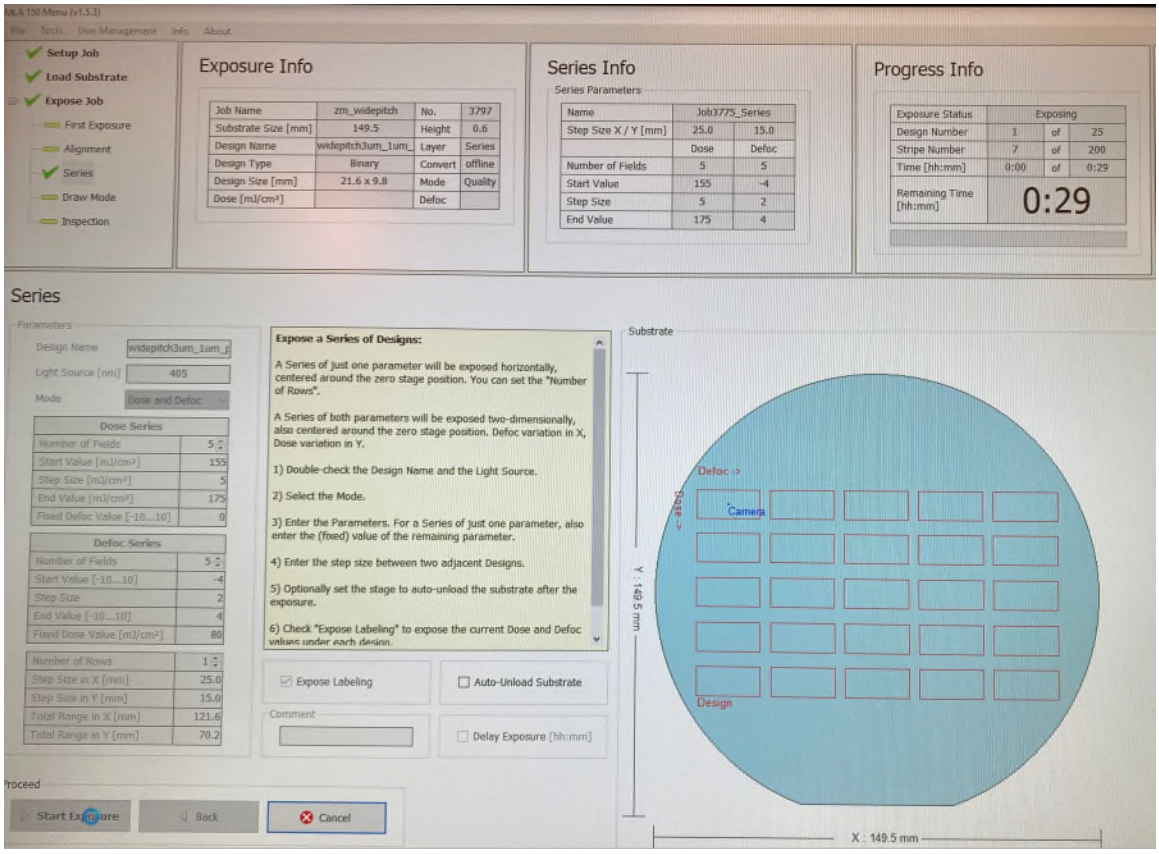

Figure A 1 Dose and defoc testing matrix on MLA150.

(a)

Job recipe	SI
Lot	zml2
Description	Etch - Silicon

UM	Name	Value	Unit
1	Etch time	125	sec
2	Pressure	0.6	Pa
3	ICP	100	W
4	Bias	50	W
9	SF6	6	sccm
10	Ar	20	sccm

(b)

Job recipe	SIO2-SEL
Lot	zm
Description	Etch - Silicon Dioxide w/higher selectivity to PR

UM	Name	Value	Unit
1	Etch time	177	sec
2	Pressure	2	Pa
3	ICP	100	W
4	BIAS	50	W
7	CHF3	30	sccm
8	CF4	30	sccm
10	Ar	0	sccm

(c)

Job recipe	SIO2DEEP
Lot	zm
Description	Etch -deep Silicon Dioxide cycle w/cooldown steps

UM	Name	Value	Unit
1	Etch time	190	sec
2	Pressure	2	Pa
3	ICP	100	W
4	BIAS	50	W
6	H2	0	sccm
7	CHF3	30	sccm
8	CF4	30	sccm
13	cooldown time	80	sec
14	# cycles	18	loops

Figure A 2 ICP RIE etching recipe on SAMCO F. (a) Si etching; (b) High selectivity SiO_2 etching; (c) Deep silicon dioxide etching with periodic cooling.

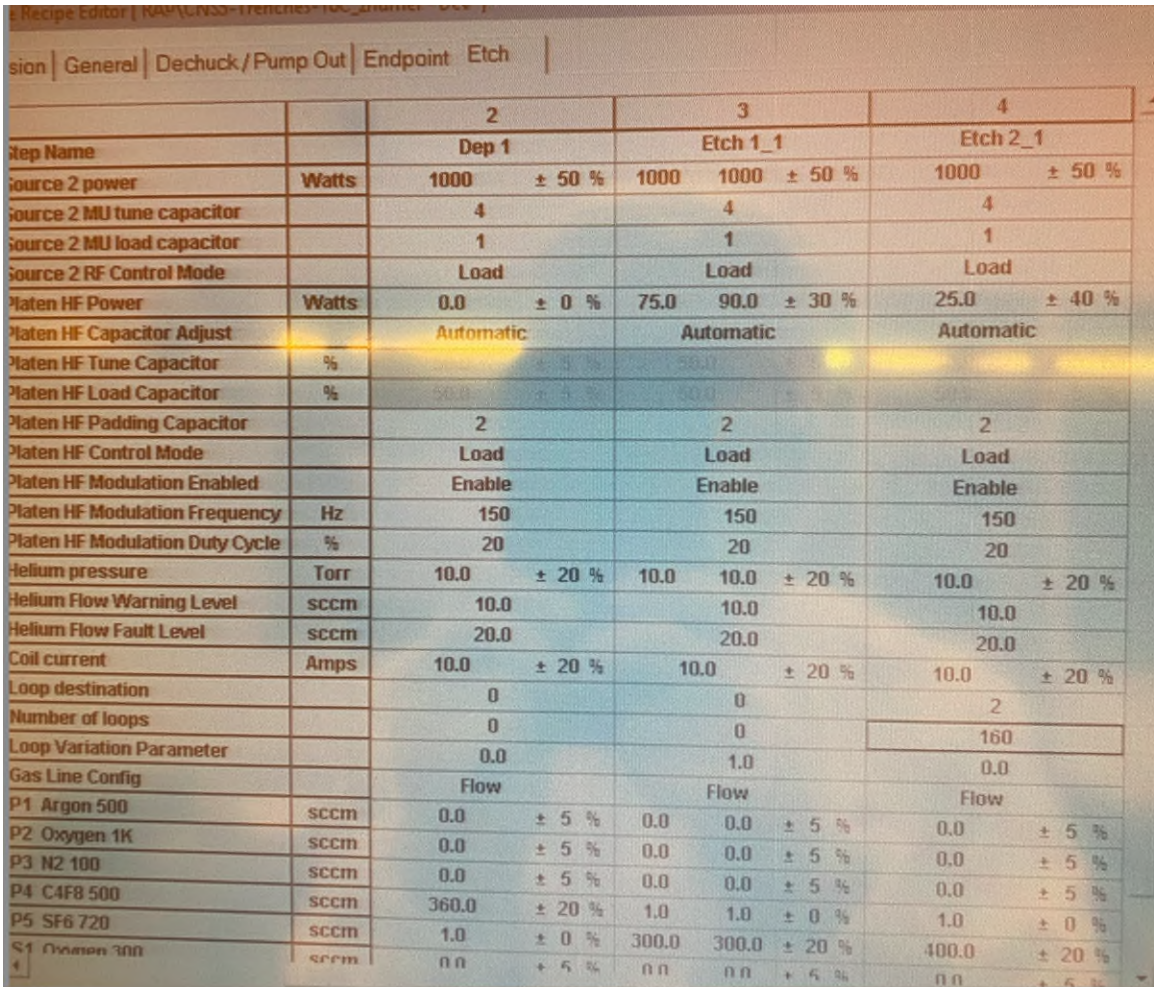

sion | General | Dechuck / Pump Out | Endpoint | Etch

		2	3	4
tep Name		Dep 1	Etch 1_1	Etch 2_1
ource 2 power	Watts	1000 ± 50 %	1000 1000 ± 50 %	1000 ± 50 %
ource 2 MU tune capacitor		4	4	4
ource 2 MU load capacitor		1	1	1
ource 2 RF Control Mode		Load	Load	Load
laten HF Power	Watts	0.0 ± 0 %	75.0 90.0 ± 30 %	25.0 ± 40 %
laten HF Capacitor Adjust		Automatic	Automatic	Automatic
laten HF Tune Capacitor	%			
laten HF Load Capacitor	%			
laten HF Padding Capacitor		2	2	2
laten HF Control Mode		Load	Load	Load
laten HF Modulation Enabled		Enable	Enable	Enable
laten HF Modulation Frequency	Hz	150	150	150
laten HF Modulation Duty Cycle	%	20	20	20
elium pressure	Torr	10.0 ± 20 %	10.0 10.0 ± 20 %	10.0 ± 20 %
elium Flow Warning Level	sccm	10.0	10.0	10.0
elium Flow Fault Level	sccm	20.0	20.0	20.0
oil current	Amps	10.0 ± 20 %	10.0 ± 20 %	10.0 ± 20 %
oop destination		0	0	2
umber of loops		0	0	160
oop Variation Parameter		0.0	1.0	0.0
as Line Config		Flow	Flow	Flow
P1 Argon 500	sccm	0.0 ± 5 %	0.0 0.0 ± 5 %	0.0 ± 5 %
P2 Oxygen 1K	sccm	0.0 ± 5 %	0.0 0.0 ± 5 %	0.0 ± 5 %
P3 N2 100	sccm	0.0 ± 5 %	0.0 0.0 ± 5 %	0.0 ± 5 %
P4 C4F8 500	sccm	360.0 ± 20 %	1.0 1.0 ± 0 %	1.0 ± 0 %
P5 SF6 720	sccm	1.0 ± 0 %	300.0 300.0 ± 20 %	400.0 ± 20 %
S1 Oxygen 300	sccm	0.0 ± 5 %	0.0 0.0 ± 5 %	0.0 ± 5 %

Figure A 3 DRIE etching recipe to etch the grooves on the silicon carrier wafer.

UM	Name	Value	Unit
1	Etch time	30	sec
2	Pressure	4	Pa
3	ICP	600	W
4	BIAS	12	W
7	CHF3	0	sccm
8	CF4	0	sccm
10	Ar	50	sccm

Figure A 4 Surface activation before bonding using Argon ICP-RIE plasma.

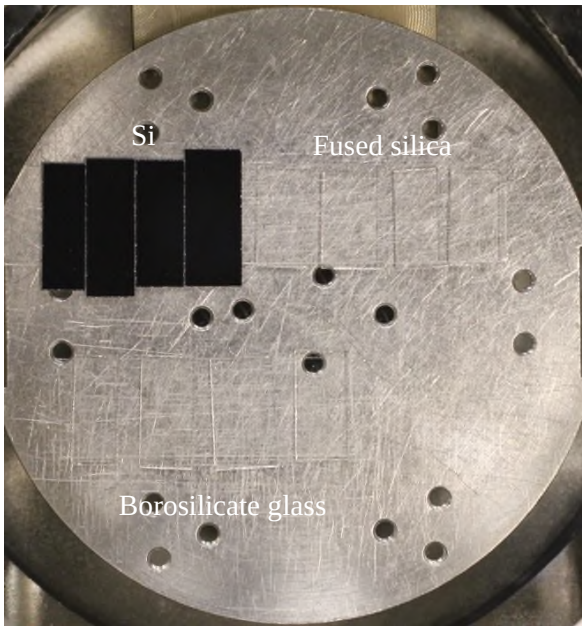

Figure A 5 Samples of different material including silicon, fused silica and borosilicate glass analyzed using XPS to compare the effectiveness of different surface activation. There are four samples for each material, each sample underwent different surface treatment, *i.e.*, no treatment, 30 minutes soaking in NH_4OH, 30s Argon plasma ICP RIE + quick DI water dip, 30 minutes soaking in NH_4OH+30s Argon plasma ICP RIE + quick DI water dip.

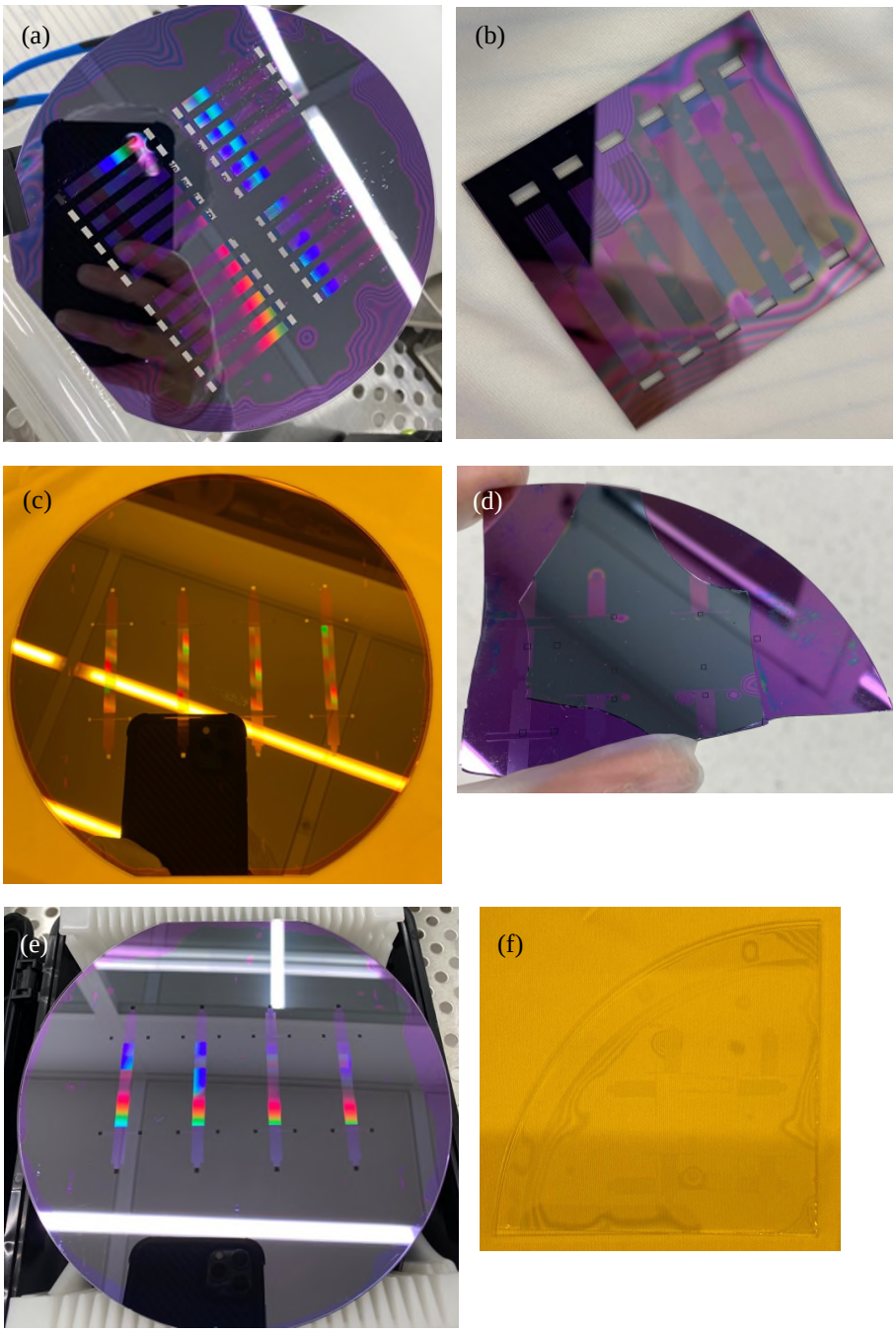

Figure A 6 Optical images of 6 inch wafers or pieces after bonding. (a) Fusion bonding of wafers with large bow and (b) the bond pair delaminated after die saw into individual device. (c) Anodic bonding of wafers with large bow using voltage ramping scheme, and (b) cleaving that occurred during blade insertion due to the high bonding strength. Fusion bonding of (e) borosilicate glass and silicon wafers with 500 nm thermal oxide; (f) fused silica substrate after die saw.

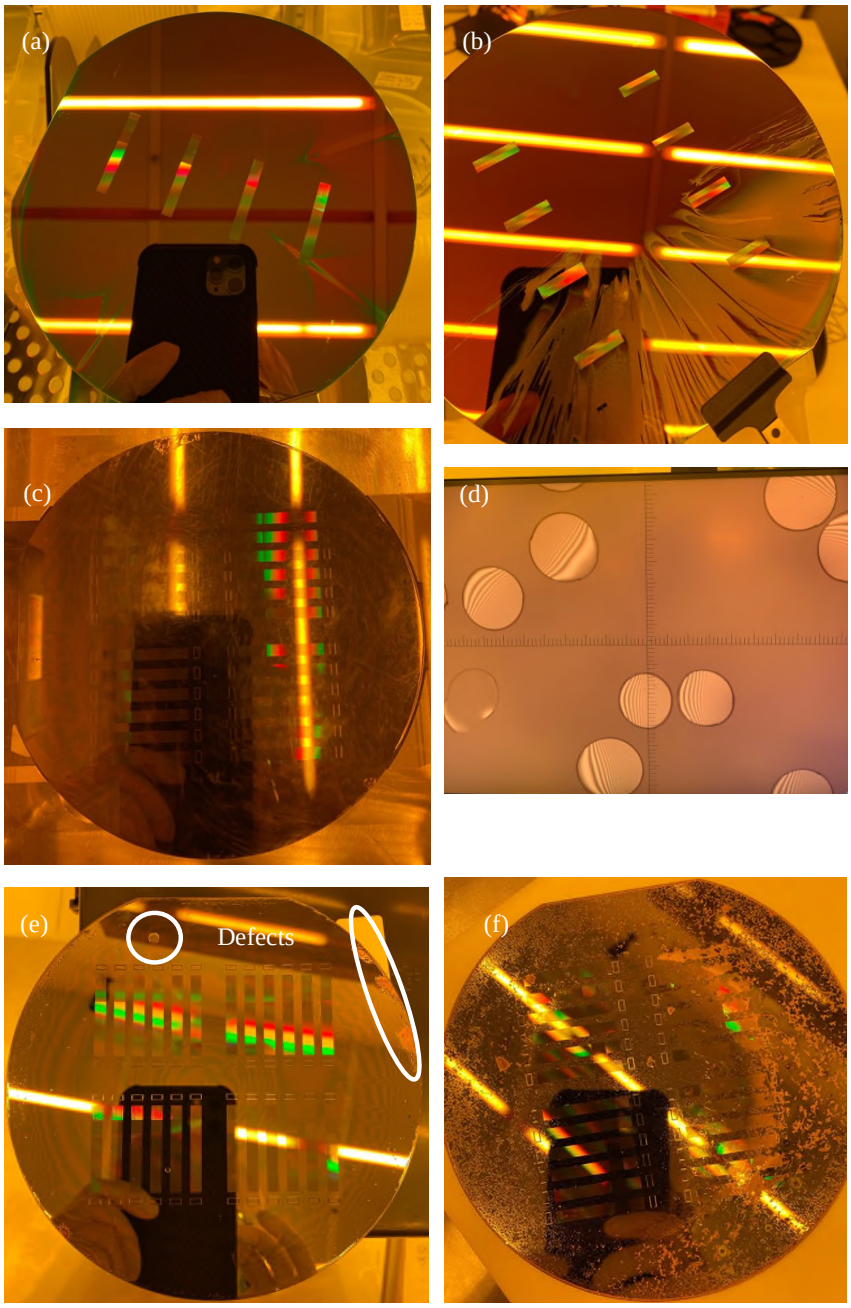

Figure A 7 Optical images of 6 common defects mentioned in the main text. (a) Particles on the wafer cause nonuniform in photoresist coating; (b) Ptrack develop recipe not setup properly; (c) Developer Fusion bonding of wafers with large bow and (b) the bond pair delaminated after die saw into individual device. (c) Anodic bonding of wafers with large bow using voltage ramping scheme, and (b) cleaving that occurred during blade insertion due to the high bonding strength. Fusion bonding of (e) borosilicate glass and silicon wafers with 500 nm thermal oxide; (f) fused silica substrate.

REFERENCE

[1] ‘Biopharmaceuticals Market by Product and by Application - Global Opportunity Analysis and Industry Forecast 2022-2030’. Accessed: Feb. 28, 2023. [Online]. Available: https://www.researchandmarkets.com/reports/5529485/biopharmaceuticals-market-by-product-and-by

[2] G. Walsh, ‘Biopharmaceutical benchmarks 2014’, *Nat Biotechnol*, vol. 32, no. 10, pp. 992–1000, 2014, doi: 10.1038/nbt.3040.

[3] G. Walsh, ‘Biopharmaceutical benchmarks 2018’, *Nat Biotechnol*, vol. 36, no. 12, pp. 1136–1145, 2018, doi: 10.1038/nbt.4305.

[4] R. M. Lu *et al.*, ‘Development of therapeutic antibodies for the treatment of diseases’, *Journal of Biomedical Science 2020 27:1*, vol. 27, no. 1, pp. 1–30, Jan. 2020, doi: 10.1186/S12929-019-0592-Z.

[5] ‘Monoclonal Antibodies (MAbS) Market Size 2022 And Growth Analysis’. https://www.thebusinessresearchcompany.com/report/monoclonal-antibodies-global-market-report (accessed Sep. 15, 2022).

[6] R. Patil and J. Walther, ‘Continuous manufacturing of recombinant therapeutic proteins: Upstream and downstream technologies’, in *Advances in Biochemical*

Engineering/Biotechnology, vol. 165, 2018, pp. 277–322. doi: 10.1007/10_2016_58.

[7] F. Li, N. Vijayasankaran, A. Shen, R. Kiss, and A. Amanullah, ‘Cell culture processes for monoclonal antibody production’, *MAbs*, vol. 2, no. 5, pp. 466–479, Sep. 2010, doi: 10.4161/MABS.2.5.12720.

[8] A. Mahé, A. Martiné, S. Fagète, and P. A. Girod, ‘Exploring the limits of conventional small-scale CHO fed-batch for accelerated on demand monoclonal antibody production’, *Bioprocess Biosyst Eng*, vol. 45, no. 2, pp. 297–307, Feb. 2022, doi: 10.1007/S00449-021-02657-W.

[9] S. Chatterjee, ‘FDA Perspective on Continuous Manufacturing’, *FDA*, 2012. https://www.fda.gov/media/85366/download%0Ahttps://www.fda.gov/downloads/AboutFDA/CentersOffices/OfficeofMedicalProductsandTobacco/CDER/UCM341197.pdf (accessed Mar. 23, 2020).

[10] R. Godawat, K. Konstantinov, M. Rohani, and V. Warikoo, ‘End-to-end integrated fully continuous production of recombinant monoclonal antibodies’, *J Biotechnol*, vol. 213, pp. 13–19, 2015, doi: 10.1016/j.jbiotec.2015.06.393.

[11] A. L. Zydney, ‘Continuous downstream processing for high value biological products: A Review’, *Biotechnol Bioeng*, vol. 113, no. 3, pp. 465–475, Mar. 2016, doi: 10.1002/bit.25695.

[12] K. B. Konstantinov and C. L. Cooney, *White paper on continuous bioprocessing May 20-21, 2014 continuous manufacturing symposium*, vol. 104, no. 3. John Wiley and Sons Inc., 2015, pp. 813–820. doi: 10.1002/jps.24268.

[13] FDA, ‘Guidance for Industry PAT - A Framework for Innovative Pharmaceutical Development, manufacturing, and Quality Assurance’, 2004. Accessed: Sep. 14, 2022. [Online]. Available: https://www.fda.gov/media/71012/download

[14] FDA, ‘Guidance for Industry Q8(R2) Pharmaceutical Development’, 2009. Accessed: Feb. 23, 2023. [Online]. Available: http://www.fda.gov/Drugs/GuidanceComplianceRegulatoryInformation/Guidances/default.htm

[15] A. S. Rathore, R. Bhambure, and V. Ghare, ‘Process analytical technology (PAT) for biopharmaceutical products’, *Anal Bioanal Chem*, vol. 398, no. 1, pp. 137–154, 2010, doi: 10.1007/s00216-010-3781-x.

[16] M. Jiang *et al.*, ‘Opportunities and challenges of real-time release testing in biopharmaceutical manufacturing’, *Biotechnol Bioeng*, vol. 114, no. 11, pp. 2445–2456, 2017, doi: 10.1002/bit.26383.

[17] Hanna Jankevics Jones, ‘The Challenges Of Applying QbD In Biopharma Development’, *Life Science Leader*, 2016. https://www.lifescienceleader.com/doc/the-challenges-of-applying-qbd-in-biopharma-development-0001

[18] O. Yang, M. Qadan, and M. Ierapetritou, ‘Economic Analysis of Batch and Continuous Biopharmaceutical Antibody Production: a Review’, *J Pharm Innov*, vol. 15, no. 1, pp. 182–200, 2020, doi: 10.1007/s12247-018-09370-4.

[19] A. L. Zydney, ‘Perspectives on integrated continuous bioprocessing - opportunities and challenges’, *Curr Opin Chem Eng*, vol. 10, pp. 8–13, 2015, doi: 10.1016/j.coche.2015.07.005.

[20] J. Hummel *et al.*, ‘Modeling the Downstream Processing of Monoclonal Antibodies Reveals Cost Advantages for Continuous Methods for a Broad Range of Manufacturing Scales’, *Biotechnol J*, vol. 14, no. 2, p. 1700665, Feb. 2019, doi: 10.1002/biot.201700665.

[21] J. Walther, R. Godawat, C. Hwang, Y. Abe, A. Sinclair, and K. Konstantinov, ‘The business impact of an integrated continuous biomanufacturing platform for recombinant protein production’, *J Biotechnol*, vol. 213, pp. 3–12, Nov. 2015, doi: 10.1016/j.jbiotec.2015.05.010.

[22] J. K. Eggersgluess, M. Richter, M. Dieterle, and J. Strube, ‘Multi-stage aqueous two-phase extraction for the purification of monoclonal antibodies’, *Chem Eng Technol*, vol. 37, no. 4, pp. 675–682, Apr. 2014, doi: 10.1002/ceat.201300604.

[23] FDA, ‘Q5A Viral Safety Evaluation of Biotechnology Products Derived From Cell Lines of Human or Animal Origin’, 1998.

[24] B. Somasundaram, K. Pleitt, E. Shave, K. Baker, and L. H. L. Lua, ‘Progression of continuous downstream processing of monoclonal antibodies: Current trends and challenges’, *Biotechnol Bioeng*, vol. 115, no. 12, pp. 2893–2907, Dec. 2018, doi: 10.1002/bit.26812.

[25] A. Jungbauer, ‘Continuous downstream processing of biopharmaceuticals’, *Trends Biotechnol*, vol. 31, no. 8, pp. 479–492, Aug. 2013, doi: 10.1016/j.tibtech.2013.05.011.

[26] R. Godawat, K. Brower, S. Jain, K. Konstantinov, F. Riske, and V. Warikoo, ‘Periodic counter-current chromatography - design and operational considerations for integrated and continuous purification of proteins’, *Biotechnol J*, vol. 7, no. 12, pp. 1496–1508, Dec. 2012, doi: 10.1002/biot.201200068.

[27] L. Arnold, K. Lee, J. Rucker-Pezzini, and J. H. Lee, ‘Implementation of Fully Integrated Continuous Antibody Processing: Effects on Productivity and COGm’, *Biotechnol J*, vol. 14, no. 2, p. 1800061, Feb. 2019, doi: 10.1002/biot.201800061.

[28] Kornecki *et al.*, ‘Accelerating Biomanufacturing by Modeling of Continuous Bioprocessing—Piloting Case Study of Monoclonal Antibody Manufacturing’, *Processes*, vol. 7, no. 8, p. 495, Aug. 2019, doi: 10.3390/pr7080495.

[29] O. Yang, S. Prabhu, and M. Ierapetritou, ‘Comparison between Batch and Continuous Monoclonal Antibody Production and Economic Analysis’, *Ind Eng*

Chem Res, vol. 58, no. 15, pp. 5851–5863, Apr. 2019, doi: 10.1021/acs.iecr.8b04717.

[30] A. L. Cataldo, D. Burgstaller, G. Hribar, A. Jungbauer, and P. Satzer, 'Economics and ecology: Modelling of continuous primary recovery and capture scenarios for recombinant antibody production', *J Biotechnol*, vol. 308, pp. 87–95, Jan. 2020, doi: 10.1016/j.jbiotec.2019.12.001.

[31] D. J. Karst, F. Steinebach, and M. Morbidelli, 'Continuous integrated manufacturing of therapeutic proteins', *Curr Opin Biotechnol*, vol. 53, pp. 76–84, Oct. 2018, doi: 10.1016/j.copbio.2017.12.015.

[32] A. S. Tait, C. E. M. Hogwood, C. M. Smales, and D. G. Bracewell, 'Host cell protein dynamics in the supernatant of a mAb producing CHO cell line', *Biotechnol Bioeng*, vol. 109, no. 4, pp. 971–982, Apr. 2012, doi: 10.1002/bit.24383.

[33] L. R. Castilho and R. A. Medronho, 'Cell retention devices for suspended-cell perfusion cultures.', *Adv Biochem Eng Biotechnol*, vol. 74, pp. 129–169, 2002, doi: 10.1007/3-540-45736-4_7/COVER.

[34] T. Kwon, R. Yao, J. F. P. Hamel, and J. Han, 'Continuous removal of small nonviable suspended mammalian cells and debris from bioreactors using inertial microfluidics', *Lab Chip*, vol. 18, no. 18, pp. 2826–2837, Sep. 2018, doi: 10.1039/c8lc00250a.

[35] A. C. Fisher, M. H. Kamga, C. Agarabi, K. Brorson, S. L. Lee, and S. Yoon, ‘The Current Scientific and Regulatory Landscape in Advancing Integrated Continuous Biopharmaceutical Manufacturing’, *Trends Biotechnol*, vol. 37, no. 3, pp. 253–267, Mar. 2019, doi: 10.1016/j.tibtech.2018.08.008.

[36] M. F. Clincke, C. Mölleryd, Y. Zhang, E. Lindskog, K. Walsh, and V. Chotteau, ‘Very high density of CHO cells in perfusion by ATF or TFF in WAVE bioreactor™: Part I: Effect of the cell density on the process’, *Biotechnol Prog*, vol. 29, no. 3, pp. 754–767, May 2013, doi: 10.1002/btpr.1704.

[37] R. Pörtner, ‘Bioreactors for Mammalian Cells’, in *Animal Cell Culture*, M. Al-Rubeai, Ed. Springer, Cham, 2015, pp. 89–135. doi: 10.1007/978-3-319-10320-4_4.

[38] J. Walther *et al.*, ‘Perfusion Cell Culture Decreases Process and Product Heterogeneity in a Head-to-Head Comparison With Fed-Batch’, *Biotechnol J*, vol. 14, no. 2, p. 1700733, Feb. 2019, doi: 10.1002/biot.201700733.

[39] M. Gagnon, S. Nagre, W. Wang, J. Coffman, and G. W. Hiller, ‘Novel, linked bioreactor system for continuous production of biologics’, *Biotechnol Bioeng*, vol. 116, no. 8, pp. 1946–1958, Aug. 2019, doi: 10.1002/bit.26985.

[40] D. J. Karst *et al.*, ‘Intracellular CHO Cell Metabolite Profiling Reveals Steady-State Dependent Metabolic Fingerprints in Perfusion Culture’, *Biotechnol Prog*, vol. 33, no. 4, pp. 879–890, Jul. 2017, doi: 10.1002/btpr.2421.

[41] T. K. Villiger, E. Scibona, M. Stettler, H. Broly, M. Morbidelli, and M. Soos, ‘Controlling the time evolution of mAb N-linked glycosylation - Part II: Model-based predictions’, *Biotechnol Prog*, vol. 32, no. 5, pp. 1135–1148, Sep. 2016, doi: 10.1002/btpr.2315.

[42] D. J. Karst *et al.*, ‘Modulation and modeling of monoclonal antibody N-linked glycosylation in mammalian cell perfusion reactors’, *Biotechnol Bioeng*, vol. 114, no. 9, pp. 1978–1990, Sep. 2017, doi: 10.1002/bit.26315.

[43] T. Ryll, G. Dutina, A. Reyes, J. Gunson, L. Krummen, and T. Etcheverry, ‘Performance of small-scale CHO perfusion cultures using an acoustic cell filtration device for cell retention: Characterization of separation efficiency and impact of perfusion on product quality’, *Biotechnol Bioeng*, vol. 69, no. 4, pp. 440–449, Aug. 2000, doi: 10.1002/1097-0290(20000820)69:4<440::AID-BIT10>3.0.CO;2-0.

[44] M. C. F. Dalm, S. M. R. Cuijten, W. M. J. Van Grunsven, J. Tramper, and D. E. Martens, ‘Effect of feed and bleed rate on hybridoma cells in an acoustic perfusion bioreactor: Part I. Cell density, viability, and cell-cycle distribution’, *Biotechnol Bioeng*, vol. 88, no. 5, pp. 547–557, 2004, doi: 10.1002/bit.20287.

[45] I. Z. Shirgaonkar, S. Lanthier, and A. Kamen, ‘Acoustic cell filter: A proven cell retention technology for perfusion of animal cell cultures’, *Biotechnol Adv*, vol. 22, no. 6, pp. 433–444, Jul. 2004, doi: 10.1016/j.biotechadv.2004.03.003.

[46] N. Singh, A. Arunkumar, S. Chollangi, Z. G. Tan, M. Borys, and Z. J. Li, ‘Clarification technologies for monoclonal antibody manufacturing processes: Current state and future perspectives’, *Biotechnol Bioeng*, vol. 113, no. 4, pp. 698–716, Apr. 2016, doi: 10.1002/bit.25810.

[47] M. E. Warkiani, A. K. P. Tay, G. Guan, and J. Han, ‘Membrane-less microfiltration using inertial microfluidics’, *Sci Rep*, vol. 5, no. 1, pp. 1–10, Jul. 2015, doi: 10.1038/srep11018.

[48] A. J. Chung and S. C. Hur, ‘High-Speed Microfluidic Manipulation of Cells’, in *Micro- and Nanomanipulation Tools*, wiley, 2015, pp. 1–40. doi: 10.1002/9783527690237.ch1.

[49] T. Kwon, R. Yao, J. F. P. Hamel, and J. Han, ‘Continuous removal of small nonviable suspended mammalian cells and debris from bioreactors using inertial microfluidics’, *Lab Chip*, vol. 18, no. 18, pp. 2826–2837, Sep. 2018, doi: 10.1039/c8lc00250a.

[50] T. Kwon *et al.*, ‘Microfluidic Cell Retention Device for Perfusion of Mammalian Suspension Culture’, *Sci Rep*, vol. 7, no. 1, pp. 1–11, Dec. 2017, doi: 10.1038/s41598-017-06949-8.

[51] S. B. Wang, S. Godfrey, F. Radoniqi, H. Lin, and J. Coffman, ‘Larger Pore Size Hollow Fiber Membranes as a Solution to the Product Retention Issue in Filtration-

Based Perfusion Bioreactors', *Biotechnol J*, vol. 14, no. 2, p. 1800137, Feb. 2019, doi: 10.1002/biot.201800137.

[52] D. J. Karst, E. Serra, T. K. Villiger, M. Soos, and M. Morbidelli, 'Characterization and comparison of ATF and TFF in stirred bioreactors for continuous mammalian cell culture processes', *Biochem Eng J*, vol. 110, pp. 17–26, Jun. 2016, doi: 10.1016/j.bej.2016.02.003.

[53] J. M. Bielser, M. Wolf, J. Souquet, H. Broly, and M. Morbidelli, 'Perfusion mammalian cell culture for recombinant protein manufacturing – A critical review', *Biotechnol Adv*, vol. 36, no. 4, pp. 1328–1340, Jul. 2018, doi: 10.1016/j.biotechadv.2018.04.011.

[54] A. J. Brennan, J. Shevitz, and J. D. Macmillan, 'A perfusion system for antibody production by shear-sensitive hybridoma cells in a stirred reactor', *Biotechnology Techniques*, vol. 1, no. 3, pp. 169–174, Sep. 1987, doi: 10.1007/BF00227555.

[55] B. Bosco, C. Paillet, I. Amadeo, L. Mauro, E. Orti, and G. Forno, 'Alternating flow filtration as an alternative to internal spin filter based perfusion process: Impact on productivity and product quality', *Biotechnol Prog*, vol. 33, no. 4, pp. 1010–1014, Jul. 2017, doi: 10.1002/btpr.2487.

[56] W. Kelly, J. Rubin, J. Scully, H. Kamaraju, P. Wnukowski, and R. Bhatia, 'Understanding and modeling retention of mammalian cells in fluidized bed

centrifuges’, *Biotechnol Prog*, vol. 32, no. 6, pp. 1520–1530, 2016, doi: 10.1002/btpr.2365.

[57] M. Iammarino, J. Nti-gyabaah, M. Chandler, D. Roush, and K. Göklen, ‘Impact of Cell Density and Viability on Primary Clarification of Mammalian Cell Broth-An Analysis using Disc-stack Centrifugation and Charged Depth filtration’, *Bioprocess Int*, vol. 38, no. November, pp. 38–50, 2007.

[58] P. Levison, A. Elliott, I.-K. Wang, and M. Collins, ‘Acoustic Wave Separation – A non-filtration approach for continuous clarification of perfusion cell culture prior to capture chromatography’, in *Integrated Continuous Biomanufacturing IV*, Oct. 2019.

[59] D. Burgstaller *et al.*, ‘Continuous cell flocculation for recombinant antibody harvesting’, *Journal of Chemical Technology and Biotechnology*, vol. 93, no. 7, pp. 1881–1890, Jul. 2018, doi: 10.1002/jctb.5500.

[60] A. Davailles, E. Climent, and F. Bourgeois, ‘Fundamental understanding of swirling flow pattern in hydrocyclones’, *Sep Purif Technol*, vol. 92, pp. 152–160, 2012, doi: 10.1016/j.seppur.2011.12.011.

[61] I. W. Bettinardi, A. Castan, R. A. Medronho, and L. R. Castilho, ‘Hydrocyclones as cell retention device for CHO perfusion processes in single-use bioreactors’, *Biotechnol Bioeng*, p. bit.27335, Mar. 2020, doi: 10.1002/bit.27335.

[62] E. A. Elsayed, L. A. G. Ramalho, L. R. Castilho, and R. A. Medronho, ‘Feed Flow Pulsation in the Separation of CHO Cells in Hydrocyclones: Effects of Pressure Drop and Pumphead Type on Separation Efficiency and Cell Viability’, in *Proceedings of the 21st Annual Meeting of the European Society for Animal Cell Technology (ESACT), Dublin, Ireland, June 7-10, 2009*, Springer Netherlands, 2012, pp. 341–344. doi: 10.1007/978-94-007-0884-6_53.

[63] N. Herrmann, P. Neubauer, and M. Birkholz, ‘Spiral microfluidic devices for cell separation and sorting in bioprocesses’, *Biomicrofluidics*, vol. 13, no. 6, p. 061501, Nov. 2019, doi: 10.1063/1.5125264.

[64] T. Klein, N. Heinzel, P. Kroll, M. Brunner, C. Herwig, and L. Neutsch, ‘Quantification of cell lysis during CHO bioprocesses: Impact on cell count, growth kinetics and productivity’, *J Biotechnol*, vol. 207, pp. 67–76, Aug. 2015, doi: 10.1016/j.jbiotec.2015.04.021.

[65] H. Jeon, T. Kwon, J. Yoon, and J. Han, ‘Engineering a deformation-free plastic spiral inertial microfluidic system for CHO cell clarification in biomanufacturing’, *Lab Chip*, vol. 22, no. 2, pp. 272–285, Jan. 2022, doi: 10.1039/D1LC00995H.

[66] H. F. Ko and R. Bhatia, ‘Evaluation of single-use fluidized bed centrifuge system for mammalian cell harvesting’, *Biopharm Int*, vol. 25, no. 11, pp. 34–40, 2012.

[67] J. K. Byoung, N. C. Ho, and J. O. Duk, ‘Application of a cell-once-through perfusion strategy for production of recombinant antibody from rCHO cells in a Centritech

Lab II centrifuge system', *Biotechnol Prog*, vol. 23, no. 5, pp. 1186–1197, Aug. 2007, doi: 10.1021/bp0700861.

[68] J. K. Byoung, J. O. Duk, and N. C. Ho, 'Limited use of Centritech Lab II centrifuge in perfusion culture of rCHO cells for the production of recombinant antibody', *Biotechnol Prog*, vol. 24, no. 1, pp. 166–174, Feb. 2008, doi: 10.1021/bp070235f.

[69] A. Richardson and J. Walker, 'Continuous Solids Discharging centrifugation to Solve Clarifying High-Cell-Density Mammalian Cell Cultures', *BioProcess International*, Apr. 19, 2018. https://bioprocessintl.com/downstream-processing/separation-purification/continuous-solids-discharging-centrifugation-a-solution-to-the-challenges-of-clarifying-high-cell-density-mammalian-cell-cultures/ (accessed Apr. 28, 2020).

[70] F. Trampler, J. M. Piret, T. Keijzer, and A. D. Ambruoso, 'Biosep: Acoustic cell retention system for perfusion cultivation with high cell concentration'. https://www.applikon-biotechnology.com/files/applikon-biosep-high-cell-concentration.pdf (accessed Apr. 21, 2020).

[71] B. Lipkens, E. Miller, B. Ross-Johnsrud, W. Presz, K. C. Chitale, and T. J. Kennedy III, 'Acoustic Perfusion Devices', US 20180298323A1, 2018

[72] M. F. Clincke *et al.*, 'Very high density of Chinese hamster ovary cells in perfusion by alternating tangential flow or tangential flow filtration in WAVE bioreactor™-

part II: Applications for antibody production and cryopreservation', *Biotechnol Prog*, vol. 29, no. 3, pp. 768–777, May 2013, doi: 10.1002/btpr.1703.

[73] V. Warikoo *et al.*, 'Integrated continuous production of recombinant therapeutic proteins', *Biotechnol Bioeng*, vol. 109, no. 12, pp. 3018–3029, 2012, doi: 10.1002/bit.24584.

[74] A. S. Rathore and A. Velayudhan, *Scale-Up and Optimization in Preparative Chromatography Principles and Biopharmaceutical Applications edited by*. Marcel Dekker, 2003.

[75] R. Hernandez, 'To surge or not to surge?', *Genetic Engineering and Biotechnology News*, 2017. https://www.genengnews.com/magazine/300/to-surge-or-not-to-surge/ (accessed Apr. 17, 2020).

[76] S. M. Mercier, B. Diepenbroek, R. H. Wijffels, and M. Streefland, 'Multivariate PAT solutions for biopharmaceutical cultivation: Current progress and limitations', *Trends Biotechnol*, vol. 32, no. 6, pp. 329–336, 2014, doi: 10.1016/j.tibtech.2014.03.008.

[77] J. K. K. Mark, C. S. Y. Lim, F. Nordin, and G. J. Tye, 'Expression of mammalian proteins for diagnostics and therapeutics: a review', *Molecular Biology Reports 2022 49:11*, vol. 49, no. 11, pp. 10593–10608, Jun. 2022, doi: 10.1007/S11033-022-07651-3.

[78] H. Lim *et al.*, ‘Structural biology of the TNFα antagonists used in the treatment of rheumatoid arthritis’, *International Journal of Molecular Sciences*, vol. 19, no. 3. MDPI AG, Mar. 07, 2018. doi: 10.3390/ijms19030768.

[79] M. Hunt, ‘Linear and Nonlinear Free Surface Flows in Electrohydrodynamics’, Doctor of Philosophy, University of London, London, 2013. Accessed: Jan. 29, 2018. [Online]. Available: http://hyperkahler.co.uk/wp-content/uploads/2013/06/PhD_thesis.pdf

[80] R. Jiang, H. Chen, and S. Xu, ‘pH excursions impact CHO cell culture performance and antibody N-linked glycosylation’, *Bioprocess and Biosystems Engineering 2018 41:12*, vol. 41, no. 12, pp. 1731–1741, Aug. 2018, doi: 10.1007/S00449-018-1996-Y.

[81] L. Naumann, P. Schlossbauer, F. Klingler, F. Hesse, K. Otte, and C. Neusüß, ‘High-throughput glycosylation analysis of intact monoclonal antibodies by mass spectrometry coupled with capillary electrophoresis and liquid chromatography’, *J Sep Sci*, vol. 45, no. 12, pp. 2034–2044, Jun. 2022, doi: 10.1002/JSSC.202100865.

[82] X. R. Jiang *et al.*, ‘Advances in the assessment and control of the effector functions of therapeutic antibodies’, *Nature Reviews Drug Discovery 2011 10:2*, vol. 10, no. 2, pp. 101–111, Feb. 2011, doi: 10.1038/nrd3365.

[83] T. Shantha Raju and R. E. Jordan, ‘Galactosylation variations in marketed therapeutic antibodies’, *MAbs*, vol. 4, no. 3, pp. 385–391, May 2012, doi: 10.4161/MABS.19868.

[84] M. Dalziel, M. Crispin, C. N. Scanlan, N. Zitzmann, and R. A. Dwek, ‘Emerging principles for the therapeutic exploitation of glycosylation’, *Science (1979)*, vol. 343, no. 6166, Jan. 2014, doi: 10.1126/SCIENCE.1235681.

[85] H. C. Ebbers, P. J. K. van Meer, E. H. M. Moors, A. K. Mantel-Teeuwisse, H. G. M. Leufkens, and H. Schellekens, ‘Measures of biosimilarity in monoclonal antibodies in oncology: the case of bevacizumab’, *Drug Discov Today*, vol. 18, no. 17–18, pp. 872–879, Sep. 2013, doi: 10.1016/J.DRUDIS.2013.05.004.

[86] R. Abès and J. L. Teillaud, ‘Impact of Glycosylation on Effector Functions of Therapeutic IgG’, *Pharmaceuticals 2010, Vol. 3, Pages 146-157*, vol. 3, no. 1, pp. 146–157, Jan. 2010, doi: 10.3390/PH3010146.

[87] I. J. del Val, C. Kontoravdi, and J. M. Nagy, ‘Towards the implementation of quality by design to the production of therapeutic monoclonal antibodies with desired glycosylation patterns’, *Biotechnol Prog*, vol. 26, no. 6, pp. 1505–1527, Nov. 2010, doi: 10.1002/btpr.470.

[88] F. Higel, A. Seidl, F. Sörgel, and W. Friess, ‘N-glycosylation heterogeneity and the influence on structure, function and pharmacokinetics of monoclonal antibodies and

Fc fusion proteins', *European Journal of Pharmaceutics and Biopharmaceutics*, vol. 100, pp. 94–100, Mar. 2016, doi: 10.1016/j.ejpb.2016.01.005.

[89] S. Schreiber, K. Yamamoto, R. Muniz, and T. Iwura, 'Physicochemical analysis and biological characterization of FKB327 as a biosimilar to adalimumab', *Pharmacol Res Perspect*, vol. 8, no. 3, Jun. 2020, doi: 10.1002/PRP2.604.

[90] R. Jefferis, 'Antibody therapeutics: isotype and glycoform selection', *http://dx.doi.org/10.1517/14712598.7.9.1401*, vol. 7, no. 9, pp. 1401–1413, Sep. 2007, doi: 10.1517/14712598.7.9.1401.

[91] L. W. Chong, M. Saghafi, C. Knappe, S. Steigmiller, C. Matanguihan, and C. T. Goudar, 'Robust on-line sampling and analysis during long-term perfusion cultivation of mammalian cells', *J Biotechnol*, vol. 165, no. 2, pp. 133–137, May 2013, doi: 10.1016/j.jbiotec.2013.03.008.

[92] R. M. Santos, P. Kaiser, J. C. Menezes, and A. Peinado, 'Improving reliability of Raman spectroscopy for mAb production by upstream processes during bioprocess development stages', *Talanta*, vol. 199, pp. 396–406, Jul. 2019, doi: 10.1016/j.talanta.2019.02.088.

[93] R. F. Steinhoff *et al.*, 'Microarray-based MALDI-TOF mass spectrometry enables monitoring of monoclonal antibody production in batch and perfusion cell cultures', *Methods*, vol. 104, pp. 33–40, Jul. 2016, doi: 10.1016/j.ymeth.2015.12.011.

[94] L. Zhao, H. Y. Fu, W. Zhou, and W. S. Hu, ‘Advances in process monitoring tools for cell culture bioprocesses’, *Eng Life Sci*, vol. 15, no. 5, pp. 459–468, Jul. 2015, doi: 10.1002/elsc.201500006.

[95] L. Rolinger, M. Rüdt, and J. Hubbuch, ‘A critical review of recent trends, and a future perspective of optical spectroscopy as PAT in biopharmaceutical downstream processing’, *Analytical and Bioanalytical Chemistry 2020 412:9*, vol. 412, no. 9, pp. 2047–2064, Mar. 2020, doi: 10.1007/S00216-020-02407-Z.

[96] H. Yang, S. Yang, J. Kong, A. Dong, and S. Yu, ‘Obtaining information about protein secondary structures in aqueous solution using Fourier transform IR spectroscopy’, *Nature Protocols 2015 10:3*, vol. 10, no. 3, pp. 382–396, Feb. 2015, doi: 10.1038/nprot.2015.024.

[97] J. C. Wasalathanthri, Dhanuka Pulasthi, Tewari, X. Kang, M. Hincapie, S. L. Barrett, and J. S. Pollock, ‘Multivariate spectral analysis and monitoring for biomanufacturing’, Sep. 05, 2019

[98] B. C. Smith, ‘Fundamentals of Fourier Transform Infrared Spectroscopy’, Mar. 2011, doi: 10.1201/B10777.

[99] L. Rolinger, M. Rüdt, and J. Hubbuch, ‘A critical review of recent trends, and a future perspective of optical spectroscopy as PAT in biopharmaceutical downstream processing’, *Analytical and Bioanalytical Chemistry*, vol. 412, no. 9. Springer, pp. 2047–2064, Apr. 01, 2020. doi: 10.1007/s00216-020-02407-z.

[100] *Handbook of Vibrational Spectroscopy*. Wiley, 2001. doi: 10.1002/0470027320.

[101] Thermo Scientific, 'Extinction Coefficients, A guide to understanding extinction coefficients, with emphasis on spectrophotometric determination of protein concentration. TECH TIP #6', 2013. www.thermoscientific.com/pierce. (accessed Feb. 19, 2023).

[102] 'Instrumentation for Fluorescence Spectroscopy', *Principles of Fluorescence Spectroscopy*, pp. 27–61, 2006, doi: 10.1007/978-0-387-46312-4_2.

[103] G. ElMasry and S. Nakauchi, 'Prediction of meat spectral patterns based on optical properties and concentrations of the major constituents', *Food Sci Nutr*, vol. 4, no. 2, pp. 269–283, Mar. 2016, doi: 10.1002/FSN3.286.

[104] Z. Q. Wen, 'Raman spectroscopy of protein pharmaceuticals', *J Pharm Sci*, vol. 96, no. 11, pp. 2861–2878, Nov. 2007, doi: 10.1002/JPS.20895.

[105] G. Thakur, V. Hebbi, and A. S. Rathore, 'An NIR-based PAT approach for real-time control of loading in Protein A chromatography in continuous manufacturing of monoclonal antibodies', *Biotechnol Bioeng*, vol. 117, no. 3, pp. 673–686, Mar. 2020, doi: 10.1002/bit.27236.

[106] D. A. Zavala-Ortiz *et al.*, 'Interest of locally weighted regression to overcome nonlinear effects during in situ NIR monitoring of CHO cell culture parameters and antibody glycosylation', *Biotechnol Prog*, vol. 36, no. 1, Jan. 2020, doi: 10.1002/btpr.2924.

[107] D. A. Zavala-Ortiz *et al.*, ‘Support Vector and Locally Weighted regressions to monitor monoclonal antibody glycosylation during CHO cell culture processes, an enhanced alternative to Partial Least Squares regression’, *Biochem Eng J*, vol. 154, p. 107457, Feb. 2020, doi: 10.1016/j.bej.2019.107457.

[108] E. W. Ciurczak, B. Igne, J. Workman, and D. A. Burns, *Handbook of Near-Infrared Analysis*, 4th ed. Boca Raton: CRC Press, 2021. doi: https://doi.org/10.1201/b22513.

[109] I. López-Peña, B. S. Leigh, D. E. Schlamadinger, and J. E. Kim, ‘Insights into Protein Structure and Dynamics by Ultraviolet and Visible Resonance Raman Spectroscopy’, *Biochemistry*, vol. 54, no. 31, pp. 4770–4783, Aug. 2015, doi: 10.1021/ACS.BIOCHEM.5B00514.

[110] D. Yilmaz, H. Mehdizadeh, D. Navarro, A. Shehzad, M. O’Connor, and P. McCormick, ‘Application of Raman spectroscopy in monoclonal antibody producing continuous systems for downstream process intensification’, *Biotechnol Prog*, Jan. 2020, doi: 10.1002/btpr.2947.

[111] M. Y. Li, B. Ebel, C. Paris, F. Chauchard, E. Guedon, and A. Marc, ‘Real-time monitoring of antibody glycosylation site occupancy by in situ Raman spectroscopy during bioreactor CHO cell cultures’, *Biotechnol Prog*, vol. 34, no. 2, pp. 486–493, Mar. 2018, doi: 10.1002/btpr.2604.

[112] M. Zschätzsch *et al.*, ‘Monitoring bioactive and total antibody concentrations for continuous process control by surface plasmon resonance spectroscopy’, *Eng Life Sci*, vol. 19, no. 10, pp. 681–690, Oct. 2019, doi: 10.1002/elsc.201900014.

[113] T. Tran *et al.*, ‘Real-time nanoplasmonic sensor for IGG monitoring in bioproduction’, *Processes*, vol. 8, no. 10, pp. 1–12, Oct. 2020, doi: 10.3390/pr8101302.

[114] J. E. Noble and M. J. A. Bailey, ‘Chapter 8 Quantitation of Protein’, *Methods Enzymol*, vol. 463, no. C, pp. 73–95, Jan. 2009, doi: 10.1016/S0076-6879(09)63008-1.

[115] D. A. Skoog, D. M. West, F. J. Holler, and S. R. Crouch, *Fundamentals of analytical chemistry*, Tenth edition. Boston, MA: Cengage, 2022.

[116] D. J. A. C. Wim Jiskoot, Ed., *Methods for Structural Analysis of Protein Pharmaceuticals*. Arlington, VA: AAPS PRESS, 2005.

[117] U. Patil, M. Crum, B. Vu, K. Wasden, K. Kourentzi, and R. C. Willson, ‘Continuous Fc detection for protein a capture process control’, *Biosens Bioelectron*, p. 112327, May 2020, doi: 10.1016/j.bios.2020.112327.

[118] M. Swartz, ‘HPLC detectors: a brief review’, *J Liq Chromatogr Relat Technol*, vol. 33, no. 9–12, pp. 1130–1150, 2010, doi: 10.1080/10826076.2010.484356.

[119] Scott Huffman, Keyur Soni, and Joe Ferraiolo, ‘UV-Vis Based Determination of Protein Concentration: Validating and Implementing Slope Measurements Using Variable Pathlength Technology’, *BioProcess International*, Sep. 11, 2014. https://bioprocessintl.com/manufacturing/monoclonal-antibodies/uv-vis-based-determination-protein-concentration-validating-implementing-slope-measurements-using-variable-pathlength-technology/ (accessed Feb. 19, 2023).

[120] Jeffrey D. Goby, Joelle N. Khouri, Anoushka Durve, Eike Zimmermann, and Kenji Furuya, ‘Control of Protein A Column Loading During Continuous Antibody Production: A Technology Overview of Real-Time Titer Measurement Methods’, *Bioprocess International*, Sep. 21, 2019. https://bioprocessintl.com/analytical/pat/control-of-protein-a-column-loading-during-continuous-antibody-production-real-time-titer-measurement-methods/ (accessed Feb. 20, 2023).

[121] M. Rüdt, N. Brestrich, L. Rolinger, and J. Hubbuch, ‘Real-time monitoring and control of the load phase of a protein A capture step’, *Biotechnol Bioeng*, vol. 114, no. 2, pp. 368–373, Feb. 2017, doi: 10.1002/bit.26078.

[122] S. H. Ko, D. Chandra, W. Ouyang, T. Kwon, P. Karande, and J. Han, ‘Nanofluidic device for continuous multiparameter quality assurance of biologics’, *Nat Nanotechnol*, vol. 12, no. 8, pp. 804–812, Aug. 2017, doi: 10.1038/NNANO.2017.74.

[123] T. Kwon, S. H. Ko, J.-F. P. Hamel, and J. Han, ‘Continuous Online Protein Quality Monitoring during Perfusion Culture Production Using an Integrated Micro/Nanofluidic System’, *Anal Chem*, vol. 92, no. 7, pp. 5267–5275, 2020, doi: 10.1021/acs.analchem.9b05835.

[124] P. Mao and J. Han, ‘Fabrication and characterization of 20 nm planar nanofluidic channels by glass-glass and glass-silicon bonding’, *Lab Chip*, vol. 5, no. 8, pp. 837–844, Jul. 2005, doi: 10.1039/b502809d.

[125] M. E. Pedersen, J. Østergaard, and H. Jensen, ‘In-Solution IgG Titer Determination in Fermentation Broth Using Affibodies and Flow-Induced Dispersion Analysis’, *ACS Omega*, vol. 5, no. 18, pp. 10519–10524, May 2020, doi: 10.1021/ACSOMEGA.0C00791.

[126] S. C. de Graaf, M. Hoek, S. Tamara, and A. J. R. Heck, ‘A perspective toward mass spectrometry-based de novo sequencing of endogenous antibodies’, *MAbs*, vol. 14, no. 1, 2022, doi: 10.1080/19420862.2022.2079449.

[127] T. K. Toby, L. Fornelli, and N. L. Kelleher, ‘Progress in Top-Down Proteomics and the Analysis of Proteoforms’, *Annual Review of Analytical Chemistry*, vol. 9, pp. 499–519, Jun. 2016, doi: 10.1146/ANNUREV-ANCHEM-071015-041550.

[128] B. P. Johansson, O. Shannon, and L. Björck, ‘IdeS: A Bacterial Proteolytic Enzyme with Therapeutic Potential’, *PLoS One*, vol. 3, no. 2, p. e1692, Feb. 2008, doi: 10.1371/JOURNAL.PONE.0001692.

[129] E. A. Redman, N. G. Batz, J. S. Mellors, and J. M. Ramsey, ‘Integrated microfluidic capillary electrophoresis-electrospray ionization devices with online ms detection for the separation and characterization of intact monoclonal antibody variants’, *Anal Chem*, vol. 87, no. 4, pp. 2264–2272, Feb. 2015, doi: 10.1021/AC503964J.

[130] J. Hajduk *et al.*, ‘Monitoring of antibody glycosylation pattern based on microarray MALDI-TOF mass spectrometry’, *J Biotechnol*, vol. 302, pp. 77–84, Aug. 2019, doi: 10.1016/j.jbiotec.2019.06.306.

[131] K. Böttinger, W. Esser-Skala, M. Segl, C. Herwig, and C. G. Huber, ‘At-line quantitative profiling of monoclonal antibody products during bioprocessing using HPLC-MS’, *Anal Chim Acta*, vol. 1207, p. 339813, May 2022, doi: 10.1016/J.ACA.2022.339813.

[132] I. Snapkov, M. Chernigovskaya, P. Sinitcyn, K. Lê Quý, T. A. Nyman, and V. Greiff, ‘Progress and challenges in mass spectrometry-based analysis of antibody repertoires’, *Trends Biotechnol*, vol. 40, no. 4, pp. 463–481, Apr. 2022, doi: 10.1016/J.TIBTECH.2021.08.006.

[133] M. B. Taraban, K. T. Briggs, P. Merkel, and Y. Bruce Yu, ‘Flow Water Proton NMR: In-Line Process Analytical Technology for Continuous Biomanufacturing’, *Anal Chem*, vol. 91, no. 21, pp. 13538–13546, Nov. 2019, doi: 10.1021/acs.analchem.9b02622.

[134] M. Bakhshpour *et al.*, ‘Sensitive and real-time detection of IgG using interferometric reflecting imaging sensor system’, *Biosens Bioelectron*, vol. 201, p. 113961, Apr. 2022, doi: 10.1016/J.BIOS.2021.113961.

[135] B. Moore, R. Sanford, and A. Zhang, ‘Case study: The characterization and implementation of dielectric spectroscopy (biocapacitance) for process control in a commercial GMP CHO manufacturing process’, *Biotechnol Prog*, vol. 35, no. 3, p. e2782, May 2019, doi: 10.1002/btpr.2782.

[136] S. Metze *et al.*, ‘Multivariate data analysis of capacitance frequency scanning for online monitoring of viable cell concentrations in small-scale bioreactors’, *Anal Bioanal Chem*, vol. 412, no. 9, pp. 2089–2102, Apr. 2020, doi: 10.1007/s00216-019-02096-3.

[137] T. Drieschner, E. Ostertag, B. Boldrini, A. Lorenz, M. Brecht, and K. Rebner, ‘Direct optical detection of cell density and viability of mammalian cells by means of UV/VIS spectroscopy’, *Anal Bioanal Chem*, vol. 412, no. 14, pp. 3359–3371, May 2020, doi: 10.1007/s00216-019-02322-y.

[138] J. Claßen, A. Graf, F. Aupert, D. Solle, M. Höhse, and T. Scheper, ‘A novel LED-based 2D-fluorescence spectroscopy system for in-line bioprocess monitoring of Chinese hamster ovary cell cultivations—Part II’, *Eng Life Sci*, vol. 19, no. 5, pp. 341–351, May 2019, doi: 10.1002/elsc.201800146.

[139] A. Tulsyan, T. Wang, G. Schorner, H. Khodabandehlou, M. Coufal, and C. Undey, ‘Automatic real-time calibration, assessment, and maintenance of generic Raman models for online monitoring of cell culture processes’, *Biotechnol Bioeng*, vol. 117, no. 2, pp. 406–416, Feb. 2020, doi: 10.1002/bit.27205.

[140] R. M. Santos, J. M. Kessler, P. Salou, J. C. Menezes, and A. Peinado, ‘Monitoring mAb cultivations with in-situ raman spectroscopy: The influence of spectral selectivity on calibration models and industrial use as reliable PAT tool’, *Biotechnol Prog*, vol. 34, no. 3, pp. 659–670, May 2018, doi: 10.1002/btpr.2635.

[141] K. Schwab and F. Hesse, ‘Estimating extrinsic dyes for fluorometric online monitoring of antibody aggregation in CHO fed-batch cultivations’, *Bioengineering*, vol. 4, no. 3, Sep. 2017, doi: 10.3390/bioengineering4030065.

[142] C. Cannizzaro, R. Gügerli, I. Marison, and U. Von Stockar, ‘On-Line Biomass Monitoring of CHO Perfusion Culture With Scanning Dielectric Spectroscopy’, *Biotechnol Bioeng*, vol. 84, no. 5, pp. 597–610, Dec. 2003, doi: 10.1002/bit.10809.

[143] A. Tulsyan, G. Schorner, H. Khodabandehlou, T. Wang, M. Coufal, and C. Undey, ‘A machine-learning approach to calibrate generic Raman models for real-time monitoring of cell culture processes’, *Biotechnol Bioeng*, vol. 116, no. 10, pp. 2575–2586, Oct. 2019, doi: 10.1002/bit.27100.

[144] L. D. Menard and J. M. Ramsey, ‘Fabrication of sub-5 nm nanochannels in insulating substrates using focused ion beam milling’, *Nano Lett*, vol. 11, no. 2, pp. 512–517, Feb. 2011, doi: 10.1021/NL103369G/.

[145] ‘Technical datasheet APPLICATIONS SPIN CURVES (200MM SILICON) AZ ® 10XT Series Thick Positive Tone Photoresists’.

[146] K. S. Chen, A. A. Ayón, X. Zhang, and S. M. Spearing, ‘Effect of process parameters on the surface morphology and mechanical performance of silicon structures after deep reactive ion etching (DRIE)’, *Journal of Microelectromechanical Systems*, vol. 11, no. 3, pp. 264–275, Jun. 2002, doi: 10.1109/JMEMS.2002.1007405.

[147] W. T. Pike, W. J. Karl, S. Kumar, S. Vijendran, and T. Semple, ‘Analysis of sidewall quality in through-wafer deep reactive-ion etching’, *Microelectron Eng*, vol. 73–74, pp. 340–345, Jun. 2004, doi: 10.1016/j.mee.2004.02.064.

[148] T. M. H. Lee, I. M. Hsing, and C. Y. N. Liaw, ‘An improved anodic bonding process using pulsed voltage technique’, *Journal of Microelectromechanical Systems*, vol. 9, no. 4, pp. 469–473, 2000, doi: 10.1109/84.896767.

[149] U. Gösele and Q. Y. Tong, ‘Semiconductor wafer bonding’, *Annual Review of Materials Science*, vol. 28, no. 1, pp. 215–241, Nov. 2003, doi: 10.1146/ANNUREV.MATSCI.28.1.215.

[150] S. Bao *et al.*, ‘A review of silicon-based wafer bonding processes, an approach to realize the monolithic integration of Si-CMOS and III–V-on-Si wafers’, *Journal of*

Semiconductors, vol. 42, no. 2, p. 023106, Feb. 2021, doi: 10.1088/1674-4926/42/2/023106.

[151] K. T. Turner and S. M. Spearing, ‘Modeling of direct wafer bonding: Effect of wafer bow and etch patterns’, *J Appl Phys*, vol. 92, no. 12, p. 7658, Nov. 2002, doi: 10.1063/1.1521792.

[152] Q. Y. Tong and U. Gösele, ‘Semiconductor wafer bonding: recent developments’, *Mater Chem Phys*, vol. 37, no. 2, pp. 101–127, Mar. 1994, doi: 10.1016/0254-0584(94)90080-9.

[153] C. Mai, M. Li, and S. Yang, ‘Low temperature direct bonding of silica glass via wet chemical surface activation’, *RSC Adv*, vol. 5, no. 53, pp. 42721–42727, May 2015, doi: 10.1039/C5RA06705G.

[154] R. W. Bower, M. S. Ismail, and B. E. Roberds, ‘Low temperature Si3N4 direct bonding’, *Appl Phys Lett*, vol. 62, no. 26, p. 3485, Jun. 1998, doi: 10.1063/1.109002.

[155] Q. Y. Tong, G. Fountain, and P. Enquist, ‘Room temperature SiO2/SiO2 covalent bonding’, *Appl Phys Lett*, vol. 89, no. 4, p. 042110, Jul. 2006, doi: 10.1063/1.2240232.

[156] J. Langan, J. A. Shorter, X. Xin, and J. I. Steinfeld, ‘Reactions of Photogenerated CF 2 and CF 3 on Silicon and Silicon Oxide Surfaces’, *MRS Proceedings*, vol. 129, no. 1, pp. 311–314, Feb. 1988, doi: 10.1557/PROC-129-311.

[157] V. Masteika, J. Kowal, N. St. J. Braithwaite, and T. Rogers, ‘A Review of Hydrophilic Silicon Wafer Bonding’, *ECS Journal of Solid State Science and Technology*, vol. 3, no. 4, pp. Q42–Q54, Feb. 2014, doi: 10.1149/2.007403jss.

[158] A. Sanz-Velasco, P. Amirfeiz, S. Bengtsson, and C. Colinge, ‘Room Temperature Wafer Bonding Using Oxygen Plasma Treatment in Reactive Ion Etchers With and Without Inductively Coupled Plasma’, *J Electrochem Soc*, vol. 150, no. 2, p. G155, Jan. 2003, doi: 10.1149/1.1536182.

[159] A. Weinert, P. Amirfeiz, and S. Bengtsson, ‘Plasma assisted room temperature bonding for MST’, *Sens Actuators A Phys*, vol. 92, no. 1–3, pp. 214–222, Aug. 2001, doi: 10.1016/S0924-4247(01)00579-9.

[160] S. N. Farrens, J. R. Dekker, J. K. Smith, and B. E. Roberds, ‘Chemical Free Room Temperature Wafer To Wafer Direct Bonding’, *J Electrochem Soc*, vol. 142, no. 11, pp. 3949–3955, Nov. 1995, doi: 10.1149/1.2048440.

[161] A. G. Milekhin *et al.*, ‘Infrared spectroscopy of bonded silicon wafers’, *Semiconductors*, vol. 40, no. 11, pp. 1304–1313, Nov. 2006, doi: 10.1134/S1063782606110108.

[162] C. Wang, J. Xu, X. Zeng, Y. Tian, C. Wang, and T. Suga, ‘Low-temperature wafer direct bonding of silicon and quartz glass by a two-step wet chemical surface cleaning’, *Jpn J Appl Phys*, vol. 57, no. 2, p. 02BD02, Feb. 2018, doi: 10.7567/JJAP.57.02BD02.

[163] C. Wang and T. Suga, ‘Investigation of fluorine containing plasma activation for room-temperature bonding of Si-based materials’, *Microelectronics Reliability*, vol. 52, no. 2, pp. 347–351, Feb. 2012, doi: 10.1016/j.microrel.2011.09.005.

[164] K. Ljungberg, A. Söderbärg, and U. Jansson, ‘Improved direct bonding of Si and SiO2 surfaces by cleaning in H2SO4:H2O2:HF’, *Appl Phys Lett*, vol. 67, no. 5, p. 650, Aug. 1998, doi: 10.1063/1.115191.

[165] C. Wang and T. Suga, ‘Room-Temperature Direct Bonding Using Fluorine Containing Plasma Activation’, *J Electrochem Soc*, vol. 158, no. 5, p. H525, Mar. 2011, doi: 10.1149/1.3560510.

[166] I. Zgura *et al.*, ‘Nanostructured SiOx layers as substrates for liquid crystal local ordering. I. Functionalization to bind Bovine Serum Albumin’, *Optoelectronics and Advanced Materials - Rapid Communications*, vol. 5, no. March 2011, pp. 318–323, Mar. 2011.

[167] C. Mathieu *et al.*, ‘Molecular Staples on Si(001)-2 × 1: Dual-Head Primary Amines’, *Journal of Physical Chemistry C*, vol. 113, no. 26, pp. 11336–11345, Jul. 2009, doi: 10.1021/JP902918J.

[168] T. Böcking, M. James, H. G. L. Coster, T. C. Chilcott, and K. D. Barrow, ‘Structural characterization of organic multilayers on silicon (111) formed by immobilization of molecular films on functionalized Si-C linked monolayers’, *Langmuir*, vol. 20, no. 21, pp. 9227–9235, Oct. 2004, doi: 10.1021/LA048474P.

[169] P. Abgrall and N. T. Nguyen, ‘Nanofluidic devices and their applications’, *Anal Chem*, vol. 80, no. 7, pp. 2326–2341, Apr. 2008, doi: 10.1021/AC702296U.

[170] C. Duan, R. Karnik, M. C. Lu, and A. Majumdar, ‘Evaporation-induced cavitation in nanofluidic channels’, *Proc Natl Acad Sci U S A*, vol. 109, no. 10, pp. 3688–3693, Mar. 2012, doi: https://doi.org/10.1073/pnas.1014075109.

[171] R. Karnik, K. Castelino, C. Duan, and A. Majumdar, ‘Diffusion-limited patterning of molecules in nanofluidic channels’, *Nano Lett*, vol. 6, no. 8, pp. 1735–1740, Aug. 2006, doi: 10.1021/NL061159Y/.

[172] K. Morikawa and T. Tsukahara, ‘Investigation of Unique Protonic and Hydrodynamic Behavior of Aqueous Solutions Confined in Extended Nanospaces’, *Isr J Chem*, vol. 54, no. 11–12, pp. 1564–1572, Nov. 2014, doi: 10.1002/IJCH.201400095.

[173] R. B. Schoch, J. Han, and P. Renaud, ‘Transport phenomena in nanofluidics’, *Rev Mod Phys*, vol. 80, no. 3, pp. 839–883, Jul. 2008, doi: 10.1103/REVMODPHYS.80.839.

[174] A. Alizadeh, W. L. Hsu, M. Wang, and H. Daiguji, ‘Electroosmotic flow: From microfluidics to nanofluidics’, *Electrophoresis*, vol. 42, no. 7–8, pp. 834–868, Apr. 2021, doi: 10.1002/ELPS.202000313.

[175] W. Reisner *et al.*, ‘Statics and dynamics of single DNA molecules confined in nanochannels’, *Phys Rev Lett*, vol. 94, no. 19, p. 196101, May 2005, doi: 10.1103/PHYSREVLETT.94.196101.

[176] E. T. Lam *et al.*, ‘Genome mapping on nanochannel arrays for structural variation analysis and sequence assembly’, *Nature Biotechnology 2012 30:8*, vol. 30, no. 8, pp. 771–776, Jul. 2012, doi: 10.1038/nbt.2303.

[177] J. Fu, R. B. Schoch, A. L. Stevens, S. R. Tannenbaum, and J. Han, ‘A patterned anisotropic nanofluidic sieving structure for continuous-flow separation of DNA and proteins’, *Nat Nanotechnol*, vol. 2, pp. 121–128, 2007, doi: 10.1038/nnano.2006.206.

[178] J. Han and H. G. Craighead, ‘Separation of long DNA molecules in a microfabricated entropic trap array’, *Science (1979)*, vol. 288, no. 5468, pp. 1026–1029, May 2000, doi: 10.1126/SCIENCE.288.5468.1026.

[179] N. Kaji *et al.*, ‘Separation of Long DNA Molecules by Quartz Nanopillar Chips under a Direct Current Electric Field’, *Anal Chem*, vol. 76, no. 1, pp. 15–22, Jan. 2004, doi: 10.1021/AC030303M.

[180] L. I. Segerink and J. C. T. Eijkel, ‘Nanofluidics in point of care applications’, *Lab Chip*, vol. 14, no. 17, pp. 3201–3205, Jul. 2014, doi: 10.1039/C4LC00298A.

[181] Y. C. Wang, A. L. Stevens, and J. Han, ‘Million-fold preconcentration of proteins and peptides by nanofluidic filter’, *Anal Chem*, vol. 77, no. 14, pp. 4293–4299, Jul. 2005, doi: 10.1021/AC050321Z.

[182] T. Kwon, S. H. Ko, J.-F. P. Hamel, and J. Han, ‘Continuous Online Protein Quality Monitoring during Perfusion Culture Production Using an Integrated Micro/Nanofluidic System’, *Anal Chem*, vol. 92, no. 7, pp. 5267–5275, 2020, doi: 10.1021/acs.analchem.9b05835.

[183] J. A. J. Lee, J. Yang, C. Lee, Y. Moon, S. Ahn, and J. Yang, ‘Demonstration of functional similarity of a biosimilar adalimumab SB5 to Humira ®’, *Biologicals*, vol. 58, pp. 7–15, Mar. 2019, doi: 10.1016/j.biologicals.2018.12.002.

[184] C. P. Papaneophytou, A. I. Grigoroudis, C. McInnes, and G. Kontopidis, ‘Quantification of the effects of ionic strength, viscosity, and hydrophobicity on protein-ligand binding affinity’, *ACS Med Chem Lett*, vol. 5, no. 8, pp. 931–936, Aug. 2014, doi: 10.1021/ML500204E.

[185] K. Lis, O. Kuzawińska, and E. Bałkowiec-Iskra, ‘Tumor necrosis factor inhibitors – state of knowledge’, *Arch Med Sci*, vol. 10, no. 6, p. 1175, Dec. 2014, doi: 10.5114/AOMS.2014.47827.

[186] J. Fu, P. Mao, and J. Han, ‘Nanofilter array chip for fast gel-free biomolecule separation’, *Appl Phys Lett*, vol. 87, no. 26, pp. 1–3, 2005, doi: 10.1063/1.2149979.

[187] L. Feng Cheow, H. Bow, and J. Han, ‘Continuous-flow biomolecule concentration and detection in a slanted nanofilter array’, *Lab Chip*, vol. 12, no. 21, pp. 4441–4448, Oct. 2012, doi: 10.1039/C2LC40195A.

[188] ‘Micromixer Chip’. https://www.dolomite-microfluidics.com/product/micromixer-chip/ (accessed Jan. 05, 2023).

[189] D. Bozinovski *et al.*, ‘(293c) Biomanufacturing and Testbed Development for the Continuous Production of Monoclonal Antibodies | AIChE Academy’, in *AIChE Annual Meeting*, Nov. 2021.

[190] J. Marušič, Č. Podlipnik, S. Jevševar, D. Kuzman, G. Vesnaver, and J. Lah, ‘Recognition of human tumor necrosis factor α (TNF-α) by therapeutic antibody fragment: Energetics and structural features’, *Journal of Biological Chemistry*, vol. 287, no. 11, pp. 8613–8620, Mar. 2012, doi: 10.1074/JBC.M111.318451.

[191] ‘Bioinformatics Software for Life Science | DNASTAR | Lasergene’. https://www.dnastar.com/ (accessed Jan. 31, 2023).

[192] ‘Prot pi | Protein Tool’. https://www.protpi.ch/Calculator/ProteinTool#Results (accessed Jan. 31, 2023).

[193] ‘Recombinant human TNF alpha protein (Active) (ab155699) | Abcam’. https://www.abcam.com/recombinant-human-tnf-alpha-protein-active-ab155699.html (accessed Jan. 02, 2023).

[194] S. Bandyopadhyay *et al.*, ‘Physicochemical and functional characterization of a biosimilar adalimumab ZRC-3197’, *Biosimilars*, vol. 5, p. 1, Dec. 2014, doi: 10.2147/bs.s75573.

[195] ‘Expasy - Compute pI/Mw tool’. https://web.expasy.org/compute_pi/ (accessed Jan. 31, 2023).

[196] ‘pKa vs pKa0’. http://www.reachdevices.com/Protein/pKa_explanation.html (accessed Feb. 21, 2023).

[197] ‘Tris(hydroxymethyl)aminomethane’. http://www.cogershop.com/tris-hydroxymethyl-aminomethane-9706443.htm (accessed Feb. 21, 2023).

[198] ‘Boric Acid | H3BO3 - PubChem’. https://pubchem.ncbi.nlm.nih.gov/compound/Boric-acid (accessed Feb. 21, 2023).

[199] J. Han, J. Fu, and R. B. Schoch, ‘Molecular Sieving Using Nanofilters: Past, Present and Future’, *Lab Chip*, vol. 8, no. 1, p. 23, 2008, doi: 10.1039//B714128A.

[200] D. G. Drescher, M. J. Drescher, and N. A. Ramakrishnan, ‘Surface Plasmon Resonance (SPR) Analysis of Binding Interactions of Proteins in Inner-Ear Sensory Epithelia’, *Methods Mol Biol*, vol. 493, p. 323, 2009, doi: 10.1007/978-1-59745-523-7_20.

[201] K. E. van Holde, ‘A hypothesis concerning diffusion-limited protein–ligand interactions’, *Biophys Chem*, vol. 101–102, pp. 249–254, Dec. 2002, doi: 10.1016/S0301-4622(02)00176-X.

[202] H.-X. Zhou, ‘Disparate Ionic-Strength Dependencies of On and Off Rates in Protein-Protein Association’, *Biopolymers*, vol. 59, pp. 427–433, 2001, doi: 10.1002/1097-0282.

[203] P. L. Kastritis and A. M. J. J. Bonvin, ‘On the binding affinity of macromolecular interactions: daring to ask why proteins interact’, *J R Soc Interface*, vol. 10, no. 79, Feb. 2013, doi: 10.1098/RSIF.2012.0835.

[204] ‘HiTrap MabSelect SuRe | Cytiva’. https://www.cytivalifesciences.com/en/us/shop/chromatography/prepacked-columns/affinity-antibody/hitrap-mabselect-sure-p-05659#related-documents (accessed Dec. 19, 2022).

[205] V. Kamat and A. Rafique, ‘Designing binding kinetic assay on the bio-layer interferometry (BLI) biosensor to characterize antibody-antigen interactions’, *Anal Biochem*, vol. 536, pp. 16–31, Nov. 2017, doi: 10.1016/J.AB.2017.08.002.

[206] S. Hu *et al.*, ‘Comparison of the Inhibition Mechanisms of Adalimumab and Infliximab in Treating Tumor Necrosis Factor α-Associated Diseases from a Molecular View’, *Journal of Biological Chemistry*, vol. 288, pp. 27059–27067, 2013, doi: 10.1074/jbc.M113.491530.

[207] K. A. van Schie, P. Ooijevaar-De Heer, L. Dijk, S. Kruithof, G. Wolbink, and T. Rispens, ‘Therapeutic TNF Inhibitors can Differentially Stabilize Trimeric TNF by Inhibiting Monomer Exchange’, *Scientific Reports 2016 6:1*, vol. 6, no. 1, pp. 1–10, Sep. 2016, doi: 10.1038/srep32747.

[208] S. Schreiber, K. Yamamoto, R. Muniz, and T. Iwura, ‘Physicochemical analysis and biological characterization of FKB327 as a biosimilar to adalimumab’, *Pharmacol Res Perspect*, vol. 8, no. 3, Jun. 2020, doi: 10.1002/PRP2.604.

[209] C. Schröter *et al.*, ‘A generic approach to engineer antibody pH-switches using combinatorial histidine scanning libraries and yeast display’, *MAbs*, vol. 7, no. 1, p. 138, Jan. 2015, doi: 10.4161/19420862.2014.985993.

[210] H. Daub, L. Traxler, F. Ismajli, B. Groitl, A. Itzen, and U. Rant, ‘The trimer to monomer transition of Tumor Necrosis Factor-Alpha is a dynamic process that is significantly altered by therapeutic antibodies’, *Scientific Reports 2020 10:1*, vol. 10, no. 1, pp. 1–10, Jun. 2020, doi: 10.1038/s41598-020-66123-5.

[211] R. A. Latour, ‘Fundamental Principles of the Thermodynamics and Kinetics of Protein Adsorption to Material Surfaces Graphical Abstract HHS Public Access’, *Colloids Surf B Biointerfaces*, p. 110992, 2020, doi: 10.1016/j.colsurfb.2020.110992.

[212] C. A. Haynes and W. Norde, ‘Globular proteins at solid/liquid interfaces’, *Colloids Surf B Biointerfaces*, vol. 2, no. 6, pp. 517–566, Jul. 1994, doi: 10.1016/0927-7765(94)80066-9.

[213] T. J. Su, J. R. Lu, R. K. Thomas, Z. F. Cui, and J. Penfold, ‘The Adsorption of Lysozyme at the Silica–Water Interface: A Neutron Reflection Study’, *J Colloid Interface Sci*, vol. 203, no. 2, pp. 419–429, Jul. 1998, doi: 10.1006/JCIS.1998.5545.

[214] D. P. J. Barz, M. J. Vogel, and P. H. Steen, ‘Determination of the zeta potential of porous substrates by droplet deflection. I. The influence of ionic strength and pH value of an aqueous electrolyte in contact with a borosilicate surface’, *Langmuir*, vol. 25, no. 3, pp. 1842–1850, Feb. 2009, doi: 10.1021/LA802949Z/ASSET/IMAGES/LARGE/LA-2008-02949Z_0002.JPEG.

[215] J. Mathes and W. Friess, ‘Influence of pH and ionic strength on IgG adsorption to vials’, *European Journal of Pharmaceutics and Biopharmaceutics*, vol. 78, no. 2, pp. 239–247, Jun. 2011, doi: 10.1016/J.EJPB.2011.03.009.

[216] Nicoya Lifesciences, ‘Reducing Non-Specific Binding in Surface Plasmon Resonance Experiments’, pp. 1–9, 2016, Accessed: Sep. 24, 2020. [Online]. Available: www.nicoyalife.com

[217] H. Zhao, P. H. Brown, and P. Schuck, ‘On the distribution of protein refractive index increments’, *Biophys J*, vol. 100, no. 9, pp. 2309–2317, May 2011, doi: 10.1016/j.bpj.2011.03.004.

[218] T. Kohno, L. T. T. Tam, S. R. Stevens, and J. S. Louie, ‘Binding Characteristics of Tumor Necrosis Factor Receptor-Fc Fusion Proteins vs Anti-Tumor Necrosis Factor mAbs’, *Journal of Investigative Dermatology Symposium Proceedings*, vol. 12, no. 1, pp. 5–8, May 2007, doi: 10.1038/SJ.JIDSYMP.5650034.

[219] A. Hawe, W. L. Hulse, W. Jiskoot, and R. T. Forbes, ‘Taylor Dispersion Analysis Compared to Dynamic Light Scattering for the Size Analysis of Therapeutic Peptides and Proteins and Their Aggregates’, *Pharm Res*, vol. 28, no. 9, p. 2302, Sep. 2011, doi: 10.1007/S11095-011-0460-3.

[220] O. Bermudez and D. Forciniti, ‘Aggregation and denaturation of antibodies: a capillary electrophoresis, dynamic light scattering, and aqueous two-phase partitioning study’, *Journal of Chromatography B*, vol. 807, no. 1, pp. 17–24, Jul. 2004, doi: 10.1016/J.JCHROMB.2004.01.029.

[221] M. E. Pedersen, R. M. S. Haegebaert, J. Østergaard, and H. Jensen, ‘Size-based characterization of adalimumab and TNF-α interactions using flow induced dispersion analysis: assessment of avidity-stabilized multiple bound species’, *Sci Rep*, vol. 11, no. 1, p. 4754, Dec. 2021, doi: 10.1038/s41598-021-84113-z.

[222] D. I. Jang *et al.*, ‘The Role of Tumor Necrosis Factor Alpha (TNF-α) in Autoimmune Disease and Current TNF-α Inhibitors in Therapeutics’, *Int J Mol Sci*, vol. 22, no. 5, pp. 1–16, Mar. 2021, doi: 10.3390/IJMS22052719.

[223] Z. Zhou, B. Yin, and J. Michel, ‘On-chip light sources for silicon photonics’, *Light: Science & Applications 2015 4:11*, vol. 4, no. 11, pp. e358–e358, Nov. 2015, doi: 10.1038/lsa.2015.131.